

AN INCLUSIVE SEARCH FOR BEYOND THE  
STANDARD MODEL LONG-LIVED DECAYS  
WITH THE CMS DETECTOR AT THE LARGE  
HADRON COLLIDER IN  $\sqrt{s} = 13$  TeV DATA

JOSHUA ROBERT HARDENBROOK

A DISSERTATION  
PRESENTED TO THE FACULTY  
OF PRINCETON UNIVERSITY  
IN CANDIDACY FOR THE DEGREE  
OF DOCTOR OF PHILOSOPHY

RECOMMENDED FOR ACCEPTANCE  
BY THE DEPARTMENT OF  
PHYSICS  
ADVISER: CHRISTOPHER G. TULLY

© Copyright by Joshua Robert Hardenbrook, 2017.

All rights reserved.

## Abstract

A search for long-lived particles decaying to jets is presented, performed on the data collected by CMS at a center-of-mass energy  $\sqrt{s} = 13$  TeV in 2015. The data set corresponds to an integrated luminosity of  $2.7 \text{ fb}^{-1}$ . The analysis exploits a set of trigger algorithms and a customized displaced-jet tagger. The number of tagged displaced-jets is used to characterize a potential signal. The pair production of long-lived particles decaying to two jets or to a b jet and a lepton is excluded for masses lighter than 450–1000 GeV, for lifetimes between 1 mm to 1 m.

## Acknowledgements

This is where I acknowledge peeeeeepople

This is the dedication all about how my thesis got turned right upside down

# Contents

Abstract . . . . .	iii
Acknowledgements . . . . .	iv
<b>1 Introduction</b>	<b>1</b>
<b>2 Theory</b>	<b>2</b>
2.1 On Standard Model of Particle Physics . . . . .	2
2.1.1 Getting to Quantum Field Theory . . . . .	3
2.1.2 Symmetries . . . . .	8
2.1.3 Sectors of the Standard Model Lagrangian . . . . .	15
2.1.4 Electroweak Symmetry Breaking (EWSB) . . . . .	17
2.1.5 Divergences in the Standard Model . . . . .	18
2.1.6 Fundamental Fields and Free Parameters of the Standard Model	20
2.1.7 Re-deriving Maxwell's Laws . . . . .	20
2.2 Beyond the Standard Model . . . . .	21
2.2.1 Problems with the Standard Model . . . . .	21
2.2.2 Supersymmetry . . . . .	21
2.2.3 Electroweak Symmetry Breaking in Supersymmetric Theories	21
2.3 Origins of Long-lived Signatures . . . . .	21
2.3.1 Standard Model Particles with Long Lifetimes . . . . .	21
2.3.2 Split-Susy and Naturalness at the LHC . . . . .	23

<b>3 Collider Physics and Phenomenology</b>	<b>25</b>
3.1 Introduction . . . . .	25
3.1.1 From Matrix Elements to Cross Sections . . . . .	26
3.1.2 Kinematics and Conventions . . . . .	30
3.2 Cross-sections . . . . .	32
3.3 Luminosity . . . . .	32
3.4 Parton Model of Hadron Collisions . . . . .	33
3.5 The Narrow Width Approximation . . . . .	35
3.6 Event Simulation . . . . .	35
3.6.1 Hard Process Modeling . . . . .	35
3.6.2 Parton Showering . . . . .	35
3.6.3 Hadronization . . . . .	35
<b>4 Experimental Apparatus</b>	<b>36</b>
4.1 CERN Laboratories . . . . .	36
4.1.1 Funding Model . . . . .	36
4.1.2 Organizational Structure . . . . .	38
4.2 The Large Hadron Collider . . . . .	38
4.3 Other LHC Related Experiments . . . . .	40
4.4 Compact Muon Solenoid Experiment (CMS) . . . . .	40
4.4.1 Electromagnetic Calorimeter (ECAL) . . . . .	42
4.4.2 Hadronic Calorimeter (HCAL) . . . . .	47
4.4.3 Superconducting Solenoid . . . . .	51
4.4.4 Tracking . . . . .	51
4.4.5 Muon Chambers . . . . .	51
4.4.6 Trigger System . . . . .	51

<b>5 Studies of Displaced Jet Tagging Variables</b>	<b>55</b>
5.1 Introduction . . . . .	55
5.1.1 Significant differences with respect to b-tagging . . . . .	56
5.2 Samples . . . . .	57
5.3 Signal Samples . . . . .	57
5.4 Individual Variable Studies . . . . .	60
5.4.1 Impact Parameter Information . . . . .	60
5.4.2 Calo Jet Information . . . . .	70
<b>6 Displaced Jet Analysis</b>	<b>73</b>
6.1 Introduction . . . . .	73
6.2 Datasets . . . . .	74
6.3 An inclusive displaced-jet tagger . . . . .	74
6.3.1 Tagging Variable Cut Optimization . . . . .	79
6.4 Event selection . . . . .	80
6.5 Datasets and simulated samples . . . . .	81
6.6 Background prediction . . . . .	83
6.6.1 Signal Injection Tests . . . . .	86
6.6.2 Tag Probability Cross Validation . . . . .	92
6.7 Systematic uncertainties . . . . .	96
6.7.1 Background systematic uncertainties . . . . .	96
6.7.2 Signal systematic uncertainties . . . . .	96
6.8 Results and interpretation . . . . .	102
<b>Bibliography</b>	<b>116</b>

# Chapter 1

## Introduction

# Chapter 2

## Theory

### 2.1 On Standard Model of Particle Physics

#### Forward

It is the goal of this section to succinctly (in a relative sense) derive the principal aspects of the standard model of particle physics from fundamental principles. The questions to be answered are: how do we build a complex framework consisting of a variety of particles and interactions that experimentally describes the universe (neglecting gravity) with startling accuracy? what are the guiding principles? and despite its success, why is the theory incomplete?

First we will describe the lagrangian formulation of classical mechanics. From here we introduce, classical field theory and the fundamental quantization of quantum mechanics to arrive at quantum field theory (QFT). After a brief discussion of global and local lagrangian symmetries in a QFT, we discuss gauge theories and how local gauge symmetries give rise to the interactions mediating the fundamental forces excluding gravity. Ultimately, we review spontaneous electroweak symmetry breaking as the source of the gauge boson masses and the higgs field.

- Energy and The Principle of Minimal Action: Here we will build up the concept

- Symmetry and Local Gauge Symmetry: What symmetries do we enforce upon the form of our theory and what are the consequences.
- Theory Renormalizability: What limits the type of terms we can include in our lagrangian as to preserve the ability to calculate the outcomes of simple scattering processes.

### 2.1.1 Getting to Quantum Field Theory

#### Lagrangian Mechanics

In lagrangian mechanics, the time evolution of some generalized coordinate  $q$  can be determined via the principle of minimal action  $\delta S = 0$ .

$$S[q(t)] = \int_{t_1}^{t_2} L\left(q, \frac{dq}{dt}, t\right) dt$$

where  $S$  is a functional of the time dependent generalized coordinate  $q(t)$ . Let  $\dot{q} = \frac{dq}{dt}$   
The equations of motion are derived by varying  $S$

$$\delta S = \int_{t_0}^{t_1} \left[ \frac{\partial L}{\partial \dot{q}} \delta \dot{q} + \frac{\partial L}{\partial q} \delta q \right] dt$$

Note that  $\delta \dot{q} = \delta \frac{dq}{dt} = \frac{d(\delta q)}{dt}$ . Integrate the first term by parts, and require that  $\delta q$  vanish at the boundaries:

$$\int_{t_0}^{t_1} \left[ -\frac{d}{dt} \left( \frac{\partial L}{\partial \dot{q}} \right) \delta q + \frac{\partial L}{\partial q} \delta q \right] dt = \delta S = 0$$

by the principle of minimal action we have arrived at the euler equations of motion:

$$\frac{d}{dt} \left( \frac{\partial L}{\partial \dot{q}} \right) = \frac{\partial L}{\partial q}$$

For a generic lagrangian with potential energy term  $V(q)$ ,  $L = \frac{1}{2}m_q\dot{q}^2 - V(q)$  we obtain the equation of motion (or force law)  $F = m\ddot{q} = -\frac{dV}{dq}$

## Classical Field Theory

In comparison with classical mechanics, which deals with finitely many [cite:tong] general coordinates  $q_i$ , classical field theory deals with an infinite number of degrees of freedom  $\phi_i(\vec{x}, t)$  [cite:tong] with a degree of freedom for each spatial coordinate  $\vec{x}, t$  and index  $i$ . For simplicity we use a single index  $\mu$  for the four spacetime dimensions and utilize the einstein summation convention where repeated indicies are summed over. The corresponding action can be written in terms of a lagrangian density  $\mathcal{L}(\phi, \partial_\mu\phi)$

$$S = \int dt L = \int d^3x \int dt \mathcal{L}(\phi, \partial_\mu\phi) = \int dx^4 \mathcal{L}(\phi, \partial_\mu\phi)$$

Similarly, we arrive at classical Euler-Lagrange Equations of motion:

$$\partial_\mu \left( \frac{\partial \mathcal{L}}{\partial(\partial_\mu\phi)} \right) = \frac{\partial \mathcal{L}}{\partial\phi}$$

We now consider the simple free lagrangian density for a real scalar field  $\phi$ :

$$\mathcal{L} = \frac{1}{2}\partial_\mu\phi\partial^\mu\phi - \frac{1}{2}m\phi^2$$

we have achieved a relativistically invariance for free as all indicies are contracted. To see this, consider a lorentz transformation  $\Lambda$  on the kinetic term. The transformation induces  $\phi(x) \rightarrow \phi'(x) = \phi(\Lambda^{-1}x) = \phi(y)$ . The transformation is  $\Lambda$  as we actively rotate the coordinate system rather than rotating the field.

$$\partial_\mu\phi\partial^\mu\phi \rightarrow ((\Lambda^{-1})_\rho^\mu\partial^\rho\phi)((\Lambda^{-1})_\nu^\mu\partial_\nu\phi) = \eta^{\rho\nu}\partial_\rho\phi\partial_\nu\phi = \partial^\nu\phi\partial_\nu\phi$$

where we have used the fact that the spacetime metric is invariant under lorentz transformations.

$$\Lambda_\rho^\mu \eta^{\rho\lambda} \Lambda_\lambda^\nu = \eta^{\mu\nu}$$

As the action integrates over all space time, the change of variable from  $x \rightarrow y$  is inconsequential and yield the same equations of motion. Applying the euler lagrange equation we arrive at the classical relativistically invariant klein gordon equation:

$$(\partial^2 - m^2)\phi = 0$$

taking the fourier transform of state  $\phi$ :

$$\phi(\vec{x}, t) = \int \frac{d^3 p}{(2\pi)^3} e^{-i\vec{p}\cdot\vec{x}} \phi(\vec{p}, t)$$

Note that the  $(2\pi)^3$  is a normalization convention on the field. We see that the solution satsfies:

$$\left( \frac{\partial^2}{\partial t^2} + (p^2 + m^2) \right) \phi(\vec{p}, t) = 0$$

From this we recognize that this is just the equation of motion for a harmonic oscillator with energy  $\omega^2 = p^2 + m^2$

## The Canonical Quantization

Quantum mechanics consists of 4 fundamental postulates. Here we enumerate their classical counter parts [cite.schrednicki]

1. **Particle State:** In classical mechanics a the state of a particle is determined by two variables  $x(t)$  and  $p(t)$ . In quantum mechanics, the state is a vector  $|\psi\rangle$  in a hilbert space  $\mathcal{H}$
2. **Dynamic Variables :** Clasically, all dynamical variables are a function only  $x(t)$  and  $p(t)$ . In quantum mechanics, classical variables represented as a function of  $x$  and  $p$  are instead represented by hermitian operators  $X$  and  $P$  that statisfy the commutation relation  $[X, P] = \frac{i}{\hbar}$ .
3. **Measurement:** Clasically, the particle state is unaffected by measurement and strictly deterministic based on the values of  $x$  and  $p$ . Quantum mechanically, a particle in a state  $|\psi\rangle$  when measured will yield and eigenvalue  $\omega$  of the operator  $\Omega$  with probability  $|\langle\omega|\psi\rangle|^2$ . After measurement the particle state is the corresponding eigenvector  $|\omega\rangle$
4. **Time Evolution:** Classically,  $p$  and  $x$  change with time according to hamiltons (or lagrangian) equations of motion. Quantum mechanics asserts the state vector evolves with time according to the Schrodinger equation:  $i\hbar\frac{d}{dt}|\psi(t)\rangle = H|\psi(t)\rangle$ . Where  $H$  is the hamiltonian with classical  $p$  and  $q$  replaced by the corresponding quantum mechanical operators

The canonical quantization consists of the second postulate that that measurement of position and momentum do not commute (postulate 2). This is the source of the famous heisenburg uncertainty principle that there are no simultaneously measurable states of  $p$  and  $q$ .

If we consider the quantum harmonic oscillator with hamiltonian:

$$H = \frac{p^2}{2} + \frac{1}{2}\omega^2 q^2$$

and postulate the existence of the creation ( $a^\dagger$ ) and annihilation ( $a$ ) operators:

$$a = \sqrt{\frac{\omega}{2}}q + \frac{1}{\sqrt{2\omega}}p \quad a^\dagger = \sqrt{\frac{\omega}{2}}q - \frac{1}{\sqrt{2\omega}}p$$

which correspondingly give the

$$q = \frac{1}{\sqrt{2\omega}}(a + a^\dagger) \quad p = -i\frac{\omega}{2}(a - a^\dagger)$$

substituting into the hamiltonian we find a simple solution after applying the commutation relation  $[p, q] = -i$  (where we have set  $\hbar = 1$ ):

$$H = \omega(a^\dagger a + \frac{1}{2})$$

Importantly we see via the relation  $[H, a]|E\rangle = (E - \omega)a|E\rangle$  and  $[H, a^\dagger]|E\rangle = (E + \omega)a^\dagger|E\rangle$  that the operators raise and lower the harmonic oscillator in multiples of  $\omega$ . The energy levels are quantized in units of  $\omega$ . Also called ladder operators,  $a$  and  $a^\dagger$ , raise and lower the energy state by 1 unit of  $\omega$  with a ground state energy  $\frac{\omega}{2}$ .

If we now consider knowledge of classical field theory we can build a quantum field by promoting the coordinate  $q$  to a field  $\phi$ . We now write the solution to the Klein-Gordon equation as an infinite sum of creation and annihilation operators that create or destroy a particle with energy  $\omega_p^2 = p^2 + m^2$  designated by its four-momentum  $p$ . Taking the solution to Fourier space:

$$\phi = \int d^4x \frac{1}{\sqrt{2\omega_p}} [a_p e^{ipx} + a_p^\dagger e^{-ipx}]$$

Although this result only applies for a real scalar field (spin 0), the corresponding fermionic field (spin 1/2) field can be found similarly starting from the Dirac equation.

## 2.1.2 Symmetries

### Noether's Theorem

It cannot be understated the importance and the consequences of symmetries in the standard model. The invariance of the action (equivalently the equations of motion) under linear translations of the coordinates gives rise to conservation of momentum. Simillarly, rotations of the coordinate space yields the conservation of angular momentum. This is a consequence of noether's theorem, that every continuous symmetry of the action has a corresponding conservation law.

To be concrete, let us consider an action that is invariant under some field transformation  $\phi \rightarrow \phi + \delta\phi$ . If we consider a gauge transformation  $\phi \rightarrow e^{i\beta}\phi$  then the infinitesimal transformation is  $\delta\phi = i\beta\phi$ . Where we are taking for granted that  $\delta S = 0$  under this variation, or effectively  $\delta\mathcal{L}$  up to surface terms in the action integral. More on this later.

$$\begin{aligned}\delta\mathcal{L} &= \left[ \frac{\partial\mathcal{L}}{\partial\phi} \delta\phi + \frac{\delta\mathcal{L}}{\partial_\mu(\partial_\mu\phi)} \delta(\partial_\mu\phi) \right] \\ &= i\beta \left[ \frac{\partial\mathcal{L}}{\partial\phi} \phi + \frac{\partial\mathcal{L}}{\partial(\partial_\mu\phi)} (\partial_\mu\phi) \right]\end{aligned}$$

We futher require that the solution satisfying the euler-lagrange equations, and exchange the first term:

$$\begin{aligned}&= i\beta \left[ \partial_\mu \left[ \frac{\partial\mathcal{L}}{\partial(\partial_\mu\phi)} \right] \phi + \frac{\partial\mathcal{L}}{\partial_\mu\phi} (\partial_\mu\phi) \right] \\ &= i\beta \left[ \partial_\mu \left[ \frac{\partial\mathcal{L}}{\partial(\partial_\mu\phi)} \phi \right] \right] \\ &= \partial_\mu \left[ \frac{\partial\mathcal{L}}{\partial(\partial_\mu\phi)} \right]\end{aligned}$$

$$\partial_\mu j^\mu = 0$$

Where  $j^\mu$  is the conserved current corresponding to the continuous symmetry. Now consider the consequences for fermionic lagrangian:

$$\mathcal{L} = \bar{\psi}(i\gamma^\mu \partial_\mu - m)\psi$$

the corresponding current is  $j^\mu = i\bar{\psi}\gamma^\mu\psi = (\rho, \vec{j})$  where  $\rho$  is charge density and  $\vec{j}$  is electric current. We expand the index and  $\partial_\mu = (\frac{d}{dt}, \vec{\nabla})$  we obtain the continuity equation:

$$\frac{d\rho}{dt} + \nabla \cdot \vec{j} = 0$$

## Symmetry Groups and Algebras

cite.groups.resp.and.physics.HF.jones

To describe symmetry mathematically we need to discuss groups. A group is an algebraic structure (the field of math is known as abstract algebra and more specifically group theory) that consists of a set  $G$  (ex. Integers) and a pairwise operation (ex. multiplication)  $a \cdot b = c$  where  $a, b, c \in G$ . The group must also contain an identity  $i \in G$  (ex. 1) such that  $i \cdot g = g$  for all  $g \in G$ . All elements  $g \in G$  must have an inverse  $g^{-1} \in G$  such that  $g \cdot g^{-1} = g^{-1}g = i$ . The operation must additionally satisfy associativity  $(a \cdot b) \cdot c = a \cdot (b \cdot c)$ . Importantly, the group does not necessarily need to be abelian  $a \cdot b = b \cdot a$ , a common example in physics is generic matrix multiplication.

For example, we can consider the group of rotations  $SO(3)$  (read special orthogonal group of dimension 3) about the origin in euclidian  $\mathbb{R}^3$  under composition. Clearly the composition of two rotations is another rotation, the inverse rotation is just rotating back, and the identity is not rotation at all. The rotations can be represented by real 3 by 3 matrices, determinant  $\pm 1$ , where element inverses are their transpose

$g^{-1} = g^T$ . Interestingly, the group  $SU(2) \cong SO(3)/\mathbb{Z}_2$ , that is,  $SU(2)$  is a double covering of  $SO(3)$ . The isomorphism is exact

Specifically, a lie group is a continuous group with a multiplicative law that is a differentiable function of the parameters. linear combinations of generator elements:

$$e^{-i\vec{\beta} \cdot \vec{T}} = e^{-i\beta^i T^i} = U_G(\vec{\beta})$$

where the  $T^i$  are the generator elements. For instance, we can build rotations in 3 dimensional space using the dimension 2 representation by exponentiating the pauli spin matrices  $\vec{\sigma} = (\sigma_1, \sigma_2, \sigma_3)$  (note the conventional normalization) :

$$L_1 = \frac{\sigma_1}{2} = \frac{1}{2} \begin{pmatrix} 0 & 1 \\ 1 & 0 \end{pmatrix} \quad L_2 = \frac{\sigma_2}{2} = \frac{1}{2} \begin{pmatrix} 0 & -i \\ i & 0 \end{pmatrix} \quad L_3 = \frac{\sigma_3}{2} = \frac{1}{2} \begin{pmatrix} 1 & 0 \\ 0 & -1 \end{pmatrix}$$

In fact, generically the lie algebra of a group  $G$  is defined by the commutation relations of its generators  $T^i$ , specifically: ]

$$[T^i, T^j] = T^i T^j - T^j T^i = i c_{ijk} T^k$$

where  $c_{ijk}$  are known as the structure constants of the algebra. The algebra is abelian if and only if all  $c_{ijk} = 0$ . Otherwise, the  $c_{ijk}$  must be anti-symmetric in any of the two indices.

In particular to quantum field theory, the Poincare symmetry group plays an important role in the source of the most fundamental conservation laws and the statistics of the quantum fields. The poincare Symmetry group consists of transformations of the form:

$$x'_\mu = \lambda_\mu^\nu x_\nu + a_\mu$$

where  $\Lambda_\mu^\nu$  is a lorentz transformation from the lorentz group  $SO(3, 1)$  (boosts and rotations) and  $a_\mu$  is a translation consisting of 4 single 4-vector  $\mathbb{R}^{3,1}$ .

The generators of the Poincare group can be enumerated as generalized angular momentum operators:  $L_{\mu\nu} = i(x_\mu \partial_\nu - x_\nu \partial_\mu)$  with the commutation relations:

$$[L_{\mu\nu}, L_{\rho\sigma}] = -i(\eta_{\mu\rho}L_{\nu\sigma} - \eta_{\nu\sigma}L_{\mu\rho} + \eta_{\nu\sigma}L_{\mu\rho} - \eta_{\mu\rho}L_{\nu\sigma})$$

However, by decomposing the operators into rotations and boosts these relations become much simpler. Define:

$$J_i = \frac{1}{2}\epsilon_{ijk}L_{jk} \quad P_i = i\partial_i \quad K_i = L_{0i}$$

Where  $J$  and  $P$  are the familiar angular and linear momentum operators. We obtain more familiar commutations relations:

$$\begin{aligned} [J_i, J_j] &= i\epsilon_{ijk}J_k & [P_0, J_j] &= 0 \\ [P_i, J_j] &= i\epsilon_{ijk}P_k & [P_0, K_i] &= iP_i \\ [P_i, K_j] &= iP_0\delta_{ij} \end{aligned}$$

For a given lie algebra, the dimension of the representation of the group is physically related to the quadratic casimir. For a given concrete representation  $L_n$  for a  $n$  dimensional representation, the quadratic casimir  $C_2$  can be written as:

$$L_n^2 = C_2(L_n)I$$

where  $I$  is the identity. For example, for the group algebra for rotations  $SU(2)$  we define  $j$  as  $n = 2j + 1$  and consider the  $j = 0, 1/2$ , and  $1$  representations. For  $j = 0$  we have  $n = 1$  in which case, the rotation is always trivial to the state. For  $j = 1/2$

we have  $n = 2$  with the traceless generators:

$$L_1 = \begin{pmatrix} 0 & 0 & 0 \\ 0 & 0 & -i \\ 0 & i & 0 \end{pmatrix} \quad L_2 = \begin{pmatrix} 0 & 0 & i \\ 0 & 0 & 0 \\ -i & 0 & 0 \end{pmatrix} \quad L_3 = \begin{pmatrix} 0 & -i & 0 \\ i & 0 & 0 \\ 0 & 0 & 0 \end{pmatrix}$$

The lorentz group can further be decomposed into  $SO(3,1) \cong SU(2) \times SU(2)$  where  $SU(2)$  is the group of matrices with determinant  $\pm 1$  where the inverses are the conjugate transpose:  $g^{-1} = (g^T)^*$ . The fundamental fields in the SM lagrangian are characterized by the four corresponding combinations of  $SU(2)$  representations. The  $(0,0)$  representation of  $SU(2) \times SU(2)$  corresponds to scalar spin 0 fields  $\phi$ . The two chiral representations  $(1/2,0)$  and  $(0,1/2)$  correspond to fermionic matter fields  $\psi$ . The  $(1/2,1/2)$  representation corresponds to the fundamental vector boson fields  $W_\mu, B_\mu, G_\mu$  and the fields after electroweak symmetry breaking.  $W^\pm, Z^0, A_\mu$ .

Let us now consider a field transformation  $\phi_a \rightarrow \phi'_a$  under some lie algebra with generators  $L_i$  such that the transformation is  $U_g(\beta)$ . Consider the heisenburg picture of quantum mechanics where operators evolve but the states remain fixed.

$$\langle O' \rangle = \langle \psi | U_g^{-1}(\beta) O U_g(\beta) | \psi \rangle$$

$$O' = U_g^{-1}(\beta) O U_g(\beta)$$

we obtain a transformed quantum field:

$$\phi'_a = e^{-i\vec{\beta} \cdot \vec{T}} \phi_a e^{-i\vec{\beta} \cdot \vec{T}}$$

expanding the exponentials we see that:

$$\phi'_a = \phi_a - i[\vec{\beta} \cdot \vec{T}, \phi_a] + \frac{(-i)^2}{2} [\vec{\beta} \cdot \vec{\tau}, [\vec{\beta} \cdot \vec{T}, \phi_a]] + O(\beta^2)$$

Where  $L^i$  is the concrete representation of  $T^i$ . applying  $[T^i, \phi_a] = -L_{ab}^i \phi_b$  gives the field transformation law:

$$\phi'_a = \left( e^{i\vec{\beta} \cdot \vec{L}} \right)_{ab} \phi_b$$

and similarly the conjugate field  $\phi_a^\dagger$  transforms in the adjoint representation:

$$\phi_a^\dagger = \left( e^{-i\vec{\beta} \cdot \vec{L}} \right)_{ab} \phi_b^\dagger$$

### Local Gauge Invariance and the Covariant Derivative

cite-peskin-pg482 Lets consider what happens when we promote the lagrangian symmetry of fields under the Standard Model gauge symmetries to a local symmetry. Local in the sense that a space dependent transformation for example, the  $U(1)$  gauge symmetry transforms the field  $\psi$  as:

$$\psi(x) \rightarrow e^{-\alpha(x)} \psi(x)$$

If we then consider a direction derivative in the direction  $n^\nu$  as defined:

$$n^\mu \partial_\mu \psi(x) = \lim_{\epsilon \rightarrow 0} \frac{\psi(x + \epsilon n) - \psi(x)}{\epsilon}$$

This is not going to have a simple transformation law, since the two states are not at the same point in sample time. We need a connection such that we have a simple transformation law. Consider:

$$n^\mu \partial_\mu \psi(x) = \lim_{\epsilon \rightarrow 0} \frac{1}{\epsilon} (\psi(x + \epsilon n) - U(x + \epsilon n, x) \psi(x))$$

where  $U(x, y)$  is our connection and transforms as:

$$U(x, y) \rightarrow e^{i\alpha(x)} U(x, y) e^{-i\alpha(y)}$$

such that when we apply the transformation to the directional derivative we obtain:

$$n^\mu \partial_\mu \psi(x) = \lim_{\epsilon \rightarrow 0} \frac{1}{\epsilon} e^{i\alpha(x+n\epsilon)} (\psi(x + \epsilon n) - U(x + \epsilon n, x) \psi(x))$$

Now lets expand the transformation for an infinitesimal  $\epsilon$ :

$$\begin{aligned} U(x + \epsilon n, x) &\approx U(x, x) + c\epsilon n^\mu A_\mu(x) + O(\epsilon^2) \\ &= 1 + c\epsilon n^\mu A_\mu(x) + O(\epsilon^2) \end{aligned}$$

Where we have used the fact that the connection between  $x$  and itself is trivial and specified some arbitrary (but very suggestive of our final answer) constant  $c = ie$ . If we would then like to see how this field  $A_\mu$  transforms we need to check the  $U(x, y)$  transformation:

$$\begin{aligned} e^{i\alpha(x)} U(x + \epsilon n, x) e^{-i\alpha(y)} &= (1 + i\alpha(x + n\epsilon))(1 - ie\epsilon n^\mu A_\mu)(1 - i\alpha(x)) \\ &= 1 + i\alpha(x + n\epsilon) - ie\epsilon n^\mu A_\mu - i\alpha(x) \end{aligned}$$

comparing this to the expansion of  $U(x + \epsilon n, x)$  we see:

$$\begin{aligned} 1 + ie\epsilon n^\mu A_\mu(x) &= 1 + i\alpha(x + n^\mu \epsilon) - ie\epsilon n^\mu A_\mu(x) - i\alpha(x) \\ A_\mu(x) &= \left[ \frac{\alpha(x + n^\mu \epsilon) + \alpha(x)}{en^\mu \epsilon} + A_\mu(x) \right] \\ A_\mu(x) &= \left[ -\frac{1}{n^\mu} \frac{1}{e} \partial_\mu \alpha(x) + A_\mu(x) \right] \end{aligned}$$

If we pick the axes such that  $n^\mu = 1$  then we have the transformation law for the gauge field:  $A_\mu(x) \rightarrow A_\mu(x) - \frac{1}{e}\partial_\mu\alpha(x)$ .

### 2.1.3 Sectors of the Standard Model Lagrangian

The Standard Model of particle physics consists of a quantum field theory lagrangian with four sectors. and three gauge group symmetries:  $U(1)_Y$  hypercharge,  $SU(2)_L$  left chiral and  $SU(3)_c$  color.

$$\begin{aligned}\mathcal{L}_{SM} &= \mathcal{L}_{Gauge} + \mathcal{L}_{Fermion} + \mathcal{L}_{Higgs} + \mathcal{L}_{Yukawa} \\ &= \left(-\frac{1}{4}F_{\mu\nu}F^{\mu\nu}\right) + (\bar{\psi}i\gamma^\mu\partial_\mu\psi) + \left(\frac{1}{2}(\partial_\mu\phi)^2 + V(\phi)\right) + (\bar{\psi}_iy_{ij}\psi_j\phi)\end{aligned}$$

All standard model particles transform as a multiplet of  $SU(3) \times SU(2)_L \times U(1)_Y$ .

#### Gauge Sector

The gauge sector consists of the field stress energy tensor of the 3 corresponding types of gauge bosons:  $G^i$  (gluons of the color force),  $W^i$  ( $W$ 's of the weak force) and  $B$  (of the weak hypercharge). Here the index  $i$  enumerates their multiplicity. There are 8 gluons, 3  $W$ 's and a single  $B$ . Ultimately, we will arrive have 8 gluons,  $W^\pm$  and the photon  $A^\mu$  because the  $SU(2) \times U(1)$  symmetry is spontaneously broken and the scalar  $\phi$  takes on a new vacuum state. More on this later.

$$\mathcal{L}_{Gauge} = -\frac{1}{4}F_{\mu\nu}^iF^{\mu\nu i} = -\frac{1}{4}G_{\mu\nu}^iG^{\mu\nu i} - \frac{1}{4}W_{\mu\nu}^iW^{\mu\nu i} - \frac{1}{4}B_{\mu\nu}B^{\mu\nu} \quad (2.1)$$

where the double scripts correspond to the commutation relations for the gauge group algebra.

$$X_{\mu\nu}^i = [D_\mu X_\nu, D_\nu X_\mu] = \partial_\mu X_\nu^i - \partial_\nu X_\mu^i - g f_{ijk} X_\mu^j X_\nu^k \quad (2.2)$$

where  $g$  is the coupling constant, the  $D_\mu$  terms correspond to the covariant derivative and the  $f_{ijk}$  are the corresponding structure constants for the non-abelian groups

that arise from the non commuting generators of the algebra when computing the commutator. In full, the field stress tensor terms are:

$$\begin{aligned} G_{\mu\nu}^i &= \partial_\mu G_\nu^i - \partial_\nu G_\mu^i - g_s f_{ijk} G_\mu^j G_\nu^k \\ W_{\mu\nu}^i &= \partial_\mu W_\nu^i - \partial_\nu W_\mu^i - g \epsilon_{ijk} W_\mu^j W_\nu^k \\ B_{\mu\nu} &= \partial_\mu B_\nu - \partial_\nu B_\mu \end{aligned}$$

### **Yukawa Sector**

The fermion sector consists of the kinetic energy terms for each quark (up and down types) and leptons (lepton, neutrinos) in the standard model. The left handed quarks transform as an  $SU(2)$  doublet:

$$q_{mL\alpha}^0 = \begin{pmatrix} u_{m\alpha}^0 \\ d_{m\alpha}^0 \end{pmatrix}_L \quad \text{and} \quad l_{mL} = \begin{pmatrix} \nu_m^0 \\ e_m^{-,0} \end{pmatrix}_L \quad (2.3)$$

where the subscript  $m$  denotes the family (1st, 2nd and 3rd generation) and  $\alpha$  denotes the color charge (red, green, and blue). As the  $SU(2)_L$  symmetry only acts on the left handed fermions we further separate the fermion sector into left and right components:

$$\begin{aligned} \mathcal{L}_{fermion,L} &= \bar{q}_{mL}^0 i\gamma^\mu D_\mu q_{mL}^0 + \bar{l}_{mL}^0 i\gamma^\mu D_\mu l_{mL}^0 \\ \mathcal{L}_{fermion,R} &= \bar{u}_{mR}^0 i\gamma^\mu D_\mu u_{mR}^0 + \bar{d}_{mR}^0 i\gamma^\mu D_\mu d_{mR}^0 + \bar{e}_{mR}^0 i\gamma^\mu D_\mu e_{mR}^0 + \bar{\nu}_{mR}^0 i\gamma^\mu D_\mu \nu_{mR}^0 \end{aligned}$$

### **Higgs Sector**

The higgs sector consists of terms related to the single scalar field  $\phi$ :

$$\mathcal{L}_{higgs} = (D^\mu \phi)^\dagger (D_\mu \phi) + \mu^2 \phi^\dagger \phi + \lambda (\phi^\dagger \phi)^2 \quad (2.4)$$

## 2.1.4 Electroweak Symmetry Breaking (EWSB)

Expanding the kinetic term for the field phi about the vaccum  $\langle \phi \rangle = \nu$  in the gauged theory we find:

$$(D^\mu \phi)^\dagger (D_\mu \phi) = \frac{1}{\sqrt{2}} \begin{pmatrix} 0 & \nu \end{pmatrix} \left| \partial_\mu + ig \frac{\tau}{2} \cdot W_\mu + i \frac{g'}{2} B_\mu \right|^2 \frac{1}{\sqrt{2}} \begin{pmatrix} 0 \\ \nu \end{pmatrix}$$

Considering only the the square gauge field terms (ignoring the derivative) we obtain the matrix:

$$\tau \cdot W + g' B_\mu I = \begin{pmatrix} W_{\mu,3} & W_{\mu,1} - iW_{\mu,2} \\ W_{\mu,1} + iW_{\mu,2} & -W_{\mu,3} \end{pmatrix}$$

adding in the diagonal  $B_\mu$  terms and taking the square:

$$(D^\mu \phi)^\dagger (D_\mu \phi) = \frac{\nu^2}{8} [g^2(W_1^2 + W_2^2) + (g' B_\mu - g W_{\mu,3})^2]$$

Now if we perform a redefinition of the gauge fields into mass eigenstates we arrive at a clean expression:

$$\begin{aligned} W_\mu^\pm &= \frac{1}{\sqrt{2}} (W_{\mu,1} \pm iW_{\mu,2}) \\ A_\mu &= \frac{1}{\sqrt{g^2 + (g')^2}} (g' W_{\mu,3} + g B_\mu) = \sin \theta_W W_\mu^3 + \cos \theta_W B_\mu \\ Z_\mu &= \frac{1}{\sqrt{g^2 + (g')^2}} (g' B_\mu - g W_{\mu,3}) = \sin \theta_W B_\mu - \cos \theta_W W_\mu^3 \end{aligned}$$

Table 2.1: Standard Model particle representations under the symmetry groups  $SU(2)$  and  $SU(3)$  respectively  $n_2$  and  $n_3$ . Also listed is associated electroweak hypercharge  $Y$  as well as the electric charge  $Q$

	$q_L$	$l_L$	$u_R$	$d_R$	$e_R$	$\nu_R$
$n_3$	3	1	3	3	1	1
$n_2$	2	2	1	1	1	1
$Y_{U(1)}$	1/6	-1/2	2/3	-1/3	-1	0
$Q = Y + T_L^3$	2/3	-1/3	2/3	-1/3	-1	0

Here we have defined the electroweak mixing angle  $\theta_W$  in terms of a right triangle with legs  $g$  and  $g'$ . With this substitution,

$$\begin{aligned} (D^\mu \phi)^\dagger (D_\mu \phi) &= \frac{\nu^2 g^2}{4} W_\mu^- W_\mu^+ + \frac{(g+g')\nu^2}{8} Z_\mu^2 + 0 \times A_\mu^2 \\ &= \frac{1}{2} m_W^2 W_\mu^- W_\mu^+ + \frac{1}{2} m_Z^2 Z_\mu^2 + 0 \times A_\mu^2 \end{aligned}$$

Electroweak symmetry breaking has generated the mass terms for the gauge bosons!  $m_{W^\pm} = \frac{\nu g}{\sqrt{2}} = 90.385$  [GeV],  $m_Z = \frac{\nu}{2} \sqrt{g+g'} = \frac{m_W}{\cos \theta_W} = 91.1876$  [GeV] and the massless photon  $A_\mu$ .

### 2.1.5 Divergences in the Standard Model

To explain why we need a mechanism like EWSB to generate the masses for the gauge bosons, we need to understand how we have motivated the terms of the Standard Model Lagrangian.

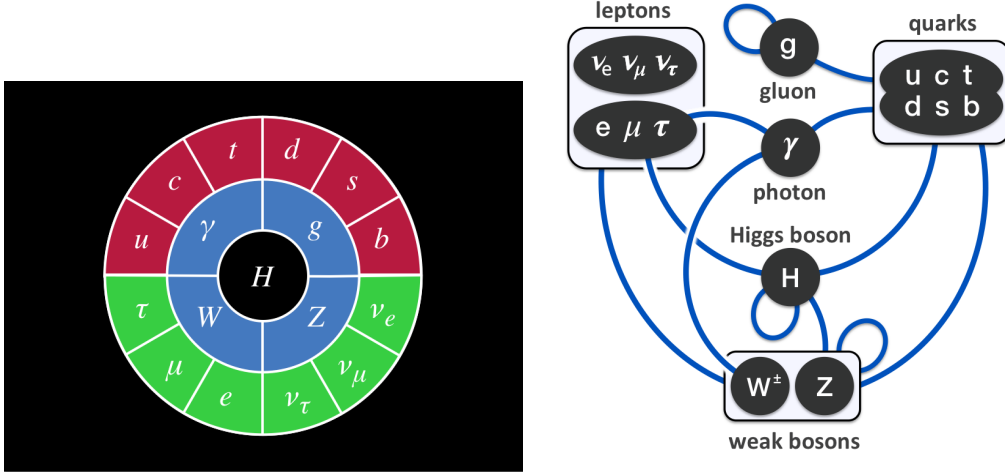


Figure 2.1

Table 2.2: cite-tully-particle: The types of terms included in the Standard Model Lagrangian

Field	Lagrangian Term	Field Dim. [Mass]
Scalar Field	$(1/2)(\partial_\mu \phi)(\partial^\mu \phi)$	$[\phi] = M^2$
Dirac Field	$\bar{\psi} M \psi$	$[\psi] = M^{3/2}$
Field Stress Tensor	$-(1/4)F_{\mu\nu}F^{\mu\nu}$	$[F_{\mu\nu}] = M^2$
Vector Field	$F_{\mu\nu} = \partial_\mu A_\nu - \partial_\nu A_\mu$	$[A_\mu] = M$
Coupling Type	Lagrangian Term	Coupling Dim [Mass]
Gauge Coupling	$g\bar{\psi}\gamma_\mu\psi A^\mu$	$[g] = 1$
Triple Gauge Coupling	$A_\mu^\mu \partial_\nu A^\nu$	$[g] = 1$
Quartic Gauge Coupling	$g^2(A_\mu A^\nu)^2$	$[g] = 1$
Yukawa Coupling	$g\bar{\psi}\psi\phi$	$[g] = 1$
Scalar Coupling w/ Gauge Bosons	$\tilde{g}A_\mu A^\mu \phi$	$[\tilde{g}] = M$
	$gA_\mu(\partial^\mu \phi)\phi$	$[g] = 1$
Scalar self-couplings	$\tilde{g}\phi^3$	$[\tilde{g}] = M$
	$g\phi^4$	$[g] = 1$

## 2.1.6 Fundamental Fields and Free Parameters of the Standard Model

## 2.1.7 Re-deriving Maxwell's Laws

After electroweak symmetry breaking we would like to perform a sanity check that we can revive the well established equations of Maxwell governing electrodynamics. Keeping only the terms that contain the field  $A_\mu$ :

$$\mathcal{L}_{EM} = -\frac{1}{4}F_{\mu\nu}F^{\mu\nu} - ie\bar{\psi}\gamma^\mu A_\mu\psi \text{ for } F_{\mu\nu} = \partial_\mu A_\nu - \partial_\nu A_\mu$$

where by definition  $F_{\mu\nu} = \partial_\mu A_\nu - \partial_\nu A_\mu$ . Applying the left side of Euler-Lagrange we find:

$$\partial_\mu \left( \frac{\partial \mathcal{L}}{\partial(\partial_\mu A_\nu)} \right) = -\frac{1}{2}\partial_\mu \left[ \left( \frac{\partial}{\partial(\partial_\mu A_\nu)} F_{\mu\nu} \right) F^{\mu\nu} \right] = -\frac{1}{2}\partial_\mu [(1 - \delta_\nu^\mu)F^{\mu\nu}] = -\frac{1}{2}\partial_\mu F^{\mu\nu}$$

The other term is simply  $\frac{\partial \mathcal{L}}{\partial A_\mu} = -ie\bar{\psi}\gamma^\mu\psi = J^\mu = (\rho, \vec{J})$ . Where  $\rho$  is charge density and  $\vec{J}$  is current. This yields our first equation:

$$\partial_\nu F^{\nu\mu} = J^\mu \tag{2.5}$$

recognizing the field stress tensor is antisymmetric we can apply a partial derivative and contract with the indices of the 4 dimensions anti-symmetric symbol to obtain:

$$\epsilon_{\theta\rho\mu\nu}\partial\rho F_{\mu\nu} = 0 \tag{2.6}$$

Using these two laws and suggestively defining  $E^i = F^{0i}$  and  $\epsilon^{ijk}B^k = F^{jk}$  simple substitution

Don't forget that the assumptions to get here were simply the existence of energy terms for the field stress tensor and the fermionic field  $\psi$  (here the electron) and geometric arguments about the continuity in the derivative under the  $U(1)$  gauge symmetry in the Lagrangian. Everything we understood about electromagnetism naturally arises (including the gauge freedom of the field  $\vec{A}$ ). Thats just awesome.

## 2.2 Beyond the Standard Model

### 2.2.1 Problems with the Standard Model

### 2.2.2 Supersymmetry

### 2.2.3 Electroweak Symmetry Breaking in Supersymmetric Theories

## 2.3 Origins of Long-lived Signatures

### 2.3.1 Standard Model Particles with Long Lifetimes

The standard model already includes a variety of particles that can generate displaced vertices (Table 2.3 Table 2.4). For example,  $B^0 \rightarrow J/\psi K^{*0}$  with  $K^{*0} \rightarrow K^+ \pi^-$  generates a 4 track vertex. Such a vertex is commonly utilized in b-tagging. Of particular interest to single displaced jet identification outside of the b-tagging regime are charge neutral SM particles decaying to charged particles with a few centimeter lifetime:  $\Lambda^0$ ,  $K_S^0$ . Such particles would have no track leading to the primary vertex and vertices far outside the b lifetime. The most relevant of processes being:

1.  $K_s^0 \rightarrow \pi^+ \pi^-$  69% of all  $K_s^0$  decays

Name	Content	Particle	Mass [MeV]	$\tau_0$ [sec]	$c\tau$ [cm]
Pion	$ud$	$\pi^\pm$	139	$2.6 \times 10^{-8}$	$7.8 \times 10^2$
Kaon	$u\bar{s}$	$K^\pm$	497	$1.23 \times 10^{-8}$	$3.7 \times 10^2$
K Short	$\frac{1}{\sqrt{2}}(d\bar{s} - s\bar{d})$	$K_s^0$	497	$0.896 \times 10^{-10}$	2.68
K Long	$\frac{1}{\sqrt{2}}(d\bar{s} + s\bar{d})$	$K_L^0$	497	$5.1 \times 10^{-8}$	$1.5 \times 10^3$
D	$c\bar{d}$	$D^\pm$	1869	$1 \times 10^{-12}$	$3.0 \times 10^{-2}$
B meson	$ub$	$B^\pm$	5279	$1.6 \times 10^{-12}$	$4.8 \times 10^{-2}$
strange B	$s\bar{b}$	$B_s^0$	5366	$1.5 \times 10^{-12}$	$4.5 \times 10^{-2}$
charmed B	$c\bar{b}$	$B_c^0$	6275	$4.5 \times 10^{-13}$	$1.4 \times 10^{-2}$

Table 2.3: Mesons with proper lifetimes greater than  $10^{-2}$  cm

Name	Content	Particle	Mass [MeV]	$\tau_0$ [s]	$c\tau_0$ [cm]
Lambda	$uds$	$\Lambda^0$	1115	$2.6 \times 10^{-10}$	7.8
bottom Lambda	$edb$	$\Lambda_b^0$	5620	$1.4 \times 10^{-12}$	$4.2 \times 10^{-2}$
Sigma plus	$uus$	$\Sigma^+$	1189	$8 \times 10^{-11}$	2.4
Sigma minus	$dds$	$\Sigma^-$	1197	$1.4 \times 10^{-10}$	4.2
Xi zero	$uss$	$\Xi^0$	1314	$4 \times 10^{-13}$	$1.2 \times 10^{-2}$
Xi minus	$dss$	$\Xi^-$	1321	$1.6 \times 10^{-10}$	4.8
charmed Xi +	$usc$	$\Xi_c^+$	2467	$4.42 \times 10^{-13}$	$1.3 \times 10^{-2}$
charmed Xi	$dsc$	$\Xi_c^0$	2471	$1.12 \times 10^{-13}$	$3.3 \times 10^{-2}$
bottom Xi	$dsb$	$\Xi_b^-$	5792	$1.56 \times 10^{-12}$	$4.7 \times 10^{-2}$
bottom Omega	$ssb$	$\Omega_b^-$	6054	$1.13 \times 10^{-12}$	$3.3 \times 10^{-2}$
Omega minus	$sss$	$\Omega^-$	1672	$8 \times 10^{-11}$	2.4

Table 2.4: Baryons with proper lifetimes greater than  $10^{-2}$  cm

2.  $\Lambda^0 \rightarrow p\pi^-$  64% of all  $\Lambda^0$  decays

Jets containing prompt and non-prompt  $K_s$  and  $\Lambda^0$  will contain tracks with large impact parameters, and large impact parameter significance. When a vertex is fit to the matched tracks we expect small track multiplicity relative to the GeV to TeV long-lived particles this identification targets. It is important to separate this contribution from the detector effects like nuclear interactions.

Particles of a characteristic lifetime  $\tau$  decay with a falling exponential. For reference, a table describing the percent of decays that will occur at various distances is shown in Table 2.5. Even lifetimes 10 and 100 times the size of the tracker, we would

Distance ( $\lambda$ )	Probability of Decay
0.01	1%
0.1	9.5%
0.25	22%
0.5	39%
0.75	52%
1	63%
1.5	77%
2	86%
3	95%
5	99.3%

Table 2.5: A reference table for the cumulative probability for a particle of lifetime  $\lambda$  to have decayed after a given distance. Distance is in multiples of lambda.

still expect 10% and 1% respectively to occur within the tracker. For particles of lifetime  $\lambda$  we expect 0.6% to decay beyond  $5\lambda$ .

### 2.3.2 Split-Susy and Naturalness at the LHC

The expectation of discovering supersymmetry (SUSY) at the TeV scale has been largely motivated by arguments based on naturalness. Since the mass of the Standard Model Higgs boson is sensitive to the high energy scale where SUSY is broken ( $m_{SUSY}$ ), its mass, of order the electroweak scale, ( $m_h \approx m_{EW} \ll m_{SUSY}$ ) would need to be tuned to order  $m_{EW}^2/m_{SUSY}^2$ . To avoid fine-tuning, we would like  $m_h^2 \approx m_{SUSY}^2 \implies m_{SUSY} \leq 1$  TeV. More specifically, knowing  $m_H \approx 125$  GeV we expect light SUSY partners (in particular, light stops) near  $< 1$  TeV to stabilize the quadratic divergences of 1 loop corrections to the Higgs mass [citation:*light\_stops*]. Unfortunately these scalar partners have yet to be discovered.

It is important to note that the stability of the Higgs boson mass is not the only fine-tuning problem in particle physics. When the same argument is made for the cosmological constant we arrive at  $\Lambda \geq m_{SUSY}^4$ , where experimentally  $\Lambda = 10^{-59}$

TeV<sup>4</sup>. If we use the same SUSY scale as we did for the Higgs mass,  $m_{SUSY} = 1$  TeV we have a new fine tuning problem of  $10^{60}$ .

As addressed by Arkani-Hamed and Dimopoulos [citation:*nima\_lhc*], many theoretical approaches have been motivated by a natural explanation for the Higgs mass while separately seeking an explanation of the cosmological constant through some other mechanism. Arkani-Hamed and Dimopoulos propose a reconsideration of naturalness, entertaining the idea that fine tuning could have a role to play in beyond the Standard Model physics. Conceivably, both  $\Lambda$  and  $m_h$  fine tuning could be resolved by the same mechanism. This un-natural model was further investigated by Giudice and Romanino [citation:*split\_susy*] and dubbed “split supersymmetry”.

Split SUSY assumes a much higher SUSY scale  $m_{SUSY}^2 \gg 1$  TeV where all scalars (excluding the Higgs) become very heavy  $O(m_{SUSY})$  and the lightest sparticles (Higgsinos and gluinos) are kept at the TeV scale by requiring the lightest neutralino to be a good dark matter candidate.

Because the scalars are so much heavier, the decay of gluinos through squarks is suppressed. The characteristic signature of split supersymmetry is thus long-lived gluinos; such processes with long lifetimes are rare in the SM.

# Chapter 3

## Collider Physics and Phenomenology

### 3.1 Introduction

In the previous chapter, we outlined how we reach a theory like the standard model from fundamental principles, but a considerable amount of physics is required to reach a practical theoretical description of what occurs inside of the experiment. The goal of this section is to connect the matrix elements  $\mathcal{M}$  from the quantum field theoretic description of the Standard Model to the Monte Carlo simulations used to test a given theory. First, we will discuss the how we can compare the matrix amplitudes with the observations in a physical detector. After, we will discuss the considerations that must be made for the fact the LHC collides hadrons rather than fundamental particles. Finally, we will discuss the framework used to describe the particles actually observed in the detector after the hard scattering occurs where perturbative physics breaks down and calculations from first principles cannot be performed. Generic principles for parton showering and hadronization models will be examined.

### 3.1.1 From Matrix Elements to Cross Sections

In high energy experimental particle physics the key quantity (besides particle quantum numbers and masses) is the cross section  $\sigma$  of the process. This is the rate or in essence, the probability that an event occurs. It is the proportionality between the number of observed collisions and the rate at which the Large Hadron Collider delivers collisions  $L$  (the luminosity) expressed simply as:

$$N_{events} = L \times \sigma$$

site-peskin Consider a target of particles type  $A$  and density  $\rho_A$  and aim particles type  $B$  with density  $\rho_B$ . If the lengths of the bunches of particles are  $l_A$  and  $l_B$  then the cross section of the processes is defined for a beam with cross-sectional area as:

$$\sigma \equiv \frac{N_{events}}{\rho_A l_A \rho_B l_B A}$$

Inverting this and assuming that we have constant density along the beams length:

$$N_{events} = \frac{\sigma N_A N_B}{A} = \sigma N_A n_B \quad (3.1)$$

by comparing this with the relation for  $N_{events}$  above containing luminosity, we see the luminosity is in effect counting the number of colliding particles per unit area. More incident particles and a more focused beam means more scattered events. In the last equality we have introduced the impact parameter density  $n_B$  for the incident  $B$  particles.

However, the the end results of feynman diagram calculations yield scattering amplitudes which are matrix elements of scattering a given intial state into a given final state, not a cross section. We have to further develop the stocastic interaction of two particles into something more concrete experimentally.

First, we need must think about the quantum fields within the beams that are colliding. To do so we set up two initial wave packets  $A$  and  $B$  in a limit of definite momentum  $p_A$  and  $p_B$  and evolve them for a very long time with the time evolution operator  $\exp(-iHt)$  and then consider the final state wave packets with the correct final state particles. This in turn will give us the probability amplitude for producing that final state.

$$\mathcal{P} = |\langle \phi_1 \phi_2 \dots | \phi_A \phi_B \rangle|^2$$

Now consider the number of incident particles colliding along the  $z$ -axis, but with non-trivial transverse displacement, also referred to as impact parameters  $b_i$ . We will take the perspective that  $A$  is a target and  $B$  is collinear with the target and account for the shift in position with an explicit factor of  $\exp(-ib \cdot k_B)$ . The properly normalized expression then reads:

$$|\phi_A \phi_B\rangle = \int \frac{d^3 k_A}{\sqrt{2E_A}(2\pi)^3} \int \frac{d^3 k_B}{\sqrt{2E_B}(2\pi)^3} \phi_A(k_A) \phi_B(k_B) e^{-ib \cdot k_B}$$

For a single target  $A$  and a beam  $B$  with constant impact parameter density  $n_B = N_B/A$  we can write the the number of events as

$$N_{events} = \sum_{\text{incident particles } i} \mathcal{P}_i = \int d^2 b n_B(b) \mathcal{P}(b) = n_B \int d^2 b \mathcal{P}(b)$$

Comparing this to Equation 3.1 we can write the cross section as:

$$\sigma = \int d^2 b \mathcal{P}(b)$$

and the properly normalized differential cross section for scattering into a the infinitesimal final state momentum element is:

$$d\sigma = \left( \prod_f \frac{d^3 p_f}{(2\pi)^3 2E_f} \right) \int d^2 b \left( \prod_{i=A,B} \int \frac{d^3 k_i}{(2\pi)^3 \sqrt{2E_i}} \phi_i(k_i) \int \frac{d^3 \bar{k}_i}{(2\pi)^3 \sqrt{2\bar{E}_i}} \phi_i^*(\bar{k}_i) \right) \\ \times e^{ib \cdot (\bar{k}_S - k_B)} |\langle \{p_f\} | \{k_i\} \rangle|^2$$

We have 6 dummy integrals to do in  $\bar{k}$  over the 3 momentums of particle  $A$  and  $B$  so count our delta functions. The  $d^2 b$  integral gives 2 delta functions in the transverse momentum  $(2\pi)^2 \delta^2(k_B^\perp - \bar{k}_B^\perp)$ . We have 8 delta functions from the matrix element enforcing that the process to conserve energy and momentum  $\delta^4(k_A + k_B - \sum p_f)$  and in the complex conjugate with the dummy variable  $\bar{k}$ :  $\delta^4(\bar{k}_A + \bar{k}_B - \sum p_f)$ . Performing the transverse integrals in  $\bar{k}_B$  sets  $\bar{k}_B^T = k_B^T$  which in combination with the transverse barred amplitude delta functions give  $\bar{k}_A^T = k_A^T$ . The remaining 2 integrals in  $z$  require some properties of delta functions:

$$\int d\bar{k}_A^z d\bar{k}_B^z \delta(\bar{k}_A^z + \bar{k}_B^z - \sum p_f^z) \delta(\bar{E}_A + \bar{E}_B - \sum E_f)$$

We can integrate the first  $B$  integral considering  $\bar{k}_B^z$  to be a function of  $\bar{k}_A^z$  and writing the barred energy terms in the momentums and masses:

$$\int d\bar{k}_A^z \delta \left( \sqrt{\bar{k}_A^2 + m_A^2} + \sqrt{\bar{k}_B^2 + m_B^2} - \sum E_f \right)$$

We now need to use the property that  $\delta[f(x)] = \sum_i (\delta(x_i)/f'(x_i))$  where  $x_i$  are the zeros of the function  $f(x)$ . Note that given our parameterization from the first delta

function  $\partial_{\bar{k}_A^z}(\bar{k}_B^2) = -2\bar{k}_B^z$ .

$$\begin{aligned} & \int d\bar{k}_A^z \left( \frac{1}{2} \frac{2\bar{k}_A}{\sqrt{\bar{k}_A^2 + m_A^2}} - \frac{1}{2} \frac{2\bar{k}_B}{\sqrt{\bar{k}_B^2 + m_B^2}} \right)^{-1} \delta(\bar{E}_A + \bar{E}_B - \sum E_f) \\ &= \frac{1}{\frac{\bar{k}_A}{E_A} - \frac{\bar{k}_B}{E_B}} \delta(\bar{E}_A + \bar{E}_B - \sum E_f) = \frac{1}{\beta_A - \beta_B} \end{aligned}$$

The 6 remaining integrals in  $k_A$  and  $k_B$  remain:

$$\begin{aligned} d\sigma = & \left( \prod_f \frac{d^3 p_f}{(2\pi)^3 2E_f} \right) \frac{|\mathcal{M}|^2}{2E_A 2E_B |\beta_A - \beta_B|} \int \frac{d^3 k_A}{(2\pi)^3 \sqrt{2E_i}} |\phi_A(k_A)|^2 \\ & \times \int \frac{d^3 k_B}{(2\pi)^3 \sqrt{2E_i}} |\phi_B(k_B)|^2 \delta^4(k_A + k_B - \sum p_f) \end{aligned}$$

To proceed further, we must consider the quality of measurements made by particle detectors. Real detectors cannot measure arbitrarily small spreads in the momentums  $k_A + k_B$ . The measurements made in a realistic experimental setup are not sensitive to the spread of momentum in the initial wave packets  $\phi_A$  and  $\phi_B$ . Given this, we can take the central value  $k_A + k_B = p_A + p_B$  to be a good approximation for the delta function. With this approximation, we can move the delta function outside the integral and perform the integrals using the unit normalization condition of the two fields  $\phi_i$ :

$$d\sigma = \left( \prod_f \frac{d^3 p_f}{(2\pi)^3 2E_f} \right) \frac{|\mathcal{M}|^2}{2E_A 2E_B |\beta_A - \beta_B|} (2\pi)^4 \delta^4(p_A + p_B - \sum p_f) \quad (3.2)$$

Let's consider the simple case of  $2 \rightarrow 2$  scattering and use the energy delta function of the 4 remaining delta functions to compute integral over the final state. To do so, we go to the center of mass frame where  $|p_1| = |p_2| = P$ ,  $\vec{p}_1 = -\vec{p}_2$ ,  $E_{cm} = 2P$ . We

first integrate  $p_2$  to invorce 3-momentum conservation

$$\int \left( \frac{d^3 p_1}{(2\pi)^3 2E_1} \right) \left( \frac{d^3 p_2}{(2\pi)^3 2E_2} \right) (2\pi)^4 \delta^4(P - \sum p_f)$$

now switching to a spherical integral with a jacobian  $p_1^2 dp_1 d\Omega$  where  $d\Omega$  is and infinitesimal solid angle.

$$\int \frac{dp_1 p_1^2 d\Omega}{(2\pi)^3 (2\pi)^3 2E_1 2E_2} (2\pi) \delta(E_{cm} - E_1 - E_2)$$

here we use the same delta function identity to obtain:

$$\begin{aligned} \int d\Omega \frac{p_1^2}{(2\pi)^2 2E_1 2E_2} \left( \frac{p_1}{E_1} + \frac{p_2}{E_2} \right)^{-1} &= \int d\Omega \frac{p_1^2}{(2\pi)^2 2E_1 2E_2} \left( \frac{E_1 E_2}{p_1(E_1 + E_2)} \right) \\ &= \int d\Omega \frac{p_1}{16\pi^2 E_{cm}} \end{aligned}$$

Combining the result for the final state integral with Equation 3.2:

$$\left( \frac{d\sigma}{d\Omega} \right) = \frac{1}{2E_A 2E_B |\beta_A - \beta_B|} \frac{|p_1|}{(2\pi)^2 4E_{cm}} |\mathcal{M}|^2$$

Now if we assume the masses of the four particles are the same (or negligible at the energies involved) and substitute  $\beta = p/E$ :

$$\left( \frac{d\sigma}{d\Omega} \right)_{CM} = \frac{|\mathcal{M}|^2}{64\pi^2 E_{cm}^2}$$

### 3.1.2 Kinematics and Conventions

Pseudorapidity  $\eta$  As the detector has cylindrical symmetry, the coordinate system used most commonly is two dimensional  $(\eta, \phi)$ . The pseudo-rapidity,  $\eta$  is an approx-

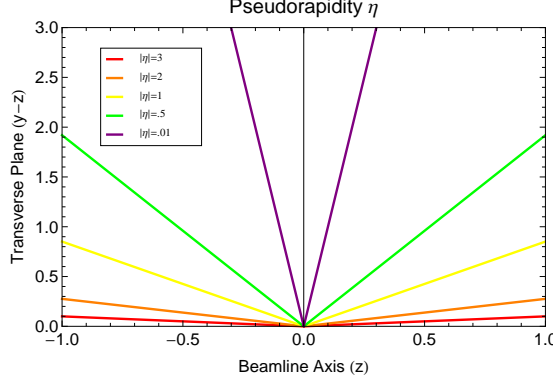


Figure 3.1: Lines of constant pseudorapidity in the z-y plane

imation to rapidity,  $y$ , that is exact in the  $\beta = 1$  limit:

$$y = \frac{1}{2} \log \frac{E - p_z}{E + p_z} \quad \eta = -\log \left( \tan \left( \frac{\theta}{2} \right) \right)$$

where  $\theta$  is the angle from the positive beam axis. This variable is useful for a number of reasons. Firstly, differences in rapidity are invariant under longitudinal Lorentz boosts along the beam axis. Also, for the energies being probed the particles in the decay products are of negligible mass and the approximation  $\eta \approx y$  is nearly exact. Given this relation, pseudorapidity provides an intuitive geometric interpretation. Near full solid angle coverage is provided within  $|\eta| < 5$

**$\boxed{\Delta R}$**  Given our coordinate system,  $\Delta R$  is our longitudinally boost invariant notion of distance:

$$\Delta R = \sqrt{(\Delta\phi)^2 + (\Delta\eta)^2}$$

Fixed values of  $\Delta R$  form a solid angle “cone” extending from the interaction point outward. This can be seen by using our definition of  $\eta$  to convert from cylindrical

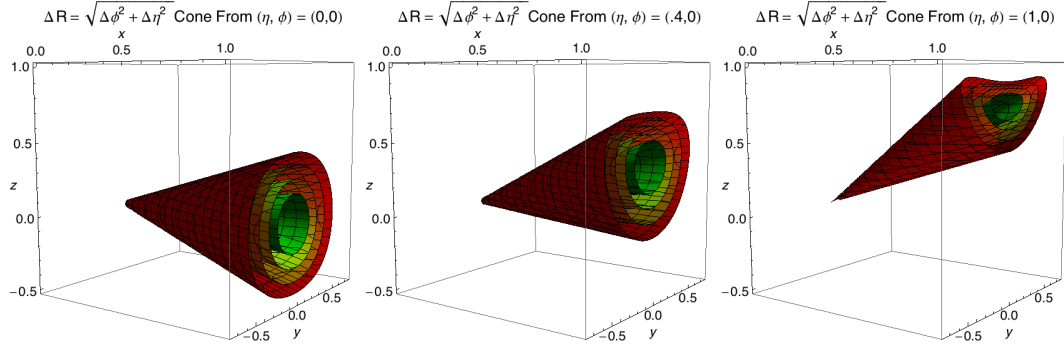


Figure 3.2: Contours of constant  $\Delta R$  from the  $(\eta_0, \phi_0) = 0, 0$

coordinates to  $(x, y, z)$  and consider the distance relative to the point  $(\eta_0, \phi_0)$

$$\Delta R = \sqrt{(\phi_0 - \tan^{-1}(y/x))^2 + \left( \eta_0 + \log \left( \tan \frac{\cos^{-1}(z/\sqrt{x^2 + y^2})}{2} \right) \right)^2}$$

## 3.2 Cross-sections

## 3.3 Luminosity

$$L = \frac{f}{\pi} \frac{N_p N_{p^*}}{n_b} \frac{\gamma}{\sqrt{\beta_x^* \beta_y^* E_x^* E_y^*}} \quad (3.3)$$

- $f$ : revolution frequency of the beams.
- $N_p$  the number of protons in the eam
- $n_b$  the number of proton bunches
- $\beta_{x,y}^*$  the transverse wavelengths of the beatatron oscillations
- $E_{x,y}^*$  the transverse emittance of the beams
- $\gamma$ : relativistic factor

To increase luminosity, this parameterization tells us we want a high frequency of collisions, high proton density within the bunches, small oscillations transverse to the ideal path, and a small average spread in position momentum space. The small spread in phase space (low emittance) means the particles are confined to a small area and have roughly the same momentum. This result in a high probability of interaction.

### 3.4 Parton Model of Hadron Collisions

cite:qcd-collider-physics-ellis

For a collision of two protons like that of the LHC (or proton anti-proton for Tevatron) the hard scattering process is not between the individual hadrons, but hadron's inner structure: the quarks and gluons. Unlike, a lepton collider, where the full four vector is controlled by the collider, the energy of any given hard hadron-hadron scattering process is probabilistic in nature, as the individual partons have some unknown fraction of the proton energy.

The cross section for a process for two hadrons with four-momentum  $P_1$  and  $P_2$  can be written:

$$\sigma(P_1, P_2) = \sum_{i,j} \int dx_1 dx_2 f_i(x_1, \mu) f_j(x_2, \mu) \hat{\sigma}_{ij}(p_1, p_2, \alpha_S(\mu), Q) \quad (3.4)$$

where the momentum of the partons participating in the hard interaction are  $p_i = x_i P_i$   $i = 1, 2$ . The scale of the hard scattering is denoted by  $Q$ . This would be  $m_W$  for  $W$  boson production. The  $f_i$  are the quark or gluon distributions within the protons. These are the parton distribution function (PDFs). The short distance cross section  $\hat{\sigma}$  can be calculated as a perturbative series in the asymptotically small running QCD coupling  $\alpha_S$ . The factorization scale  $\mu$  is an arbitrary parameter that is chosen as the boundary between the long and short distance interaction physics. The boundary at

$\mu$  separates the soft emitted partons that should be considered part of the hadron and the partons emitted at large transverse momentum that should be considered part of the hard process. In general, this be set near the order of the process process scaled  $Q$ .

If we consider the ratio of the actual  $\sqrt{\hat{s}}$  of the hard process relative to the proton  $\sqrt{s}$  we define  $\tau$ , the loss of energy between the COM collision of the proton and the individual partons

$$\frac{s}{\hat{s}} = \frac{(p_1 + p_2)^2}{(x_1 p_1 + x_2 p_2)^2} = \frac{2 p_1 \cdot p_2}{2 x_1 x_2 p_1 \cdot p_2} = \frac{1}{x_1 x_2} = \frac{1}{\tau}$$

Now lets consider the total cross section  $\sigma_{TOT}$  which consists of the parton luminosity  $L_{ij}$  for two individual partons  $i$  and  $j$  and the corresponding cross sections  $\sigma_{ij}$ . We assume that the cross section  $\hat{\sigma}$  is only a function of  $\hat{s}$ , (a property that holds true for many processes, but not in general). Let  $\tau_0$  be the minimum  $\tau$  at which the process can occur.

$$\begin{aligned} \sigma_{TOT} &= \sum_{i,j} \sigma_{ij} L_{ij} = \sum_{i,j} \int_{\tau_0}^1 \frac{dL_{ij}}{d\tau}(1) \hat{\sigma}_{ij} d\tau \\ &= \sum_{i,h} \int_{\tau_0}^1 \frac{dL_{ij}}{d\tau} d\tau \left( \frac{\hat{s}}{s\tau} \right) \hat{\sigma}_{ij} = \sum_{i,j} \int_{\tau_0}^1 \frac{d\tau}{\tau} \left( \frac{1}{s} \frac{dL_{ij}}{d\tau} \right) (\hat{s} \hat{\sigma}_{ij}) \end{aligned}$$

Here the center term is refered to as the parton luminosity function and contains the parton distribution functions with some extra accounting for the parton types to avoid double counting:

$$\tau \frac{dL_{ij}}{d\tau} = \frac{1}{1 + \delta_{ij}} \int_0^1 dx_1 dx_2 \times [(x_1 f_i(x_1, \mu^2) x_2 f_j(x_2, \mu^2)) + (1 \leftrightarrow 2)] \delta(\tau - x_1 x_2)$$

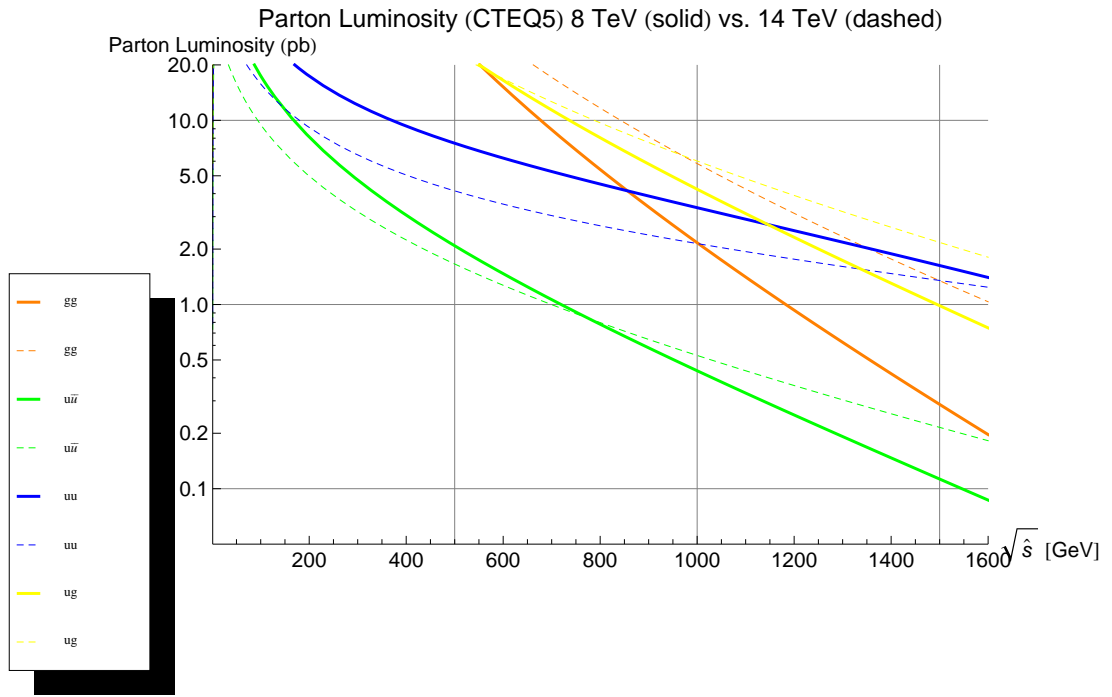


Figure 3.3: Contours of the parton luminosity function derived from CTEQ5 parton distribution functions for  $\sqrt{s} = 8$  TeV and  $\sqrt{s} = 14$  TeV. Contours are separated by collisions the individual partons in the collision.

## 3.5 The Narrow Width Approximation

## 3.6 Event Simulation

### 3.6.1 Hard Process Modeling

### 3.6.2 Parton Showering

### 3.6.3 Hadronization

$$\Lambda_{QCD} \approx 0.1 - 0.3 \text{ GeV}$$

top quark width is larger than lambda qcd and thus decays before hadronization.  
This allows for the study of a bare quark.

# Chapter 4

## Experimental Apparatus

### 4.1 CERN Laboratories

#### 4.1.1 Funding Model

The CERN operating budget provided by the individual member states. The size of the contribution is determined:

“using the arithmetic average of three years of Net National Income values until year before last year and applying the corresponding annual average exchange rate for each year”

Here the Net National Income is defined as:

Figure 4.1: Net National Income for member countries over the three year period used in the average generating the 2015 budget for CERN Laboratories

Table 4.1: Country Contributions 2015 cite:cern-budget. The total budget for CERN in 2015 was 1127 Million Swiss Francs cite:total-budget. The USD/CHF exchange rate as of 01-01-2015 was 0.994 and 0.999 as of 12-31-2015 cite:xchange-rates. Countries contributing less than 5% are excluded from the list (Switzerland contributes 3.87%). The average contribution from the top 5 countries which comprise 68.8 of the operating budget is 0.068 million swiss franc per billion dollars USD of gross domestic product. For the United States a comparable contribution (1224 Million USD) would be larger than the 2015 operating budget

Country	GDP	Abs (Rel) Cont.	(Cont/GDP) $\times 10^{-6}$
Germany	\$3.36T	231M CHF (20.5%)	68 CHF/USD
France	\$2.24T	170M CHF (15.1%)	75 CHF/USD
UK	\$2.86T	161M CHF (14.3%)	56 CHF/USD
Italy	\$1.82T	125M CHF (11.1%)	69 CHF/USD
Spain	\$1.19T	88M CHF (7.82%)	74 CHF/USD
USA	\$18.03T	-	-

Table 4.2: CMS Gender Demographics by Age as of 2014. Age groups are separated by age range. Columns represented the fraction of the total CMS. 4119 Males and 863 females for an overall gender ratio of 4.77 men to every 1 female.

Age Range	% of Men	% of Women	Male/Female Ratio
< 25	12.6%	19.4%	3.1
25-29	20.0%	24.0%	4.0
30-34	12.8%	15.0%	4.2
35-39	9.7 %	8.4%	5.0
40-44	8.5%	8.3 %	4.9
45-49	8.3%	7.2 %	5.5
50-54	8.5%	7.0%	5.8
55-59	6.6%	5.0%	6.3
60-64	5.2%	2.6%	9.8
65-69	3.8%	2.1%	8.7
>69	4.1%	0.6%	34

Table 4.3: Differences in Absolute NNI vs GDP for the year 2015. Ordering remains fixed by absolute contribution size.

Country	GDP [USD]	NNI [USD]	NNI/GDP	NNI/Capita
Germany	3.36T	3.31T	0.99	40.6k
France	2.24T	2.27T	1.01	34.4k
UK	2.86T	2.33T	0.81	35.8k
Italy	1.82T	1.84T	1.01	30.3k
Spain	1.19T	1.33T	1.12	28.6k
USA	18.03T	15.67	0.87	48.7k

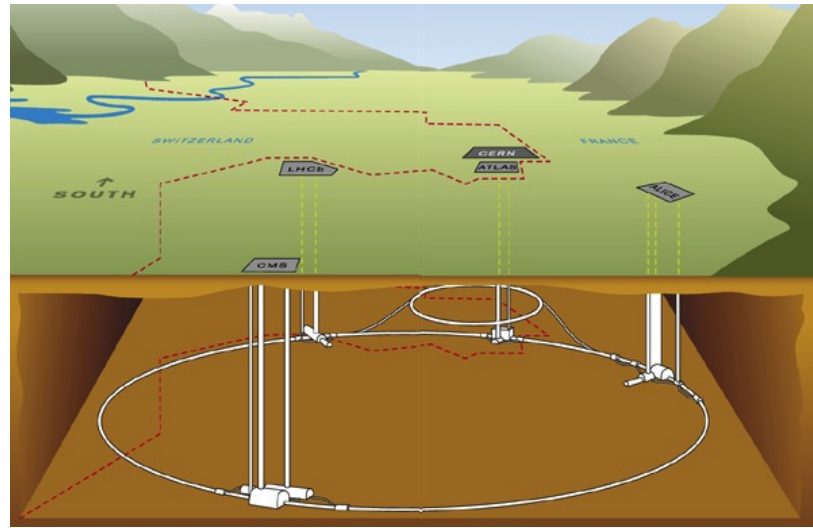


Figure 4.2: The LHC tunnel installed on the border of Geneva, Switzerland and France. The experiments are distributed along the circumference of the ring.

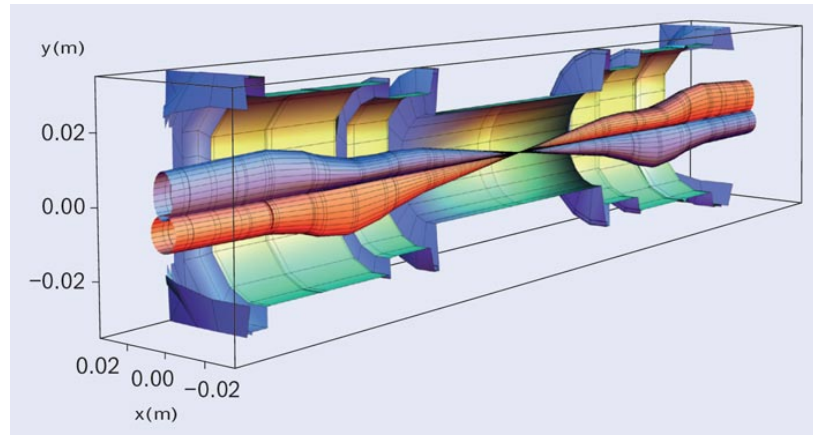


Figure 4.3: Squeeze

#### 4.1.2 Organizational Structure

### 4.2 The Large Hadron Collider

The bunches of protons in the LHC are bent into a circular trajectory by more than 1200 superconducting dipole magnets and are focused and maintained close to the ideal orbit around the ring by hundreds of superconducting quadrupole magnets.

Table 4.4: LHC Running Parameters cite:LHC\_PARAMETERS\_ONLINE.pdf

Parameter	Value	Remarks
Circumference (km)	26.7 km	100-150 m underground
Number of Dipoles	1232	Nb-Ti Cables
Length of Dipole	13.3 m	
Dipole Field Strength	8.4 T	Results from high beam energy
Operating Temperature	1.9 K	He cooled superconducting magnets
Current in Dipole Coils	13kA	Results from high magnetic field
Beam Intensity	0.5 A	
Beam Stored Energy	362 MJ	1MJ melts 2kg Cu
Magnet Stored Energy / octant	1100 MJ	

Thousands of corrector magnets around the ring allow the beam to be steered closer to the ideal orbit, make the focusing independent of the particles' energy variations within a bunch, and cancel the effects of higher order multipoles in the fields induced by small field imperfections in the main magnets. The radiofrequency (RF) field in superconducting cavities is placed periodically around the ring and accelerates the protons from the injection energy of 450 GeV to the final operating energy, which is designed to be 7 TeV per beam. The RF field also causes the protons to be bunched, as only particles at or near a certain "equilibrium phase" on the RF wave will be accelerated stably. Special quadrupoles around each interaction region focus the bunches down to a small transverse size, to increase the likelihood of a proton-proton collision each time two bunches pass through each other.

### Source of Pile Up Interactions

pile up events per event cross is the total inelastic cross section times the luminosity divided by the bunch collision rate. This is respectively  $8.5 \times 10^{-26} \text{cm}^2 \times 10^{34} \text{cm}^{-2} \text{s}^{-1} / (32 \times 10^6 \text{s}^{-1}) \approx 27$  (cite:arXiv:1204.5689).

## 4.3 Other LHC Related Experiments

## 4.4 Compact Muon Solenoid Experiment (CMS)

Physics from a theoretical point of view can consider particles in terms of their kinematic phase space, however, one cannot make direct measurements of the hard scattering process. Instead, detectors are built to indirectly measure the energy and momenta of the final state particles. To do this, a layered system of sub detectors is used to perform particle identification. By relying on known interactions of standard model particles with detector materials strong probabilistic statements can be made about the flavor of particles in a given collision. By building a hermetic detector and integrating the various subdetectors in a given solid angle, one obtains a wholeistic view of the fundamental physics. This section will discuss each subdetector, the particles it is used to identify, and the underlying physics which allows the individual measurements to be made.

The Compact Muon Solenoid (CMS) Detector is a general-purpose detector consisting of an all silicon tracker, a precision electromagnetic calorimeter (ECAL), a hadron calorimeter (HCAL), a 4 T superconducting solenoid and muon chambers. The solenoid deflects charged particles whose paths are traced in the tracker, making it possible to reconstruct the particles' momentum. The two calorimeters reconstruct the energy of and identify photons, electrons and hadronic jets. As shown in Figure ?? the detector has cylindrical symmetry about the interaction point where the proton beams collide. By maintaining near full coverage of the interaction point it is

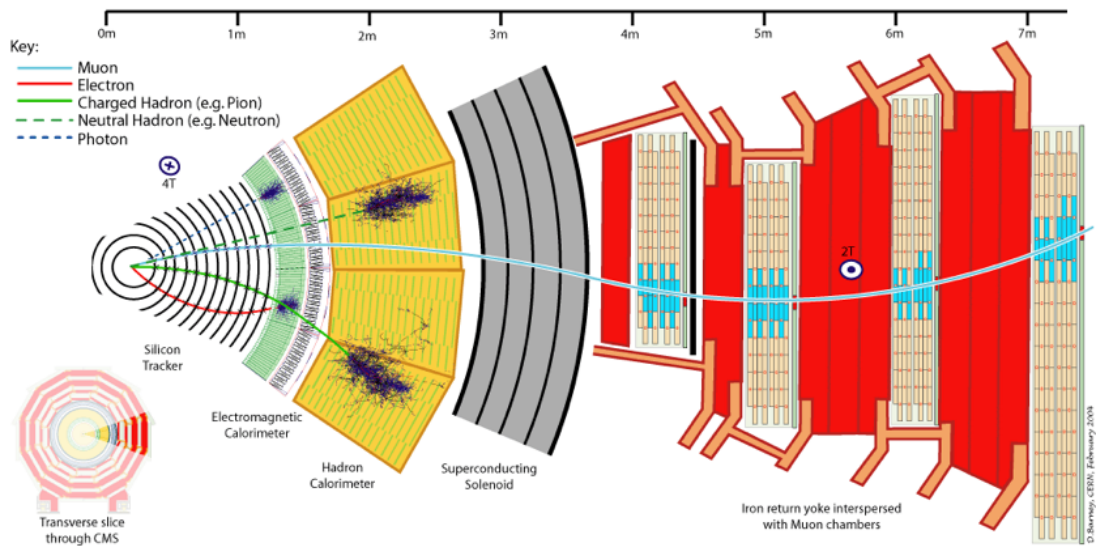


Figure 4.4: A tear-away view of the inner detectors of CMS.

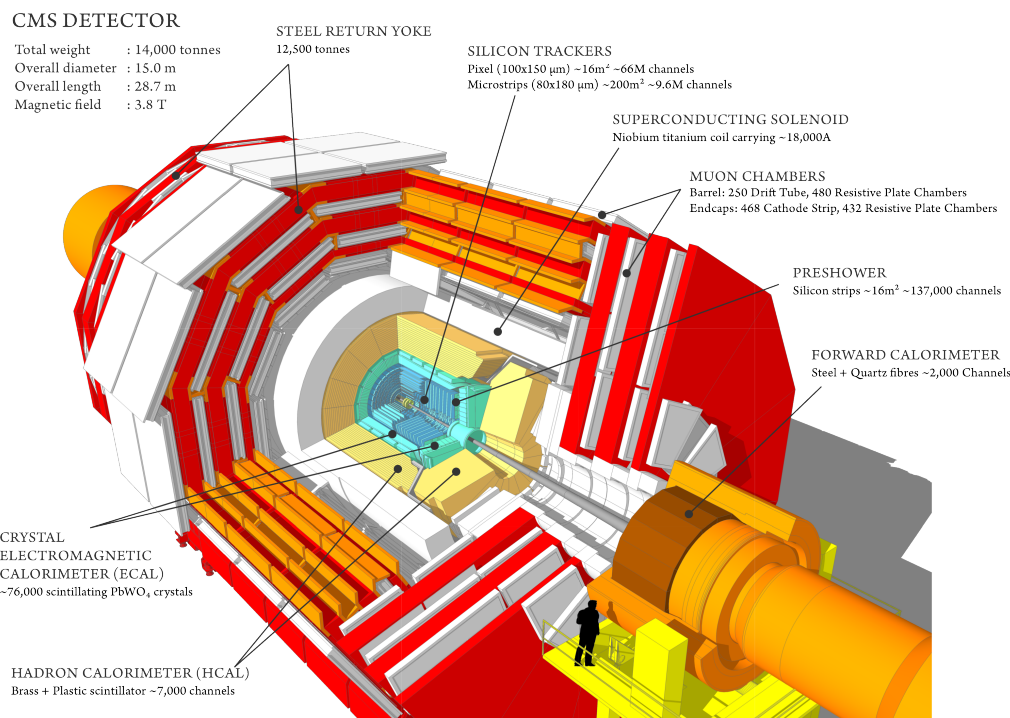


Figure 4.5: Cut away view of the CMS Detector

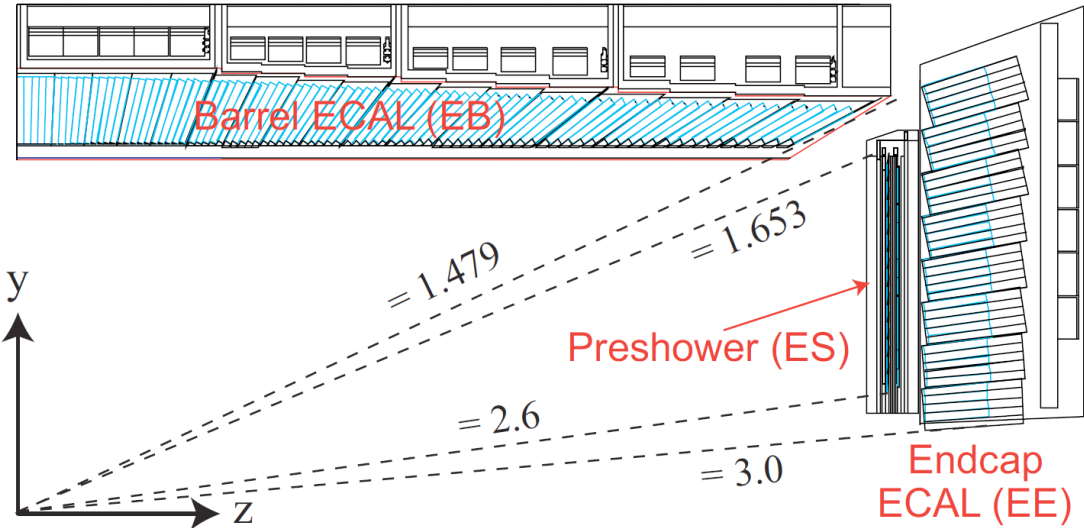


Figure 4.6: Kinematic coverage of the electromagnetic calorimeter (ECAL) barrel and endcap

possible to detect signatures such as neutrinos or other weakly interacting particles as missing energy.

#### 4.4.1 Electromagnetic Calorimeter (ECAL)

The electromagnetic calorimeter (ECAL) exists to measure the energy of electromagnetic showers of electrons and photons.

For high energy electromagnetic objects, that is above the mass threshold of pair production:  $\gamma \rightarrow e^+e^-$ , the interaction with matter occurs as an electromagnetic shower. In this shower, photons pair produce electron-positon pairs and electrons undergo bremmstrahlung radiation:  $e^\pm \rightarrow \gamma e^\pm$ . This processes continues until the individual particles in the shower cannot continue  $1 \rightarrow 2$  processes and instead undergo multiplicity preserving interactions such as compton scattering and ionization.

The detector material (for CMS a scintillating crystal) is characterised the shower's Moliere Radius, defined as the radius (transverse to the incidence) of a cylinder that contains 90% of the shower. For the CMS ECAL, crystals are of approximately the

Moliere radius 2.2 cm. The material can further be characterized by it's radiation length, the typical amount of matter the incident particle can traverse before an interaction. The CMS crystals have a relatively short radiation length of 0.9 cm. Each crystal is approximately 25 radiation lengths = 23 cm.

The crystal energy resolution as a function of energy is characterised as:

$$\frac{\sigma(E)}{E} = \frac{S}{\sqrt{E}} \oplus \frac{N}{E} \oplus C \quad (4.1)$$

Here  $\sigma$  is the gaussian standard deviation of the energy measurement, the operator  $\oplus$  signifies addition in quadrature,  $S$  the stochastic term,  $N$  the electronic readout noise, and  $C$  the constant term which does not scale with energy. The stochastic term  $S$  comes from the statistical nature of the photoelectric shower and the containment within the crystal. The readout term arises from the electronics noise in the preamplifier and digitization of the signal. The constant term  $C$  is caused by non uniformities between the many crystals and is ultimately dominated by the crystal to crystal intercalibration. As the first two term scale inversely with energy the constant term for high energy photons and electrons  $> 50$  GeV is dominant. The design energy resolution for high energy photons like those found in the discovery of the Higgs boson is  $< 0.5\%$

The ECAL consists of 75,848 Lead Tungstate PbWO<sub>4</sub> scintillating crystals Fig. ???. The ECAL is separated into two sections: the Endcaps and the Barrel. The Barrel consists of 61200 2x2x23 cm<sup>3</sup> crystals separated into 36 Supermodules and is contained in  $|\eta| < 1.48$ . The Endcaps are separated into 4 Dees (Fig. 4.8) of 3662 crystals with each crystal measuring 3x3x22 cm. The 4 dees cover a pseudorapidity range between  $1.48 < |\eta| < 3.0$ . The Endcaps are behind a preshower detector, composed of two lead absorbers interleaved with silicon detectors. The preshower covers the pseudorapidity range of  $1.653 < |\eta| < 2.6$  with each silicon sensor covering

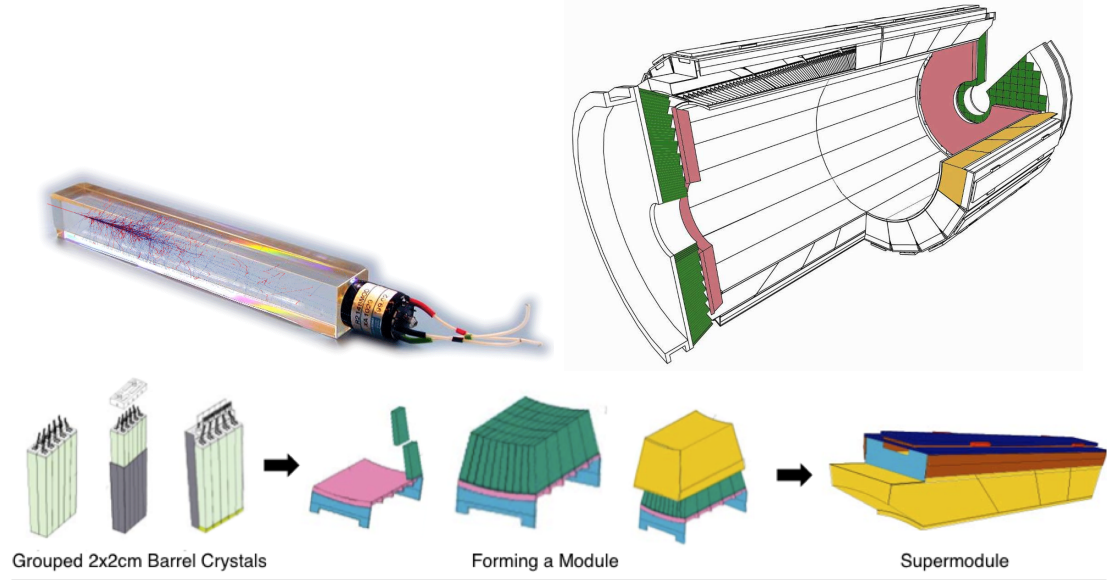


Figure 4.7: A single CMS ECAL Crystal (top left) tearaway view of distribution of crystals (top right) The construction of a single supermodule (bottom)

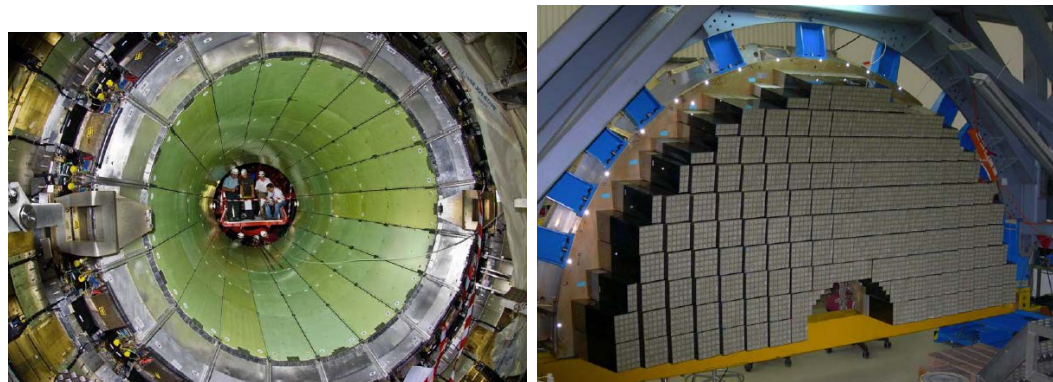


Figure 4.8: The ECAL barrel installed within CMS (left) A single Dee of the ECAL endcap (right)

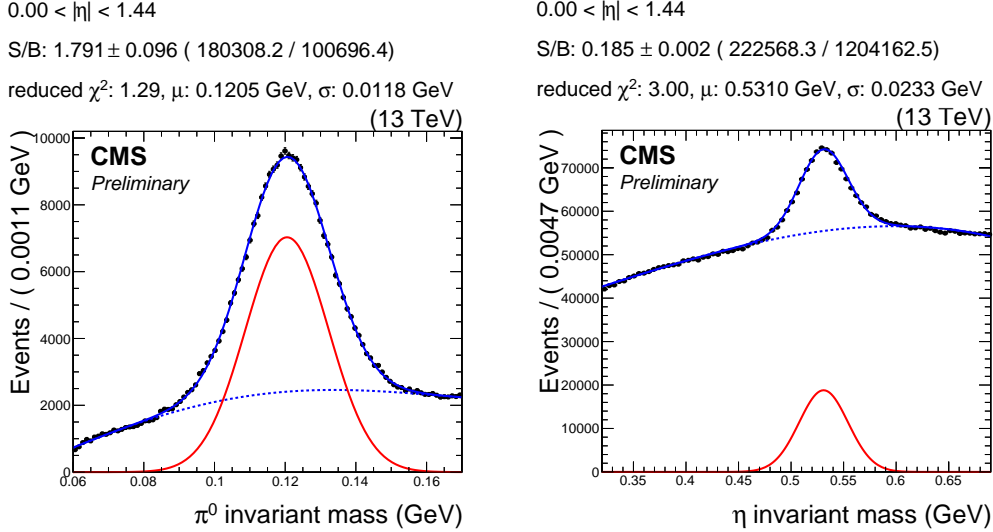


Figure 4.9: Calibration stream outputs for the pizero and eta barrel trigger paths

a square are of 63 mm x 63 mm divided into 32 strips. The preshower is designed to give significantly better spatial resolution than using the endcap alone to aid in the separating single photons and  $\pi^0 \rightarrow \gamma\gamma$  decays used to calibrate the endcap. As the first layer is 2 radiation wavelengths thick such that the majority of incident single photons will begin to shower before reaching the second layer.

The preshower converts many of the photons, which assists in distinguishing directly produced photons from pairs of photons resulting from neutral pion decays.

The light in each crystal is collected as a current and amplified by avalanche photodiodes (APDs) in the barrel region and vacuum phototriodes (VPTs) in the endcap. This transition is necessary as the endcap region must be tolerant to much higher levels of radiation damage from softly scattered (low momentum transfer  $Q^2$ ) interactions.

The detector is calibrated with a method that reconstructs the mass of neutral pion and eta-mesons to precisely calibrate the entire ECAL. The copious production of these particles in hadronic jets at the LHC allows us to perform this calibration rapidly, even at very low luminosity.

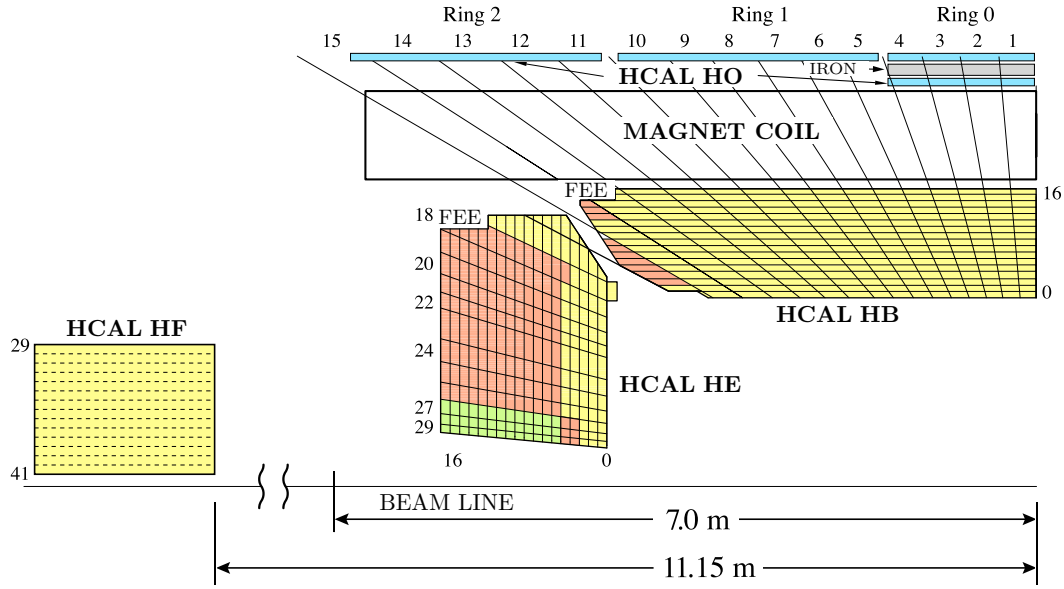


Figure 4.10: Kinematic acceptance of the CMS HCAL

Under irradiation, the crystals undergo transpacency changes due to the formation of color centers, which interestingly recover spontaneously when there is no radiation present. As the crystal transparency affects the energy measurement, the crystal transparency is continuously monitored by a laser monitoring system. The system takes advantage of a  $3 \mu\text{s}$  gap in the LHC bunch train to inject the pulses at a rate of 100 Hz. This rate allows for a measurement of every crystal to be made at least every 30 minutes. In the barrel, only laser pulses of known wavelength are injected through optical fibers. In the endcap, LEDs provide an additional wavelength.

The presence of the preshower also causes some degradation of the Endcaps' energy resolution relative to the Barrel.

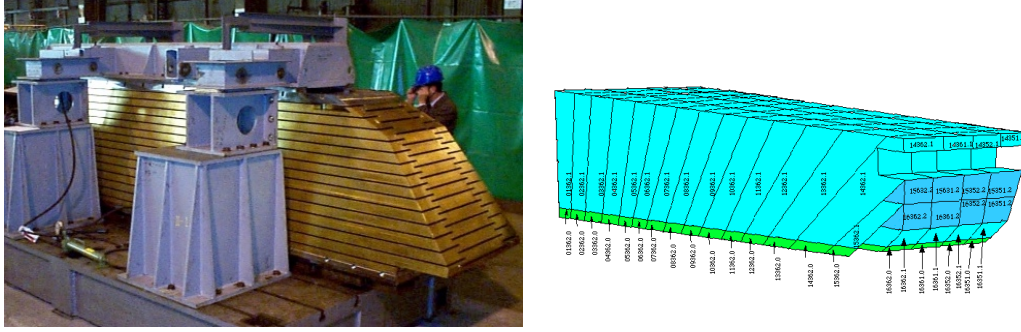


Figure 4.11: A single wedge of the CMS HCAL barrel

#### 4.4.2 Hadronic Calorimeter (HCAL)

Surrounding the ECAL. The Hadronic Calorimeter (HCAL) is designed to measure the energy of neutral hadrons which do not deposit the majority of their energy in the ECAL.

The HCAL consists of four sections: the barrel (HB), the endcap (HE), two forward calorimeters (HF) and an outer hadron calorimeter (HO). The barrel and endcap of the HCAL cover  $|\eta| < 4$ . The forward detectors extend the subdetector's reach to  $|\eta| = 5$ . The Outer Calorimeter exists to contain extremely high energy jets from reaching the muon chambers. While electrons and photons deposit nearly all of their energy in the ECAL, high energy hadrons deposit most of their energy in the HCAL.

The detector is constructed as alternating layers of brass absorber and plastic scintillator

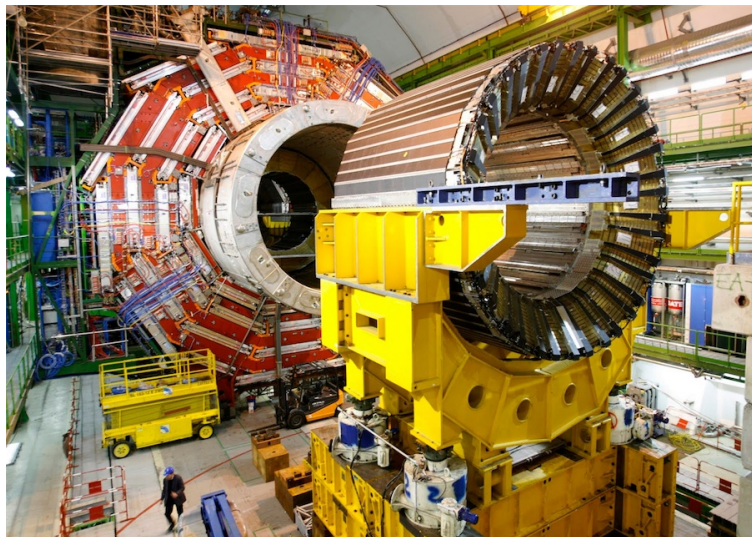


Figure 4.12: The CMS HCAL outside of the detector

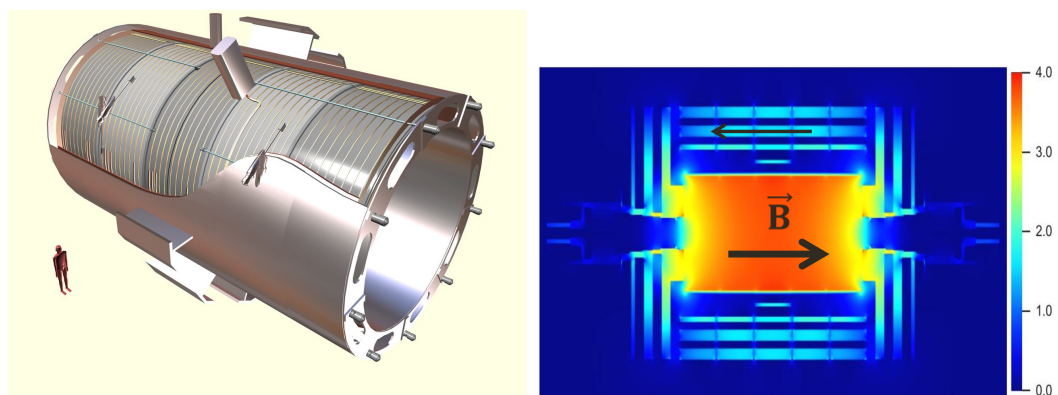


Figure 4.13: The CMS solenoid with a human for scale

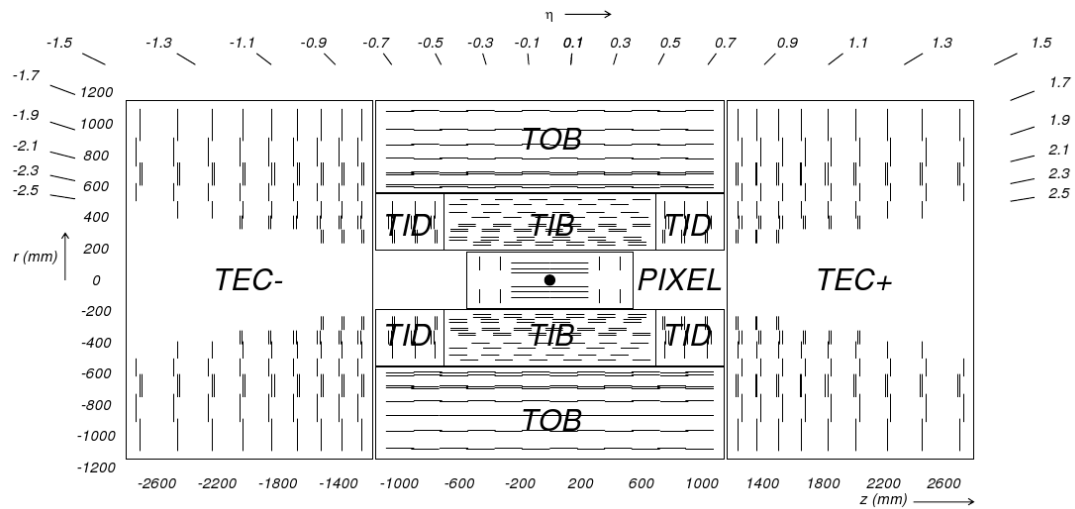


Figure 4.14: Kinematic acceptance of the CMS tracker

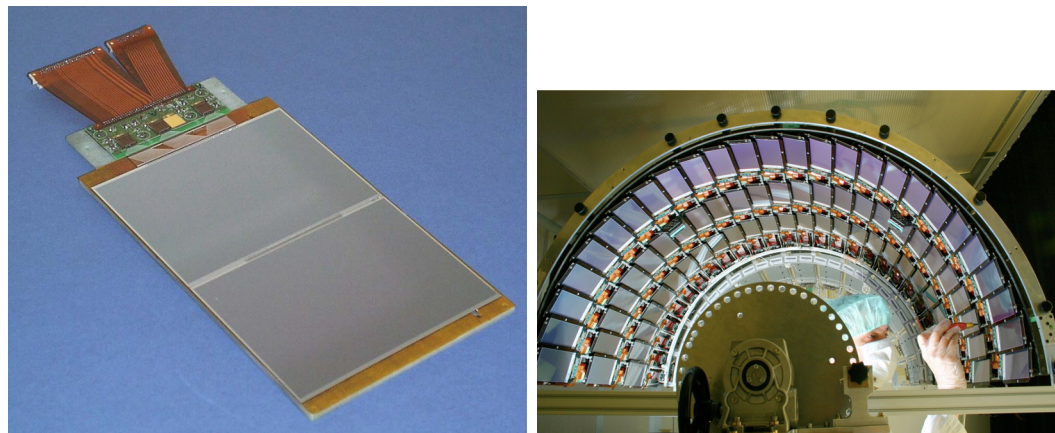


Figure 4.15: A single CMS tracker module (left) and a tracker inner barrel module (right)

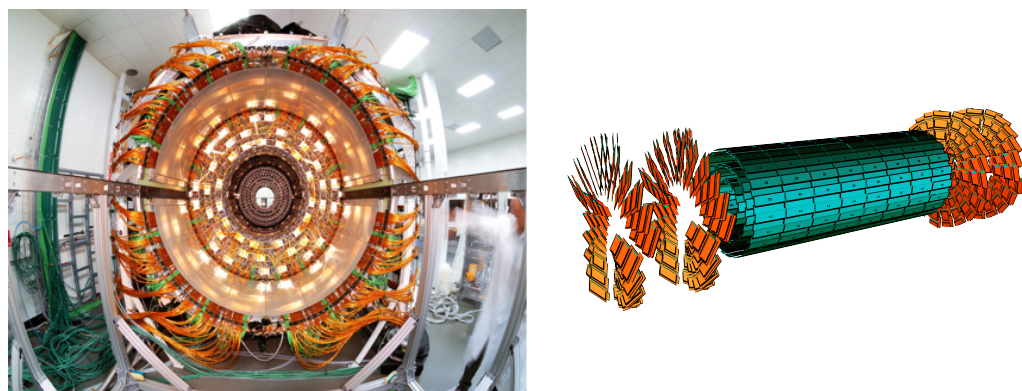


Figure 4.16: The CMS Pixel detector

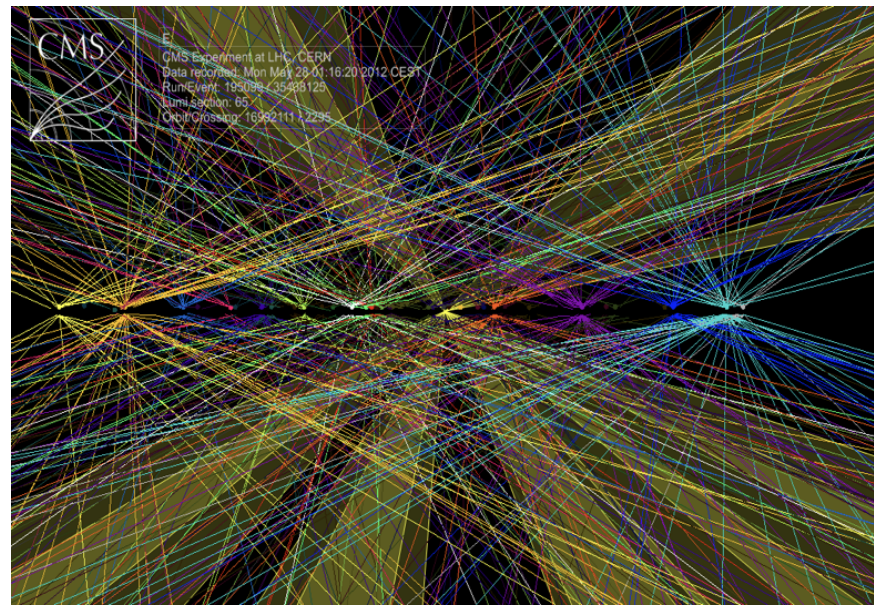


Figure 4.17: Pileup Interactions

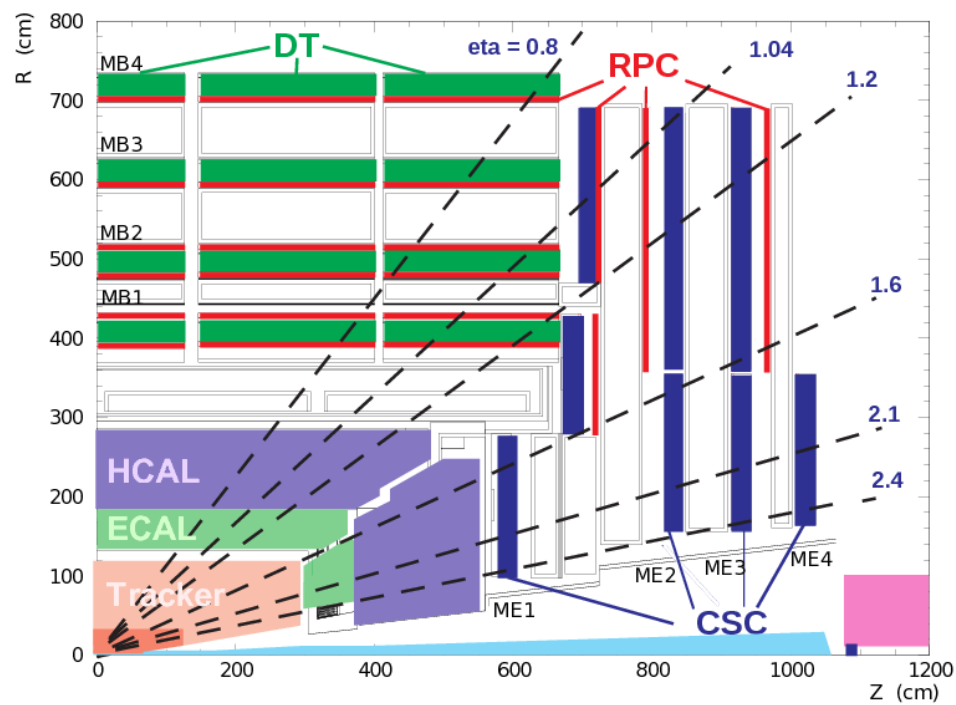


Figure 4.18: Kinematic acceptance of the CMS Muon System

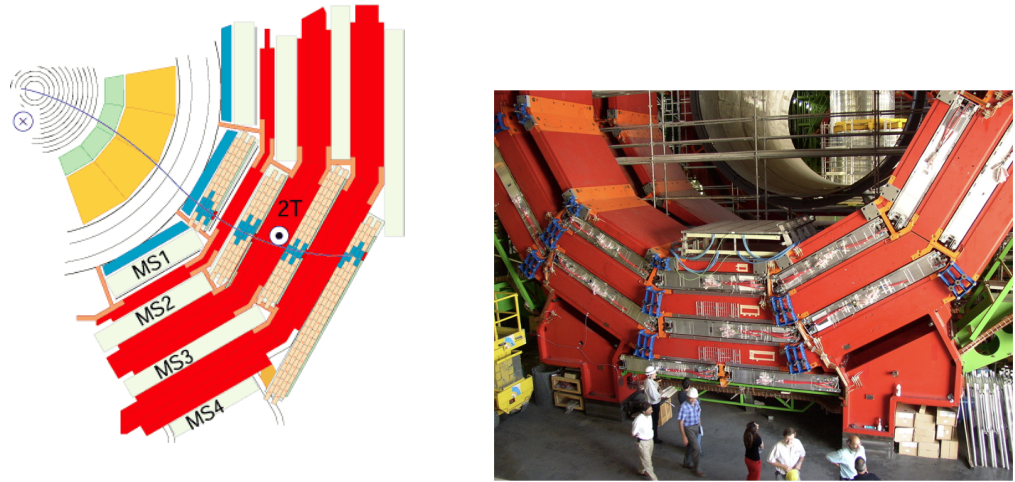


Figure 4.19: The Muon RPC Plates

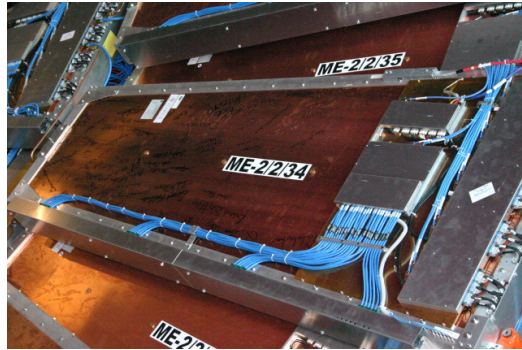


Figure 4.20: The Muon Cathode Strip Chamber

#### **4.4.3 Superconducting Solenoid**

#### **4.4.4 Tracking**

#### **4.4.5 Muon Chambers**

#### **4.4.6 Trigger System**

The CMS Trigger System exists as a filter through which events are determined to be “interesting”. It is both unnecessary and inefficient to record anything that occurs in the detector electronics. Most events that occur from colliding protons are well

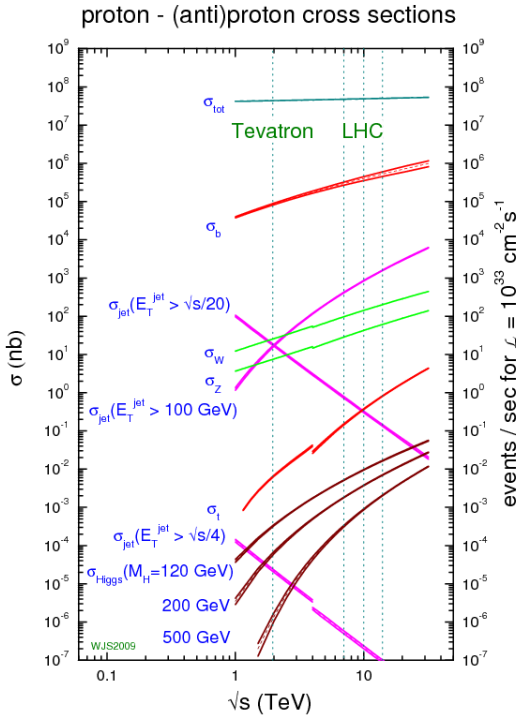


Figure 4.21: Common cross sections of proton collisions as a function of the center of mass energy  $\sqrt{s}$

understood. To the left, you can see the logarithmic plot of common physics processes for proton-proton scattering. Events such as the production of a  $b$  quark occur at  $\approx 10^6$  Hz at a luminosity of  $\mathcal{L} = 10^{33} \text{ cm}^{-2}$  whereas the production of the Higgs is much lower at  $\approx 10^{-2}$  Hz.

At design luminosity, the LHC has beam crossings at a rate of  $\approx 40$  MHz with each crossing coming spaced at  $\approx 25$  ns. For each crossing there are  $\approx 20$  inelastic collisions (referred to as pile up) contained in an event file of  $\approx 1$  Mb. However the bandwidth for storage is limited to  $\approx 10^2$  Hz and equivalently  $10^2$  Mb/s. Generally, all but one of the inelastic collisions is interesting and a large excess of uninteresting activity is generated in the detector electronics. The trigger must be robust enough to select this needle in a haystack event while remaining computationally efficient in maximizing the limited bandwidth.

The CMS Trigger system is designed to read events at the event crossing frequency and generate the factor  $10^5$  of rejection between the crossing frequency and the archival capacity. This factor is far too large to achieve in a single step given the complexity of triggers and event reconstruction. Therefore the task is split into two steps: The Level 1 (L1) and High Level (HLT) Trigger systems.

The  $O(10^7)$  events per second first pass through the L1 Trigger which reads out events at  $10^5$  Hz. From here, the High Level Trigger makes the final decision as to which events are kept. Approximately 350 Hz is processed and stored, 300 Hz is “parked” (stored but processed later), and 1 kHz is partially stored (only the HLT level information and not the RAW detector information) and used for data scouting for future analysis.

The most basic criterion for interesting events are hard physics events with high momentum transfer,  $q^2$ . As the protons collide with effectively no transverse momentum, any event with significant deposits of transverse energy (or even missing transverse momentum) is indicative of a hard physics process. The number of objects with a given transverse momentum falls off exponentially, so a simple minded way to reduce the rate of processed events is to raise the threshold of accepted events.

More specific criterion for “interesting events” is analysis dependent. Generally, analyses are categorized by their final state signature. Thus, the trigger requires loose identification on the objects of that signature such as the isolation and shape of energy deposition. Once the event has passed the Level 1 and HLT Triggers, tighter and more computationally costly selection can be made offline where we are unrestricted by bandwidth limitations.

As there is a limited amount of bandwidth for processing the events, the numerous analyses of CMS are given a budget (measured in Hz) for the triggers they request. As it stands the  $H \rightarrow \gamma\gamma$  analysis is assigned a budget of 30 Hz for its diphoton trigger

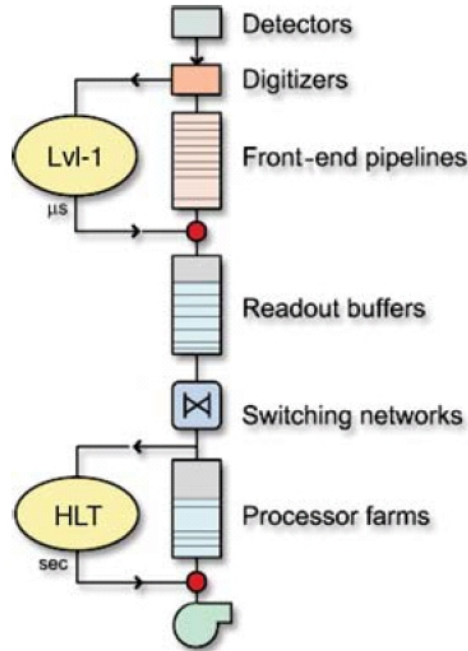


Figure 4.22: A diagrammatic representation of the level 1 and HLT trigger processing

suite. As the diphoton channel was of high priority in the 7 and 8 TeV running this accounted for a significant fraction ( $\approx 10\%$ ) of the overall budget.

As the luminosity of the machine increases, we expect proportionally more events per second and must accordingly alter the triggers.

### Level 1 (L1) Trigger

### High Level Trigger (HLT)

# Chapter 5

## Studies of Displaced Jet Tagging Variables

### 5.1 Introduction

The identification of jets originating from  $b$  quarks ( $b$ -tagging) was originally developed and successfully utilized for the discovery of the top quark. Among other applications,  $b$ -tagging is now a tool for studying the Higgs and searching for beyond the standard model (BSM) physics. Since its inception,  $b$ -tagging has evolved including the implementation of particle flow, refined secondary vertex algorithms, and advanced multivariate techniques. The strength of  $b$ -tagging is not restricted to its signal to background differentiation, but includes the community sized impact of a well defined and supported physics object definition.

The  $b$ -tagging algorithms are publicly documented with corresponding working points and data/mc factors derived by the physics object group (POG in CMS). The algorithms are integrated directly into the experiment software allowing fast adoption of subsequent improvements. The object can then be used interchangeably as part of a large toolkit of jets, leptons, taus, photons, and missing energy.

Past searches (list references here) by CMS and ATLAS experiment for long lived particles decaying to jets rely significantly on secondary vertexing of displaced tracks. As the ability to vertex the jet is highly dependent on the ability to reconstruct highly displaced tracks, the existence of a vertex, although the highly separating between signal and background is often the most inefficient selection criteria (especially at long life times on the scale of the detector). Of particular concern is that current vertexing algorithms may not perform effectively for non-SM jet vertices such as found in Emerging Jets [citation].

The case of long lived particle that decay outside of the detector remains outside the scope of jet-tagging, but remains an interesting use case in conjunction with the tag definitions.

Analyses utilizing the tags should expect strong topological sensitivity for  $\geq 2$  displaced jets, electrons, and taus regardless of their configuration of a long lived  $X$  decay. Lifetime sensitivity is expected for decays which occur for transverse distances between 1mm to 2m, corresponding to outside of the lifetime of b hadrons up to the edge of the HCAL.

### 5.1.1 Significant differences with respect to b-tagging

Given the close analogy to  $b$ -tagging techniques, it is important to clarify where  $b$ -tagging algorithms are inefficient and where they can be extended.

For shorter lifetime regimes ( $c\tau < 1$  mm),  $b$ -tagging can still identify displaced jets, but leaves room for new techniques. Heavy long-lived resonances undergoing a 2 body decay will have significantly more momentum transverse to the flight direction of the long lived particle (when compared to a  $b$  decay). This angle is a powerful discriminant to background nuclear interactions and is strongly correlated with the boost of the mother particle. Under the assumption that the angle is small,  $b$ -tagging uses only positively signed impact parameters for track identification (corresponding

to to decays downstream of the flight path). Heavy particles produced nearly at rest will decay isotropically with impact parameters of negative sign (when decays occur backward relative to the mother's momentum direction).

For longer lifetimes, a transition occurs at distances larger than a few centimeters where new issues undaddressed by b-tagging arise. Although the  $b$  meson is displaced it is comparably straightforward to discern the primary vertex of the event. This allows b-tagging algorithms to more accurately calculate longitudinal quantities, such as 3D track impact parameters. For displaced jets, this is not the case and utilizing longitudinal quantities relative to a mis-identified primary vertex can yield sub-optimal performance. Pixel hit requirements are explicitly required for tracks used in  $b$ -tag secondary vertexing, but displaced jets decays can occur outside the pixel layers. In addition, b-tagging algorithms include upper bounds on longitudinal and transverse impact parameters to limit contributions from nuclear interactions.

o

## 5.2 Samples

## 5.3 Signal Samples

Two signal samples are used to study displaced identification which we will refer to as  $XX4J$  and  $GUN$ . Both samples are generated using PYTHIA 8 (cite-pythia).

The  $XX4J$  sample consists of the direct pair production of two neutral  $X^0$ 's with finite lifetime. Each  $X^0$  decays to u,d,s,c, and b with equal probability. This sample is generated with flat pileup between 10 and 50 with 25 ns bunch crossing code for cmsDriver as `Flat_10_50_25ns`. It is important to note that due to pile up interactions, these samples contain both prompt and displaced jets. In this sample,

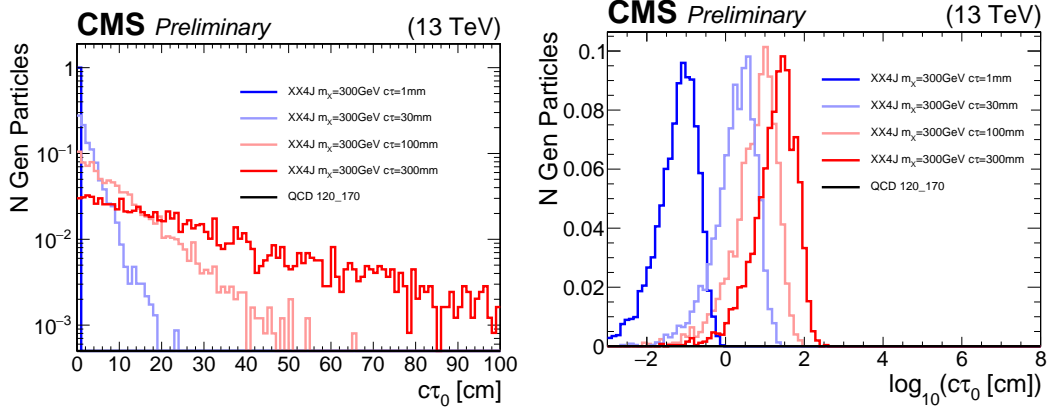


Figure 5.1: The proper  $c\tau_0$  of the XX4J samples. The samples are generated with exponential lifetime distributions  $e^{-x/c\tau_0}$  which have mean  $c\tau_0$  and exponential slope  $1/c\tau_0$ .

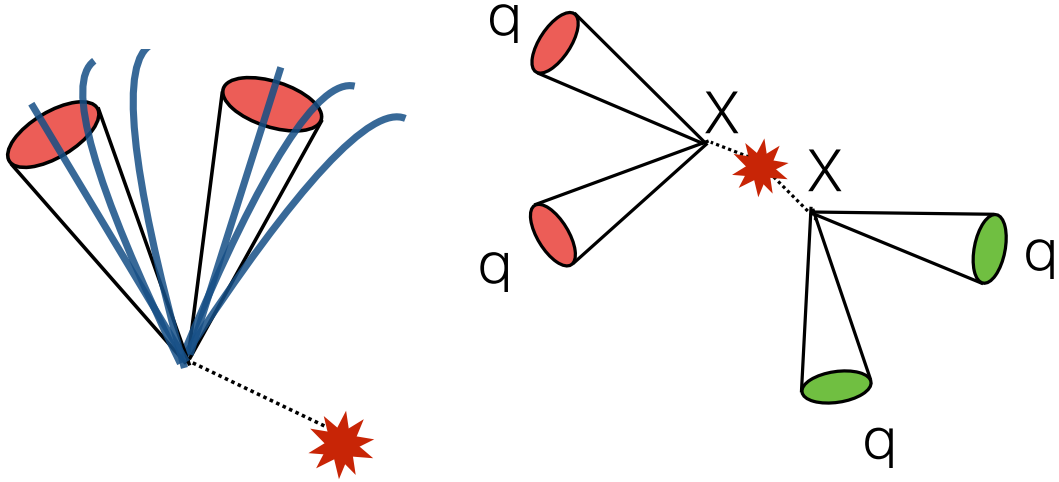


Figure 5.2: The topology of the two samples used in the study *GUN* (left) and *XX4J* (right)

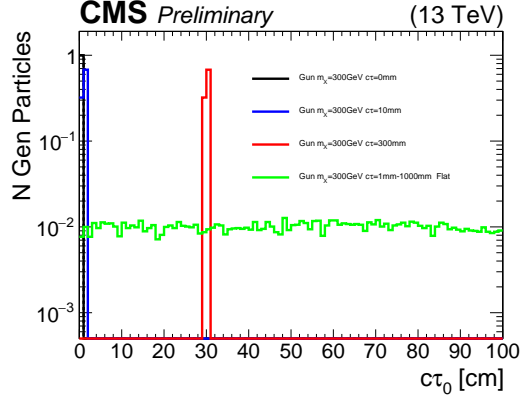


Figure 5.3: The proper  $c\tau_0$  of the displaced di-jet gun samples. The samples are generated with either flat, or delta function  $\delta(c\tau_0 - c\tau'_0)$  lifetime distributions

variables for displaced jet identification generally have two distinct populations of jets.

The  $XX4J$  samples are generated with varied lifetimes and masses (Fig. 5.1). Each  $X^0$  has an exponential lifetime distribution  $e^{-x/c\tau_0}$  with mean  $c\tau_0$  and slope  $1/c\tau_0$ .

The second sample is a displaced di-jet gun sample denoted  $GUN$ . This sample is generated using the `PythiaPtGun` interface. A single  $X^0$  particle is generated with flat  $50 < p_t < 500$  GeV, flat  $\phi$ , and flat  $-2.4 < \eta < 2.4$ . The  $X^0$  decays to a pair of d quarks with 100% branching fraction. Each event will thus contain a single displaced vertex. The configuration for the gun parameters is shown below. Small modifications to CMSSW are required to create a Pythia rather than HEPMC Particle with a finite lifetime.

The resonance is decayed within pythia and passed directly to hadronization bypassing all process level pythia effects: initial state radiation, final state radiation, and beam remnants. Furthermore, the event is reconstructed without pileup mixing. This sample is generated to have a sample of reconstructed tracks that only originate from a displaced vertex without the complications of correctly. One important side effect of simulating without pileup is the lack of a reconstructed primary vertex.

The proper lifetime distribution of the sample is chosen to be either a delta function  $\delta(c\tau_0 - c\tau'_0)$  or flat between 1mm and 1000mm (Fig. 5.3). Additionally two prompt dijet gun samples are built for comparison. One sample with lifetime 0mm decaying to two b-quarks and one sample with lifetime 0mm decaying to two d-quarks. A reminder that the decay length in the lab frame will differ by a factor  $\gamma\beta$  from the proper lifetime .

The reconstructed calo jet transverse momentum for varied lifetimes is not especially sensitive to the lifetime of the decaying  $X^0$  (Fig. ??) until very long lifetimes. The flat lifetime gun sample develops high transverse momentum (relative to the shorter lifetime) jets when the long lived  $X^0$  decays at a transverse distance far enough from the beamline to be reconstructed as a single jet, or decaying entirely inside the calorimeter.

## 5.4 Individual Variable Studies

### 5.4.1 Impact Parameter Information

The tracks originating from a decay at a displaced vertex will have large impact parameters relative to the true primary vertex. The impact parameter is calculated by starting from the particle trajectory at the innermost measurement point and extrapolating backward to the minimum distance between the track and jet direction  $\vec{j}$  (Fig 5.5). Here, the track is linearized by taking the line tangent to the track at this point. The minimum distance from this linearized track to the primary vertex gives the magnitude of the impact parameter. We will refer to the vector pointing from the primary vertex to the point of minimum distance as  $\vec{IP}$  (Fig. 5.4).

The sign of the impact parameter is given as the sign of the scalar product between  $\vec{IP}$  and the direction of the jet:  $\vec{IP} \cdot \vec{j}$ . For decays where the calo jet direction is accurately reconstructed, the impact parameter of displaced tracks will have positive

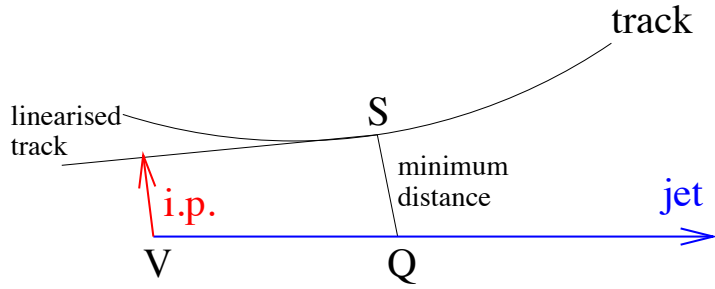


Figure 5.4: Diagram depicting the impact parameter calculation.  $V$  is the position of the primary vertex.  $\vec{j} = \vec{V}\vec{Q}$  is the direction of the calo jet.  $S$  is the point on the track extrapolation backward from the inner hit which is closest to the jet axis. From  $S$  the track is linearized and extrapolated backwards. The impact parameter magnitude is the minimal distance on the linearized track from the primary vertex. We will denote the vector from the primary vertex to the point of minimal distance on the linearized track as  $\vec{IP}$

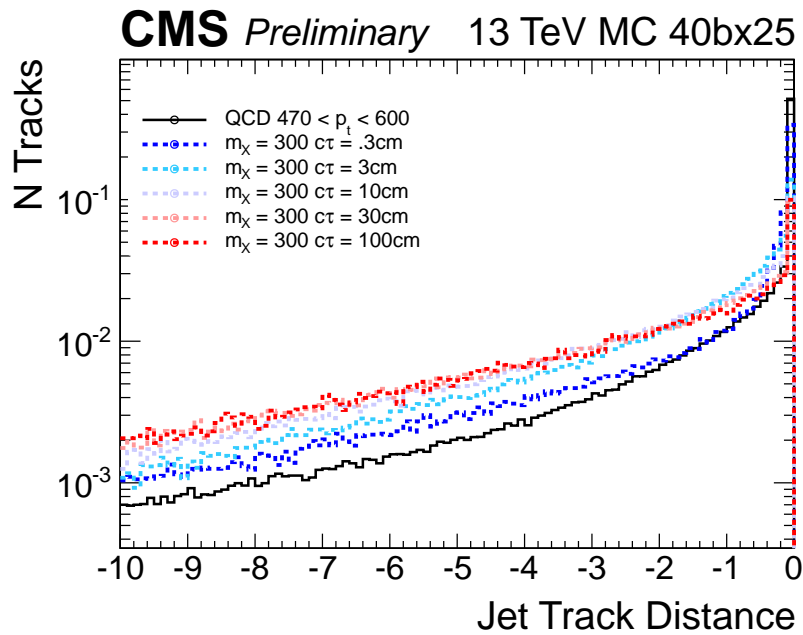


Figure 5.5: The closest distance between the jet axis and track

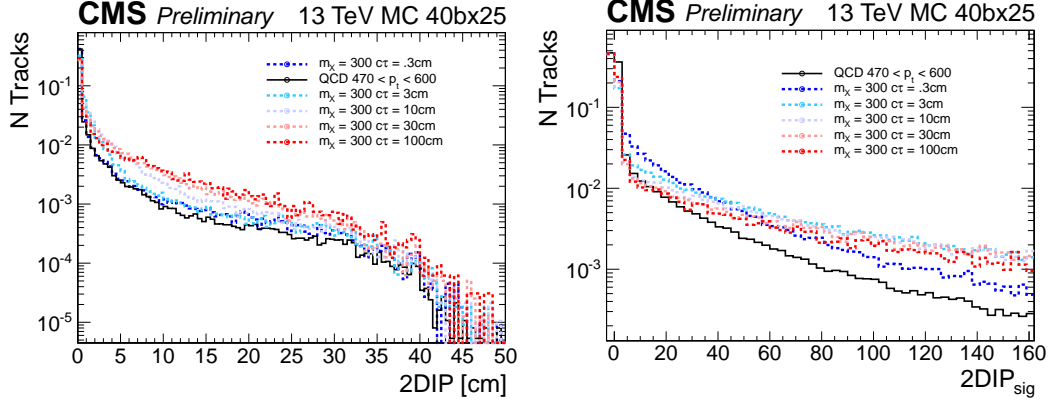


Figure 5.6: The same samples in Fig ?? are shown. (Left) The 2D impact parameter of tracks matched to calo jets matched to generator quarks with  $\Delta R < 0.5$ . (Right) 2D impact parameter significance of the same tracks. All distributions are normalized to 1.

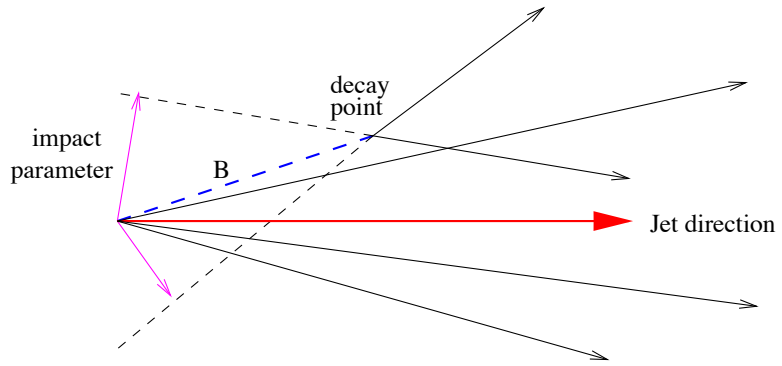


Figure 5.7: Diagram of a B hadron decay showing the mis-alignment of the jet direction from a calo jet and the decay vertex

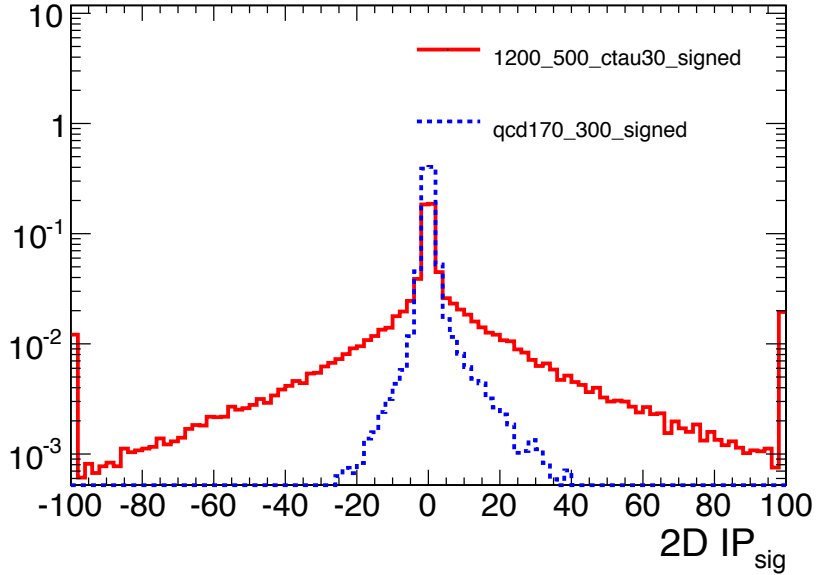


Figure 5.8: Comparison of the  $2DIP_{sig}$  of tracks within 1) QCD jets and 2) the less boosted decay of a heavy higgs  $H^0 = 1200\text{GeV}$  decaying to two long lived  $X^0$  with  $m_X = 500\text{GeV}$ . As not all tracks are down stream of long lived flight direction there are tracks with large negative values of  $2DIP_{sig}$ . The contribution of  $B$  mesons producing tracks with large positive  $2DIP_{sig}$  can be sign in the asymmetry of the QCD distribution

sign, corresponding to the decay occurring down stream of the jet direction. As the accuracy of the jet direction reconstruction depends on the lifetime of the particle producing the jets (Fig. 5.7), we opt to use un-signed IP significance to identify displaced jets (Fig. 5.6). In example, a case when the signal has large negative values of  $2DIP_{sig}$  is shown in Fig 5.8. It is important to note that as most *GUN* samples (excluding the prompt samples) do not have a reconstructed primary vertex, a fake primary vertex with a nominal error is introduced in the calculation. This biases the impact parameter significance relative to the  $XX4J$ .

To account for the tracking resolution impact parameter significance is introduced. Tracks with impact parameter consistent with the primary vertex relative to the tracking resolution given small impact parameter significance  $< 5$ . For decays

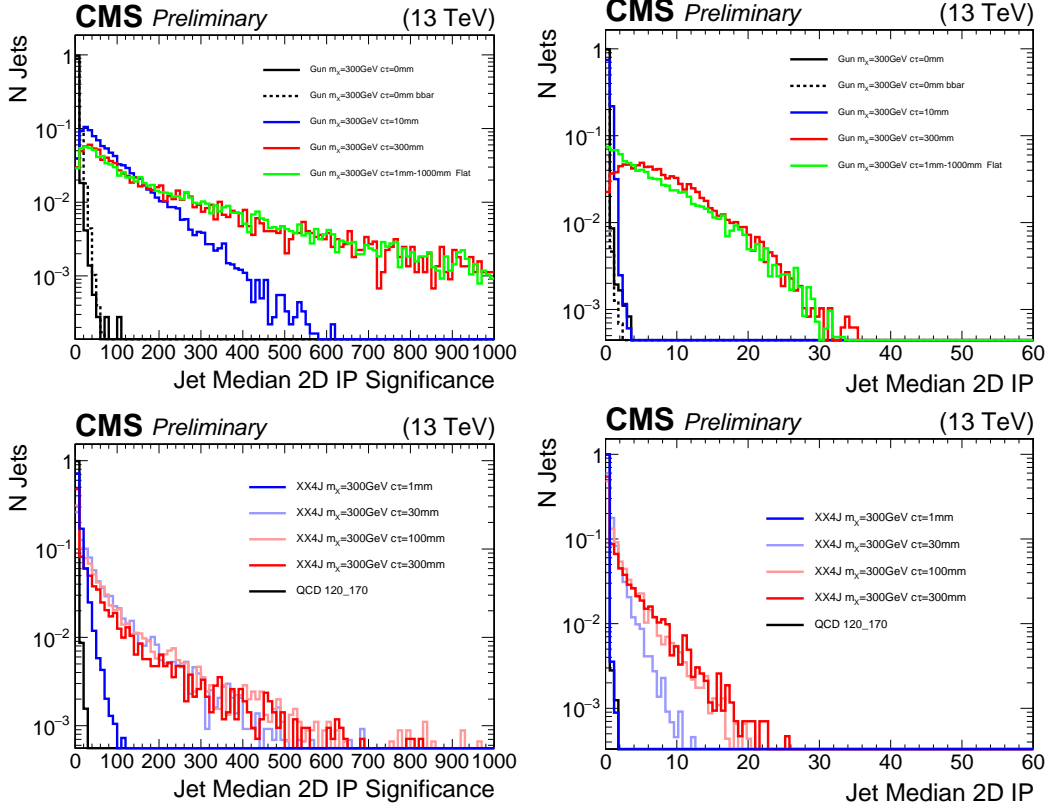


Figure 5.9: Unsigned 2D impact parameter for the  $XX4J$  and  $GUN$  samples

within  $L_{xy} < 10$  mm significance gives significant improvements in signal background separation relative to the absolute impact parameter value Fig. 5.9.

Impact parameter tag info is reconstructed with limited requirements on the tracks. No maximum longitudinal or transverse impact parameter is enforced. No requirement on the number of hits, pixel tracks, or track quality is required at this step. A maximum  $\chi^2 < 20$  of the track fit is enforced and a  $p_t > 1$  GeV to ensure the track would reach the calorimeter.

Variables leveraging the impact parameter information for a given jet are derived from the distribution of impact parameter significances. Fig. 5.10 demonstrates the improved separation of median IP significance relative to the mean (Fig. 5.10). As background QCD jets contain real displaced tracks (Tab. 2.3, 2.4), the mean

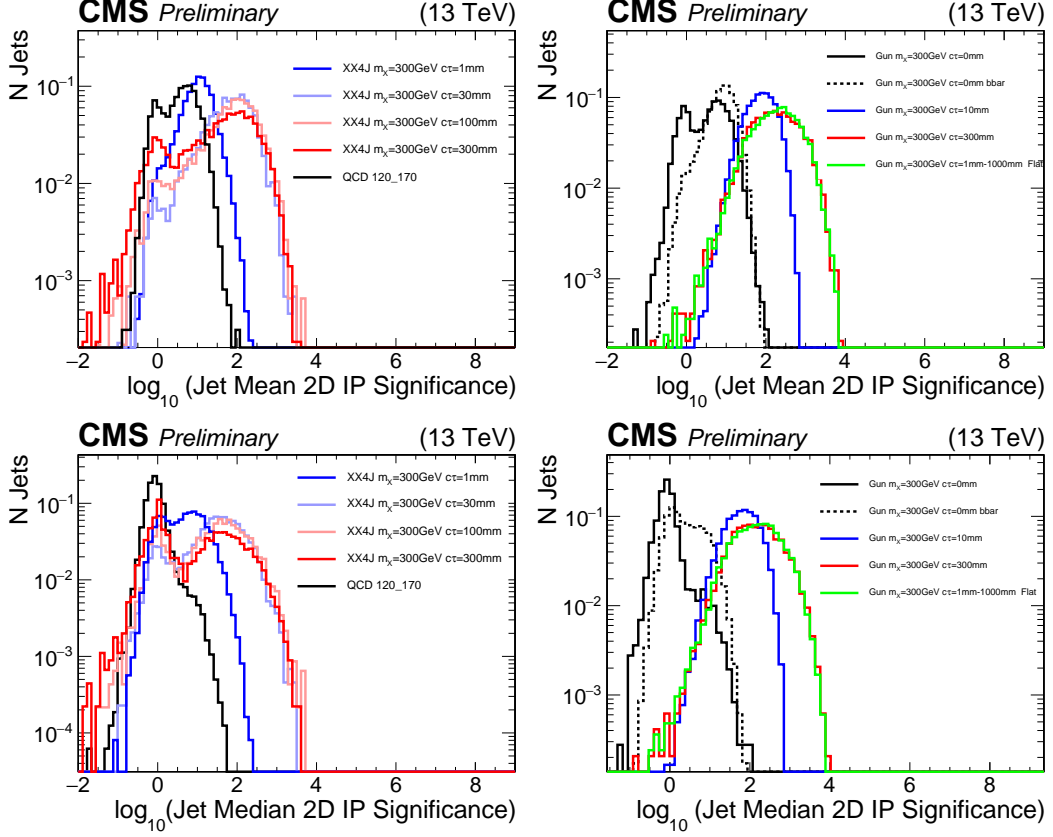


Figure 5.10: A comparison between using mean or median IP significance for the displaced di-jet gun and XX4J signal samples

calculation is sensitive to outlier tracks with large IP significance. For truly displaced jets, all tracks have large impact parameter preserving a high median value.

The tracks from displaced jets should not have significant contribution from tracks included in a primary vertex. This reduces the likelihood of selecting the correct primary vertex for the calculation of 3D impact parameters. Instead, we opt to use exclusively transverse quantities that depend only loosely on the primary vertex selection when a beam-spot constraint is applied. Fig. 5.11 shows the comparison between the 2D and 3D impact parameters showing greater separation for using traverse impact parameters. For the displaced di-jet gun samples, a primary vertex is rarely reconstructed for longer lifetimes. In this case, a fake PV is built and the resulting discrimination power is lost in the longitudinal axis.

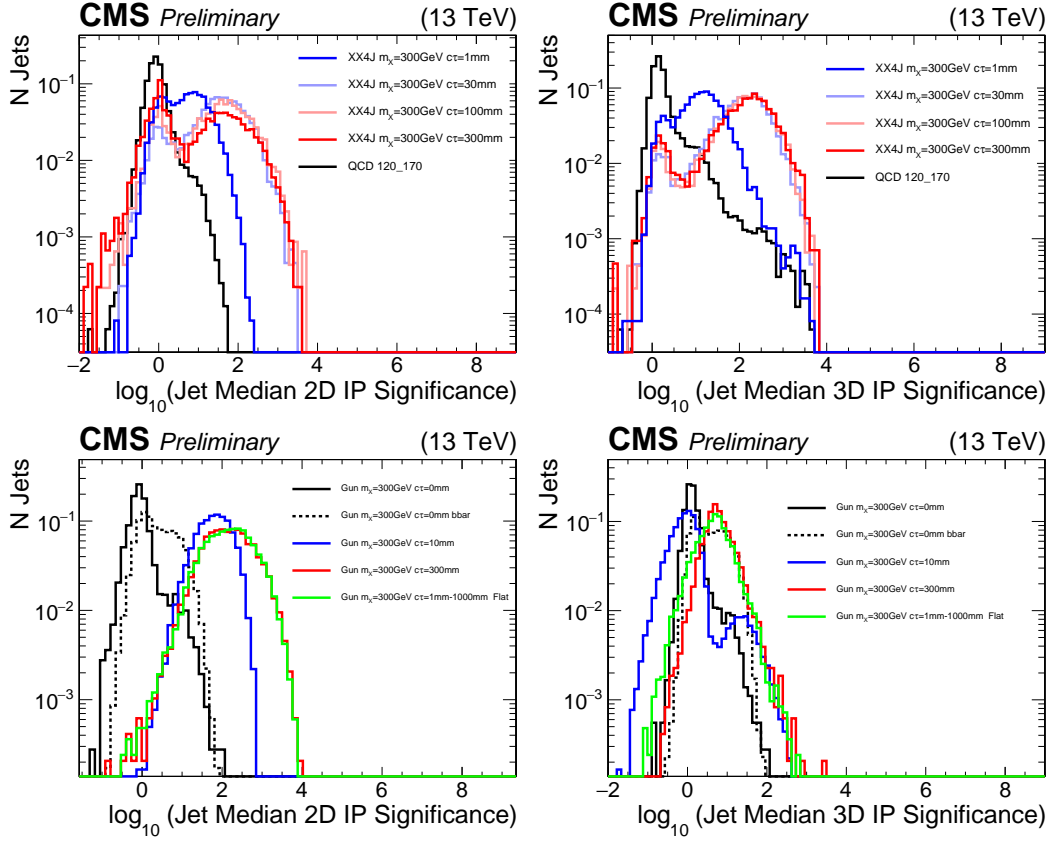


Figure 5.11: A comparison between the median IP Significance in 2D vs 3D for the displaced di-jet gun and XX4J signal samples

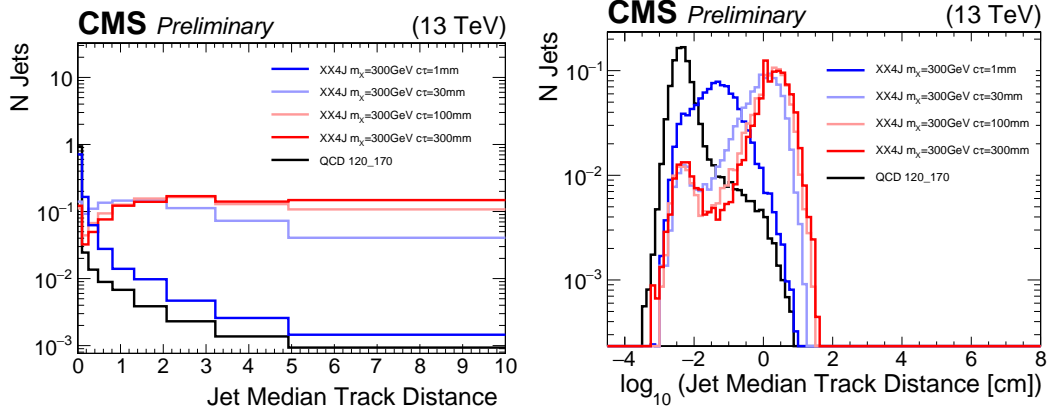


Figure 5.12: For each track in a jet the minimum distance between the track and the jet axis is computed. From this distribution the median is computed for each jet.

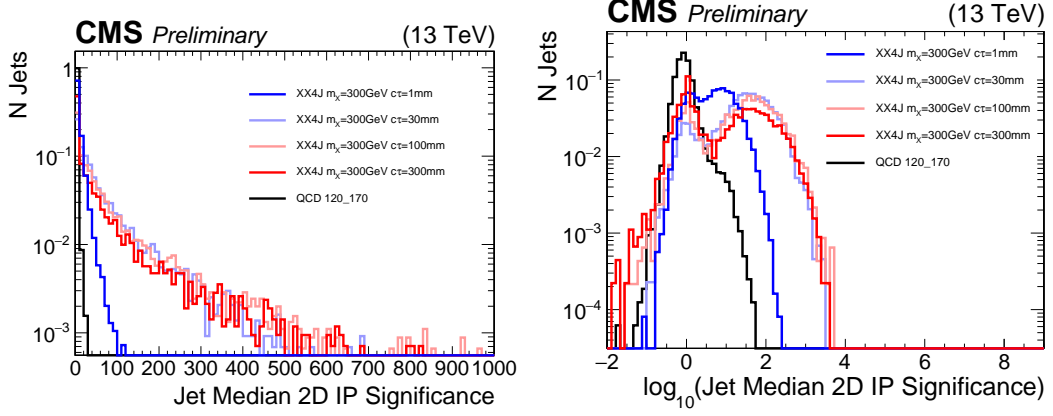


Figure 5.13: A comparison between log and linear scale variables. The log scale case shows the distinct population of significances related to pileup in the  $XX4J$  sample.

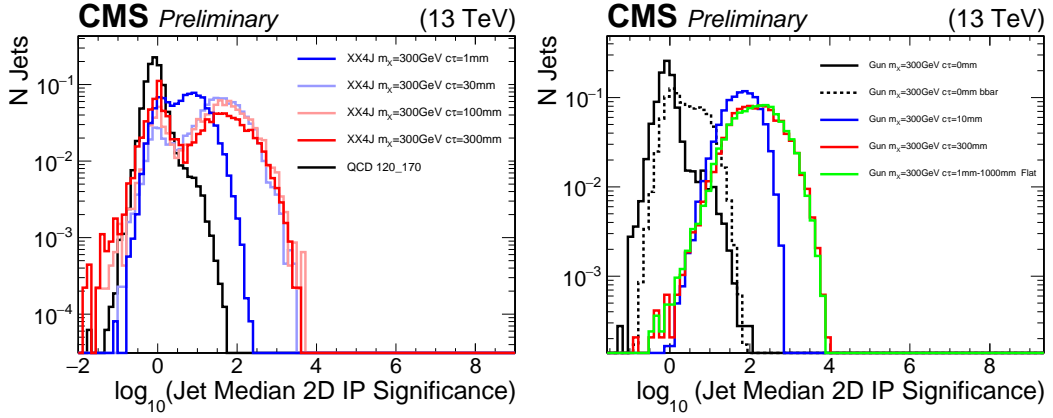


Figure 5.14: A comparison of the Jet Median 2D IP significance between the displaced di-jet gun and  $XX4J$  samples

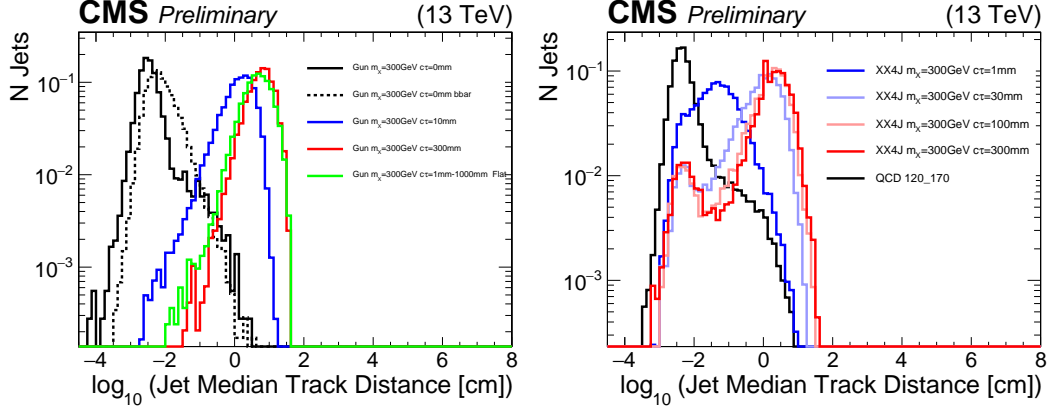


Figure 5.15: The closest distance between the jet axis and track

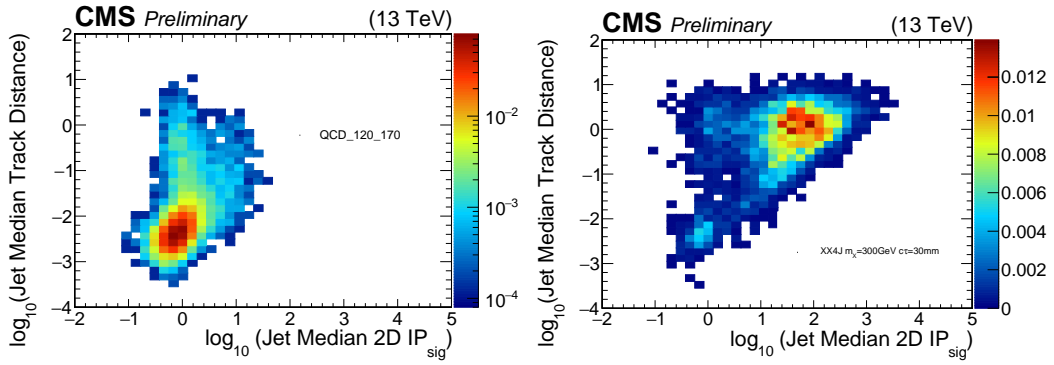


Figure 5.16: Correlations between the IP significance and the jet distance variables

### Jet Primary Vertex Fraction (Alpha and Beta)

Jets decaying displaced from the primary vertex are unlikely to contain tracks included in the event's primary vertex fit when a beam spot constraint is included. QCD jets, expect the majority of their tracks to be from either the true primary vertex or a pile up vertex. For a given jet  $\alpha(PV)$  is calculated as the sum is taken over tracks matching in  $\Delta R < 0.4$  between two collections of tracks: the tracks in the specified primary vertex and tracks from the `generalTracks` collection. The sum is restricted to tracks with  $p_t > 1.0$  GeV.

$$\alpha_{jet}(PV) = \frac{\sum_{i \in PV, tracks} p_t^i}{\sum_{j \in generalTracks} p_t^j} \quad (5.1)$$

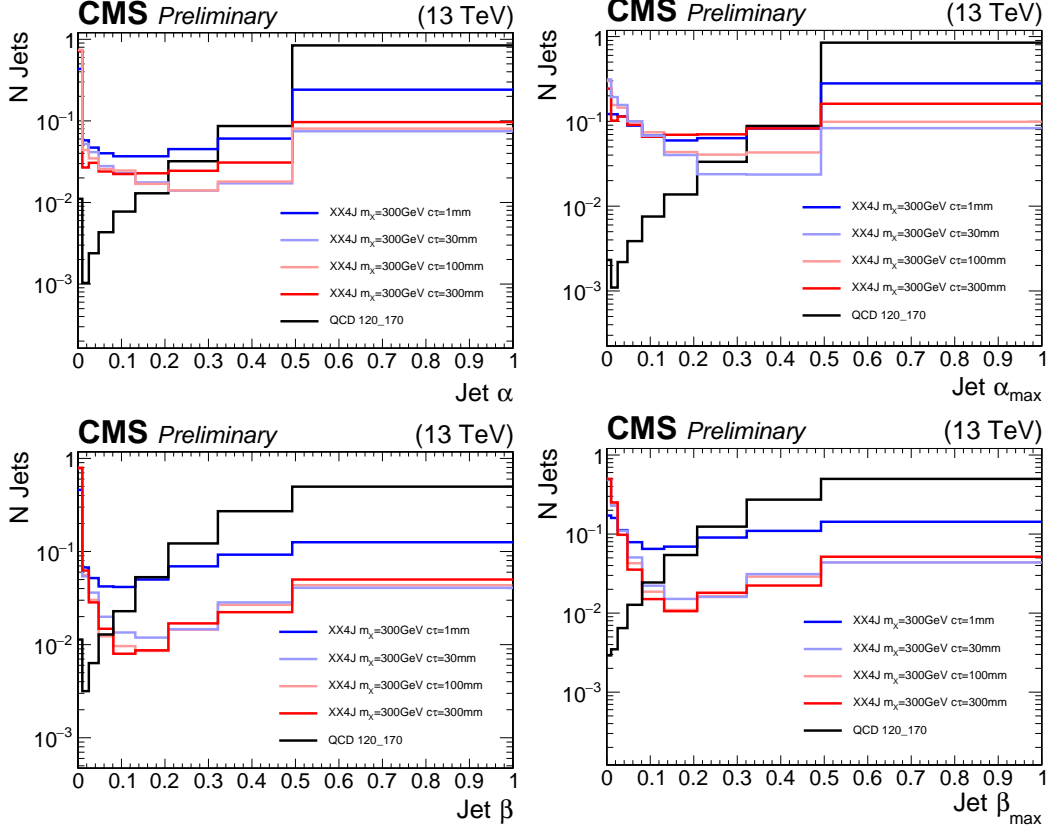


Figure 5.17:  $\alpha, \alpha_{max}, \beta, \beta_{max}$  when varying the lifetime of the decaying  $X^0$

If a single PV is selected for all jets in the event, PU jets which are not from this vertex can have signal-like  $\alpha \approx 0$ . To avoid this we define  $\alpha_{max}$  for each jet individually selecting the primary vertex with the largest contribution to the sum. The assumption is PU jets will have high  $\alpha$  for at least one of the vertices. Many events with  $\alpha = 0$  have  $\alpha_{max}! = 0$  as they originate from a sub-leading vertex in the `offlinePrimaryVerticesWithBS` collection. Because the **GUN** samples typically have no reconstructed primary vertices (except in the prompt case), these plots are not shown.

A second jet variable  $\beta(PV)$  and  $\beta_{max}$  are defined similarly:

$$\beta_{jet}(PV) = \frac{\sum_{i \in PV, tracks} p_t^i}{p_{t,jet}} \quad (5.2)$$

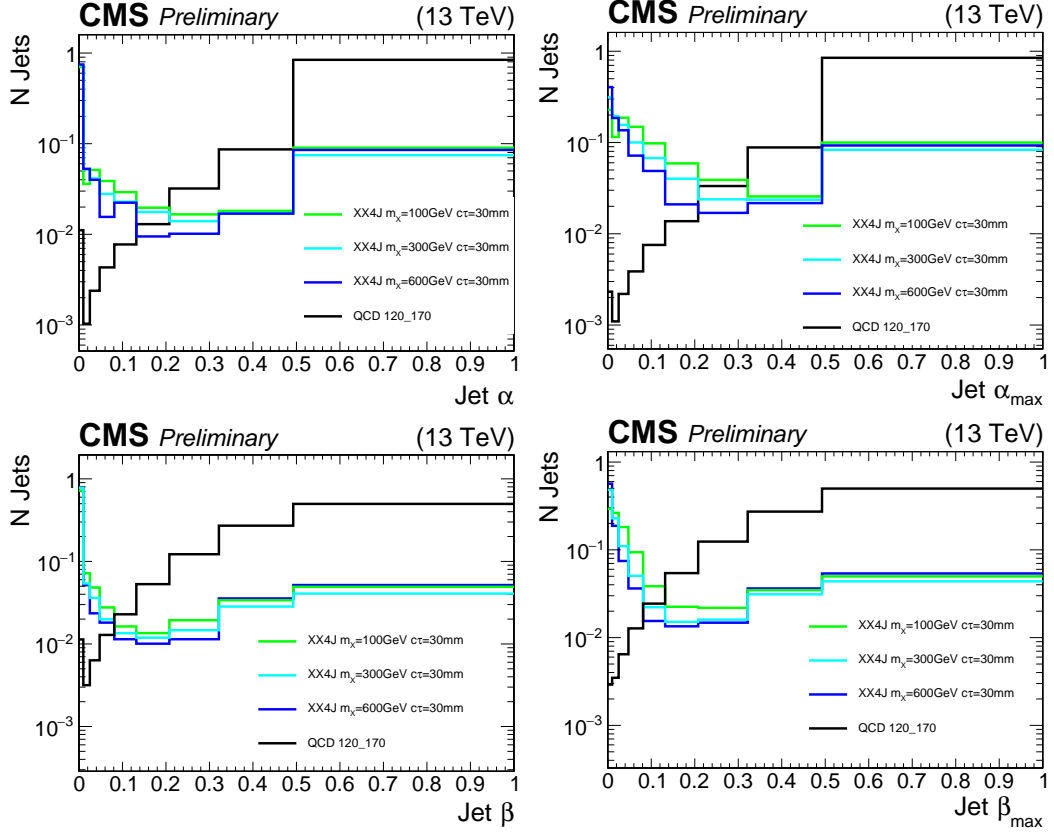


Figure 5.18:  $\alpha, \alpha_{max}, \beta, \beta_{max}$  when varying the mass of the decaying  $X^0$

A comparison of the four variables:  $\alpha, \alpha_{max}, \beta, \beta_{max}$  is shown in Fig. 5.17 varying the lifetime of the sample and in Fig. 5.18 varying the mass for fixed lifetime.

Fig 5.19 show  $\alpha_{max}$  has small correlation in background with the median 2D IP significance and  $\beta_{max}$  less so. This is because  $\alpha_{max}$  is a function of the tracks matched to the jet, which are utilized in the median IP significance calculation. At low values of  $\alpha_{max}$  we find the best separation between signal and background.

### 5.4.2 Calo Jet Information

In the case which there are no tracks to identify the decay as displaced, we can utilize the high hadronic energy fraction of jets that occur from decays in the hadronic

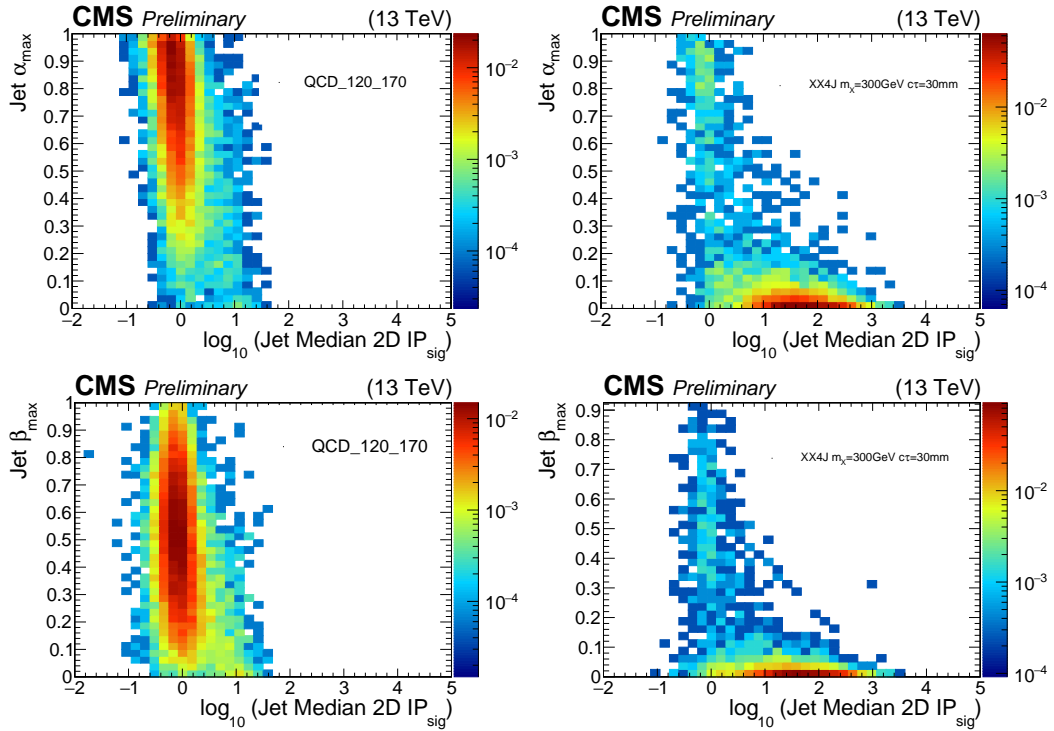


Figure 5.19: (Left) The correlation between  $\alpha_{max}$  and  $\beta_{max}$  and median 2D IP significance for QCD (Right) The same for XX4J with  $m_X = 300$  GeV and  $c\tau = 30\text{mm}$

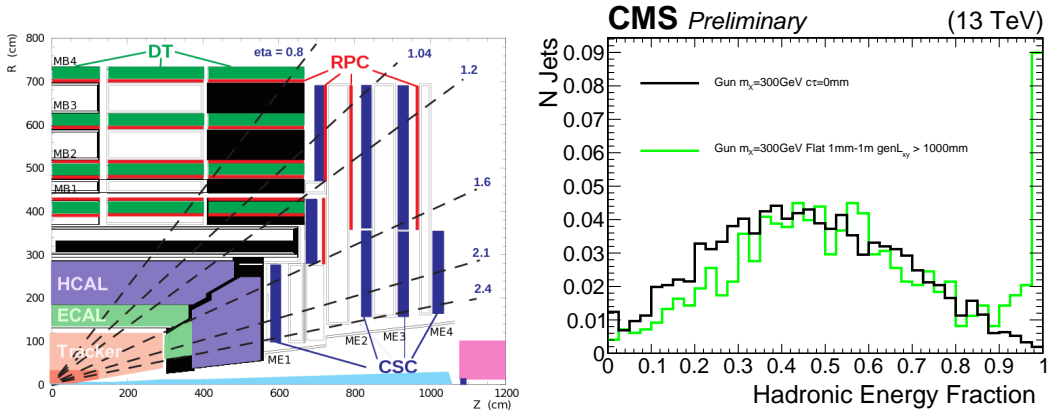


Figure 5.20: (Left) A longitudinal slice of the CMS detector showing the transverse coverage of the tracking layers. (Right) Hadronic fraction of jets in events with generator level requirement that the  $X^0$  decay at a transverse distance  $L_{xy} > 100\text{cm}$

calorimeter. Fig. 5.20 applies a generator level cut on the transverse decay distance of  $L_{xy} > 100$  cm to insure that the decay occurs outside of the tracker.

# Chapter 6

## Displaced Jet Analysis

### 6.1 Introduction

The study of physics beyond the standard model (BSM) is one of the main objectives of the ATLAS and CMS experiments at the CERN LHC. With no signal observed so far, the ATLAS and CMS results put severe bounds on BSM theories.

The majority of these searches focus on prompt particles with lifetimes  $c\tau_0 < 1\text{mm}$  and contain requirements on the physics objects that reject longer lived particle decays. This leaves open the possibility that light long-lived particles could exist and still remain undetected. In this paper, we present an inclusive search for long-lived particles decaying to various combinations of jets and leptons. The analysis exploits the information originating from the CMS calorimeters to reconstruct jets and measure their energies. The information from reconstructed tracks, in particular the transverse impact parameters, is used to discriminate the displaced-jets signal from the background of ordinary multijet events. The analysis is performed on data collected with the CMS detector at a center-of-mass energy  $\sqrt{s} = 13 \text{ TeV}$  in 2015. The data set corresponds to an integrated luminosity of  $2.7\text{fb}^{-1}$ . Results for similar

signatures have been reported by ATLAS [1, 2] and CMS [3], using data collected at  $\sqrt{s} = 8$  TeV.

## 6.2 Datasets

## 6.3 An inclusive displaced-jet tagger

The basic requirement for the displaced jet tagging criteria is at least a single track with  $p_t > 1$  GeV. Besides the requirements implicitly enforced on the iterative tracking in the `generalTracks` collection, there are no further requirements (no total and pixel hit requirements). All tracking related variables for tagging are computed with this collection of tracks i.e. `generalTracks` with  $p_t > 1$  GeV. There are no energy composition requirements of the calorimeter deposit and no requirements of a reconstructed secondary vertex, both of which can exclude sensitivity to long-lived decays to electrons and single prong taus.

All variables utilize 2D quantities. By excluding the longitudinal dimension we prevent large overestimation of displacement due to primary vertex mis-identification. When the signal model in question has a lifetime small on the scale of the longitudinal spread of pile up the primary vertex can still be accurately reconstructed. In contrast, for a decay in the lab frame of a few centimeters the probability of selecting the correct primary vertex can be highly model dependent. In fact, with beam spot constraints applied and no initial state radiation it is possible the primary vertex would not be reconstructed at all. This is especially the case for relatively light particles produced with lifetimes longer than the beamspot radius. By utilizing the `offlineBeamSpotWithBS` collection to compute primary vertex related quantities we limit the transverse spread relative to the z direction to approximately 0.001 cm. As

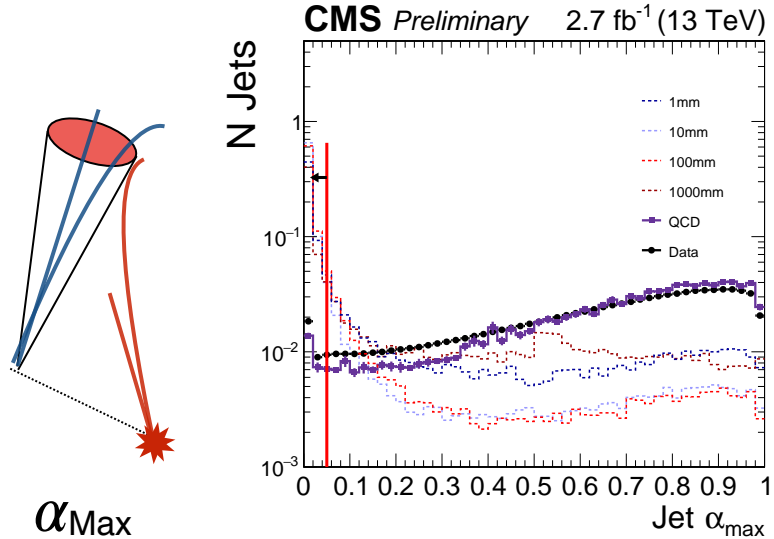


Figure 6.1: Diagram (left) and data/MC comparison (right) for the displaced jet tagging variable  $\alpha_{max}$ . The left distribution shows the data collected by the displaced jet triggers with kinematic cuts and  $H_T$  trigger matching thresholds applied. Signal samples are taken from Jet-Jet interpretation with no generator matching for the signal jets, fixed  $m_X = 700$  GeV and varied proper lifetime  $c\tau_0$  in the mother frame.

the tag sensitivity becomes highly insensitive at distances smaller than 1 mm, the effect of choosing the wrong PV is negligible.

In contrast to previous analyses, a fitted secondary vertex is not utilized in the tag definition. This decision is deliberate to maintain sensitivity to electrons and single track taus while maintaining a single definition. Previous analyses had possible sensitivity by fitting a secondary vertex to pairs of jets containing a single track. Additionally, by not vertexing pairs of jets the displaced object allows for sensitivity to odd (non-even) multiplicities of displaced jets. For example, in the Jet-Jet interpretation there is sensitivity to 3 jets when the 4th is reconstructed outside of the tracker acceptance.

## The Primary Vertex Compatibility Variable Alpha Max

The variable  $\alpha_{max}$  characterizes the disassociation of the jet's tracks and all fitted primary vertices in an event. Jets decaying displaced from the primary vertex are unlikely to contain tracks included in the event's primary vertex fit. Background QCD jets, will contain a majority of tracks from either the true primary vertex or a pile up vertex. For a given jet  $\alpha(PV)$  is calculated as the ratio of sums of  $p_t$  taken over tracks matching in  $\Delta R < 0.4$  between two collections of tracks: the tracks in the specified primary vertex and tracks from the `generalTracks` collection. The sum is restricted to tracks with  $p_t > 1.0$  GeV.

$$\alpha_{jet}(PV) = \frac{\sum_{i \in PV, tracks} p_t^i}{\sum_{j \in generalTracks} p_t^j} \quad (6.1)$$

If a single PV is selected for all jets in the event, PU jets which are not from this vertex can have signal-like  $\alpha \approx 0$ . To avoid this, we define  $\alpha_{max}$  for each jet individually selecting the primary vertex with the largest contribution to the sum. The assumption is PU jets will have high  $\alpha$  for at least one of the vertices. Many jets with  $\alpha = 0$  have  $\alpha_{max} > 0$  as they originate from a sub-leading vertex in the `offlinePrimaryVerticesWithBS` collection. As the variable is calculated relative to all primary vertices, there is no dependence on selecting a single vertex.

## The 2D Angle $\Theta_{2D}$

The variable  $\Theta_{2D}$  is utilized to characterize the recoil angle of the tracks from the flight direction of the long lived particle.  $\Theta_{2D}$  is defined as the angle between 1) the 2D ray extended from the primary vertex to the inner hit of the track and 2) the track 2D momentum vector at the inner hit of the track extended from the inner hit. The first vertex in the `offlinePrimaryVertexWithBS` collection is selected for all jets in the event.

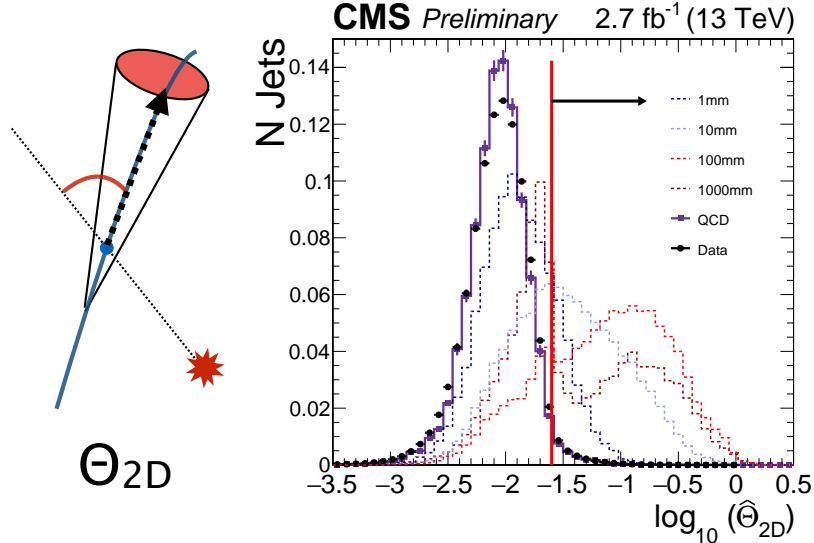


Figure 6.2: Diagram (left) and data/MC comparison (right) for the displaced jet tagging variable  $\theta_{2D}$ . The left distribution shows the quantities collected by the displaced jet triggers with kinematic cuts and  $H_T$  trigger matching thresholds applied. Signal samples are taken from Jet-Jet interpretation with no generator matching for the signal jets, fixed  $m_X = 700$  GeV and varied proper lifetime  $c\tau_0$  in the mother frame.

As Standard Model QCD jets do contain long lived particles and tracks associated to conversions, a typical jet has a long tail in its distribution of  $\Theta_{2D}$ . To minimize the effect of this tail, the median value (2D) is used,  $\hat{\Theta}_{2D}$  (for the same reasons as it is used for  $2DIP_{sig}$ ). Additionally, as the range of  $\Theta_{2D}$  spans many orders of magnitude near zero a logarithm is applied constraining typical QCD jet values of  $-2.5 < \log(\hat{\Theta}_{2D}) < -1$ .

As mentioned previously, the smaller the boost of the particle, the more isotropic the decay angles. Thus, the decays of heavier long-lived particles yield larger values of  $\Theta_{2D}$ . When the lifetime of the particle is small near 1 mm it is more difficult to resolve this angle because the ray's extrapolation backward corresponds to a smaller and smaller distance from the primary vertex . As the lifetime approaches a few centimeters the signal is up to 50% efficient in a nearly background free regime.

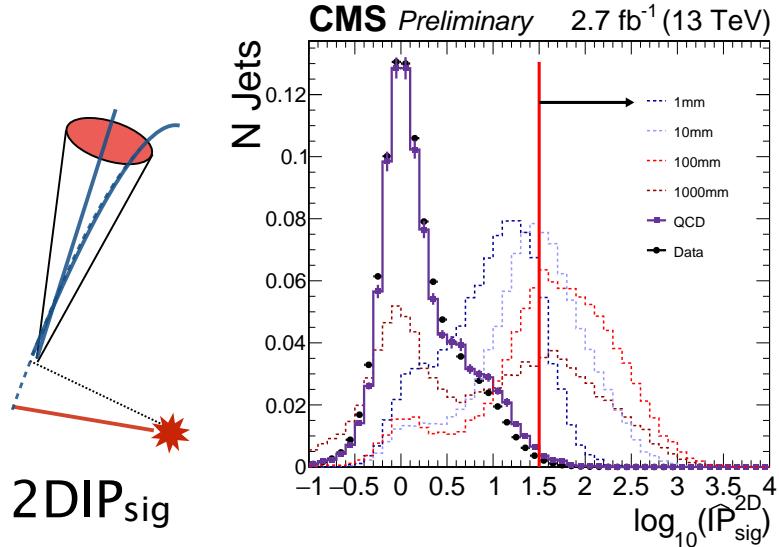


Figure 6.3: Diagram (left) and Data vs. Monte Carlo comparison (right) for the displaced jet tagging variable  $2DIP_{sig}$ . The left distribution shows the quantities collected by the displaced jet triggers with kinematic cuts and  $H_T$  trigger matching thresholds applied. Signal samples are taken from Jet-Jet interpretation with no generator matching for the signal jets, fixed  $m_X = 700$  GeV and varied proper lifetime  $c\tau_0$  in the mother frame.

Background jets capable of passing tight  $\Theta_{2D}$  requirements typically consist of a single track.

### Jet $2DIP_{sig}$

Variables leveraging the impact parameter information for a given jet are derived from the distribution of impact parameter significances derived from the tracks matched to the jet. As background QCD jets contain a long tail from the presence of real displaced tracks with large IP significance, the median  $2DIP_{sig}$  is chosen:  $\hat{IP}_{sig}^{2D}$ . For jets originating from displaced decay, most tracks have a large impact parameter preserving a high median value.

Table 6.1: The baseline tag definition in terms of the three displaced jet tagging variables

Tagging Variable	$\log_{10}(x)$ Requirement	Linear Requirement
$\alpha_{max}$	N/A	< 5%
$\hat{IP}_{sig}^{2D}$	> 1.5	> 31.6
$\hat{\Theta}_{2D}$	> -1.6	> 0.025

Table 6.2: The loose tag definition in terms of the three displaced jet tagging variables.

Tagging Variable	$\log_{10}(x)$ Requirement	Linear Requirement
$\alpha_{max}$	N/A	< 50%
$\hat{IP}_{sig}^{2D}$	> 0.434	> 2.71
$\hat{\Theta}_{2D}$	> -1.70	> 0.02

### 6.3.1 Tagging Variable Cut Optimization

The requirements included in the baseline tag definition are determined through a scan of the possible parameter space. The values of the tagging variables scanned can be found in Table 6.4. Firstly, a scan is performed to determine the optimal selection relative to a figure of merit that is maximal labeled  $fom_{max}(x)$  for a given sample  $x \in X$  where  $X$  is the set of training samples. The figure of merit for a given sample  $x \in X$  and selection  $s_i \in S$  is computed as  $fom(x, s_i) = \bar{N}(s_i, x) / \sqrt{\bar{N}(s_i, x) + \hat{N}_b(s_i)}$  where  $\bar{N}$  is the average number of jets tagged per event passing the event selection and  $\hat{N}_b$  is an estimate number of background events in the two tag bin. This estimation

Table 6.3: The integrated fake-rate is precisely  $N_{tagged}/N_{jets}$  for all jets passing the jet selection in events passing the event selection in data collected by the displaced jet triggers.

Working Point	Flat Fake-Rate / Probability
Loose Tag	2.5816%
Baseline Tag	0.0496%

Table 6.4: The values of the tagging variables included in the scan for selecting the baseline tag definition

Tagging Variable	Begin Scan	End Scan	Step Size	N Points
$\alpha_{max}$	0	0.5	0.05	11
$\log_{10}(\hat{IP}_{sig}^{2D})$	0.0	2.5	0.1	26
$\log_{10}(\hat{\Theta}_{2D})$	-2.5	-0.5	0.1	21

$\hat{N}_b$  is calculated as the total number of jets tagged in data times the fake rate  $\hat{N}_b(s_i) = N_{jets-tagged}^{data} \times \frac{N_{jets-tagged}^{data}}{N_{jets}^{data}}$ . Once  $fom_{max}$  is calculated for every sample and selection we choose the tagging requirements which minimize sum of the differences squared of the figure of merit  $fom(s_i, x)$  relative to the maximal value  $fom_{max}$  Eq. 6.2.

$$\chi^2(s_i) = \sum_{x \in X} \left( \frac{(fom(s_i, x) - fom_{max}(x))^2}{fom_{max}(x)} \right) \quad (6.2)$$

The training set is chosen as the set of all Jet-Jet samples with  $c\tau_0 = 1, 3$  mm. This set is chosen as it is the most difficult region for the analysis with the largest upper limit on the excluded cross-section.

## 6.4 Event selection

A signal is searched for by applying the selection described in section ?? and counting the number of tagged displaced jets,  $N_{tags}$ . In addition to the online and offline requirements described in section 6.5, the analysis signal region requires  $N_{tags} \geq 2$ . Efficiencies are reported for all interpreted models as a function of the lifetime with fixed mass (Table 6.5 and 6.6) as well as a function of mass with fixed lifetime (Table 6.7 and 6.8).

Table 6.5: Signal efficiency for fixed  $m_X = m_{\tilde{t}} = 300$  GeV and varied  $c\tau_0$  for the Jet-Jet and B-Lepton models. Selection requirements are cumulative from the first to the last row.

<b>Jet-Jet</b>				
$m_X$ [GeV]	300	300	300	300
$c\tau_0$ [mm]	1	10	100	1000
$\geq 2$ tags	$2.33 \pm 0.15\%$	$39.49 \pm 0.63\%$	$54.54 \pm 0.74\%$	$14.58 \pm 0.38\%$
Trigger	$2.16 \pm 0.15\%$	$38.12 \pm 0.62\%$	$39.32 \pm 0.63\%$	$8.07 \pm 0.28\%$
Event sel.	$2.09 \pm 0.14\%$	$37.09 \pm 0.61\%$	$36.53 \pm 0.60\%$	$6.67 \pm 0.26\%$
$\geq 3$ tags	$0.170 \pm 0.041\%$	$14.14 \pm 0.38\%$	$16.72 \pm 0.41\%$	$1.36 \pm 0.12\%$
$\geq 4$ tags	$0.010 \pm 0.010\%$	$4.73 \pm 0.22\%$	$4.71 \pm 0.22\%$	$0.170 \pm 0.041\%$

<b>B-Lepton</b>				
$m_{\tilde{t}}$ [GeV]	300	300	300	300
$c\tau_0$ [mm]	1	10	100	1000
$\geq 2$ tags	$0.453 \pm 0.023\%$	$15.82 \pm 0.13\%$	$31.52 \pm 0.19\%$	$8.545 \pm 0.098\%$
Trigger	$0.291 \pm 0.018\%$	$11.45 \pm 0.11\%$	$17.08 \pm 0.14\%$	$3.224 \pm 0.060\%$
Event sel.	$0.269 \pm 0.017\%$	$9.91 \pm 0.11\%$	$13.33 \pm 0.12\%$	$2.084 \pm 0.048\%$
$\geq 3$ tags	$0.017 \pm 0.004\%$	$2.462 \pm 0.053\%$	$3.814 \pm 0.065\%$	$0.368 \pm 0.020\%$
$\geq 4$ tags	–	$0.297 \pm 0.018\%$	$0.480 \pm 0.023\%$	$0.0315 \pm 0.0060\%$

The two classes of events: (i) events passing the inclusive trigger algorithm and with  $H_T > 650$  GeV; (ii) events passing the exclusive trigger algorithm and with  $H_T > 450$  GeV are treated as a single class.

## 6.5 Datasets and simulated samples

Events are collected from two dedicated online selection algorithms, designed to identify events with displaced jets. The algorithms consider jets clustered from energy deposits in the calorimeters, using the FASTJET [4] implementation of the anti- $k_t$  algorithm [5], with size parameter 0.4. Jets with transverse momentum  $p_t < 60$  GeV or  $|\eta| > 2.0$  are discarded. An inclusive trigger algorithm accepts events when the scalar sum of the jet  $p_t$ 's,  $H_T$ , is greater than 500 GeV and at least two jets with  $|\eta| < 2.0$  and at most two prompt tracks are found. Tracks are classified as prompt if

their transverse impact parameter relative to the beam line,  $IP^{2D}$ , is less than 1mm. Another trigger algorithm is used, which requires  $H_T > 350$  GeV and asks that there be two displaced jets each having at least one track with transverse impact parameter  $IP^{2D} > 5\sigma_{IP^{2D}}$ , where  $\sigma_{IP^{2D}}$  is the uncertainty on  $IP^{2D}$ . Samples with large  $H_T$  are used to study the performance of the online selection algorithms.

Events are selected offline requiring at least two jets with  $p_t > 60$  GeV and  $|\eta| < 2.0$ . As for the online selection, the offline jet reconstruction is performed clustering energy deposits in the calorimeters with the anti- $k_t$  algorithm, with jet size parameter of 0.4. Two classes of events are considered: (i) events passing the inclusive trigger algorithm and with  $H_T > 650$  GeV and (ii) events passing the exclusive trigger algorithm and with  $H_T > 450$  GeV. The two classes of events sum to 786,002 unique events passing the event selection.

The main source of background events originates from multijet production. The properties of this background process are studied using a simulated multijet sample, generated with PYTHIA 8 [6]. The NNPDF 2.3 [7] parton distribution functions (PDFs) are used to model the parton momentum distribution inside the colliding protons. The event simulation includes the effect of multiple proton-proton collisions in the same bunch crossing and in bunch crossing nearby in time, referred to as pileup. Simulated samples are reweighted to match the pileup profile observed in data.

The analysis is interpreted with a set of benchmark signal models. The **Jet-Jet** model predicts pair-produced long-lived scalar neutral particles  $X^0$  [8], each decaying to two light quarks u,d,s,c, and b with equal probability. The resonance mass  $m_X$  and proper lifetime  $c\tau_0$  are scanned between 50 and 1500 GeV and between 1 and 2000mm, respectively. The trigger efficiencies for a fixed  $m_X = 300$  GeV and  $c\tau_0 = 1, 30$ , and 1000 mm are 30%, 81%, and 42% respectively. The trigger efficiencies for a fixed  $c\tau_0 = 30$  mm and  $m_X = 50, 100$ , and 1000 GeV are 2%, 14%, and 92% respectively.

The **B-Lepton** model contains pair-produced long-lived top squarks in R-parity violating models of Supersymmetry [9]. Each top squark decays to one b quark and a lepton. The branching fractions of the decay to the three lepton flavors are equal. The resonance mass  $m_{\tilde{t}}$  and proper lifetime  $c\tau_0$  are scanned between 300 and 1000GeV and between 1 and 1000mm, respectively. The trigger efficiencies for a fixed mass  $m_{\tilde{t}} = 300$  GeV and  $c\tau_0 = 1, 30$ , and 1000 mm are 15%, 41%, and 23% respectively. The trigger efficiencies for  $m_{\tilde{t}} = 500, 700$ , and 1000 GeV and fixed  $c\tau_0 = 30$  mm are 64%, 71%, and 74% respectively.

These models are also investigated with modified branching fractions. The **Light-Light** model is the Jet-Jet model excluding decays to b quarks (equal decays to lighter quarks) and the **B-Mu**, **B-Ele**, and **B-Tau** models are derived from the B-Lepton model with 100% branching fraction to muons, electrons, and taus, respectively. Leptonic tau decays are included in the **B-Tau** interpretation. All signal samples are generated with PYTHIA, with the setup described above for the multijet sample.

## 6.6 Background prediction

As typical multijets contain only a sub dominant fraction of real displaced tracks, jets with a small multiplicity of tracks represent the dominant background. As the tagging criteria utilize averages of all tracks matched to the jet, the likelihood of tagging a fake decreases exponentially with  $N_{\text{tracks}}$ .

Figure 6.4 shows the fraction of jets that are tagged as displaced jets in data as a function of the number of tracks associated with the jet  $N_{\text{tracks}}$ . This function is the misidentification rate of tagging a prompt jet as displaced (up to possible signal contamination) and is interpreted as the probability  $p(N_{\text{tracks}})$  of being tagged. This parameterization allows for a representative estimation, event by event, of the probability of tagging multiple fake displaced jets. That is to say, an event with two

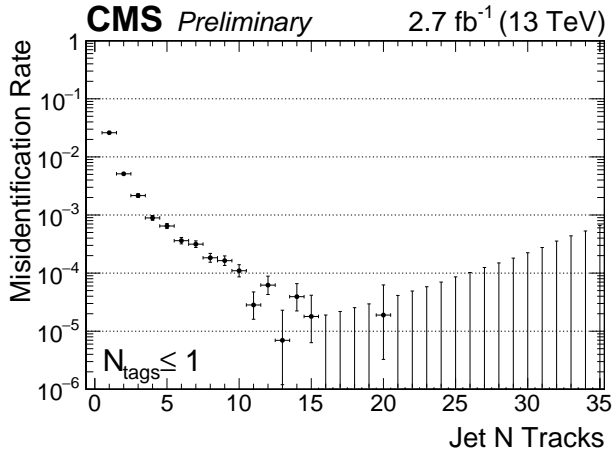


Figure 6.4: The fraction of jets passing the displaced-jet tagging criteria as a function of the number tracks associated with the jet  $N_{\text{tracks}}$ . The results are from data events with  $N_{\text{tags}} \leq 1$  collected with the displaced-jet triggers and passing the offline selection criteria.

high track multiplicity jets is much less probable than two single track jets to have 2 fake displaced-jet tags.

To maintain the statistical independence of the events that are used to perform the prediction and the events in the signal region, the probabilities are measured in the full control sample of events with  $N_{\text{tags}} \leq 1$ , while the final signal region requires  $N_{\text{tags}} \geq 2$ . Additionally, this limits signal contamination in the probability measurement. The control sample of  $N_{\text{tags}} = 1$  includes 1391 events.

The size of the bias introduced by only measuring the misidentification rate in events with  $N_{\text{tags}} \leq 1$  is quantifiable. For the nominal tag the size of the effect of removing these events on the predicted number of two tag events is negligible (0.4%) compared to the statistical uncertainty of the prediction.

The mistagging rate is used to predict the probability for an event to have  $N_{\text{tags}}$  tagged jets,  $P(N_{\text{tags}})$ . For instance, for an event  $m$  with three jets  $j_1$ ,  $j_2$ , and  $j_3$ ,

there is one configuration with no tags, with a probability:

$$P^m(N_{\text{tags}} = 0) = (1 - p_1)(1 - p_2)(1 - p_3) ,$$

where  $p_i = p(N_{\text{tracks}}(j_i))$ . Similarly, there are three possibilities for this same event to have  $N_{\text{tags}} = 1$ :

$$P^m(N_{\text{tags}} = 1) = p_1(1 - p_2)(1 - p_3) + (1 - p_1)p_2(1 - p_3) + (1 - p_1)(1 - p_2)p_3 .$$

The probability of finding  $N_{\text{tags}}$  tags in the  $m$  event is:

$$P^m(N_{\text{tags}}) = \sum_{\text{jet-configs}} \prod_{i \in \text{tagged}} p_i \prod_{k \in \text{not-tagged}} (1 - p_k) . \quad (6.3)$$

Tagged jets enter the product as  $p_i$  and non-tagged jets enter as  $(1 - p_i)$ . Equation (6.3) is used to compute the probability of observing  $N_{\text{tags}}$ , under the assumption that the sample does not contain any signal. The number of events expected for a given value of  $N_{\text{tags}}$  is then computed as

$$N_{\text{events}}(N_{\text{tags}}) = \sum_m P^m(N_{\text{tags}}) , \quad (6.4)$$

where  $m$  runs only over events with fewer than two tagged jets. The prediction is then compared to the observed  $N_{\text{tags}}$  multiplicity in events with two or more tagged jets, to assess the presence of a signal.

Let  $q_i$  be the misidentification rate corresponding to a jet with  $i$  tracks and  $N_{\text{tracks}}$  the maximum number of tracks for any jet in the analysis. The statistical error  $\sigma_{q_i}$  in the misidentification rate is propagated to an error on the number of tagged events

with  $N_{tags} = 1, 2, 3, \dots$

$$\begin{aligned}\sigma_{N_{n-tags}}^2 &= \sum_{i=1}^{N_{tracks}} \left( \frac{\partial N_{n-tags}}{\partial q_i} \sigma_{q_i} \right)^2 \\ &= \sum_{i=1}^{N_{tracks}} \left( \left( \sum_{m \in N_{events}} \frac{\partial P^m(N_{tags} = n)}{\partial q_i} \right) \sigma_{q_i} \right)^2\end{aligned}$$

The probability is determined for each event for  $N_{tags} \leq N_{jets}$ . The predicted number of events with  $N_{tags}$  is calculated as the sum over all events Eq. ??.

We validate this procedure in the absence (background-only test) and presence (signal-injection test) of a signal, using simulated events.

The background-only test is performed predicting the tag multiplicity on the simulated multijet sample, taking as input the misidentification rate distribution. In order to populate the large- $N_{tags}$  region of the distribution, a looser version of the displaced-jet tagger is employed in this test. The full sample of events passing the event selection is divided into multiple independent samples and the background prediction validated. The predicted background of  $N_{tags}$  events in simulated multijet events is found to be consistent within statistical uncertainty.

### 6.6.1 Signal Injection Tests

#### Injection with QCD

To test the response of the background prediction to the presence of signal contamination in the jet probabilities used for the  $P(N_{tags})$  derivation, signal events are ‘injected’ into QCD Monte Carlo. Approximately 15 million QCD events from /QCD\\_HT700to1000\\_TuneCUETP8M1\\_13TeV-madgraphMLM-pythia8 are used as the background input. The resulting predictions for varied masses, lifetimes, and sizes of contamination are shown in Fig. 6.5 and Fig. 6.6. The corresponding predictions, observed number of tags, and the deviation from expectation are summarized in

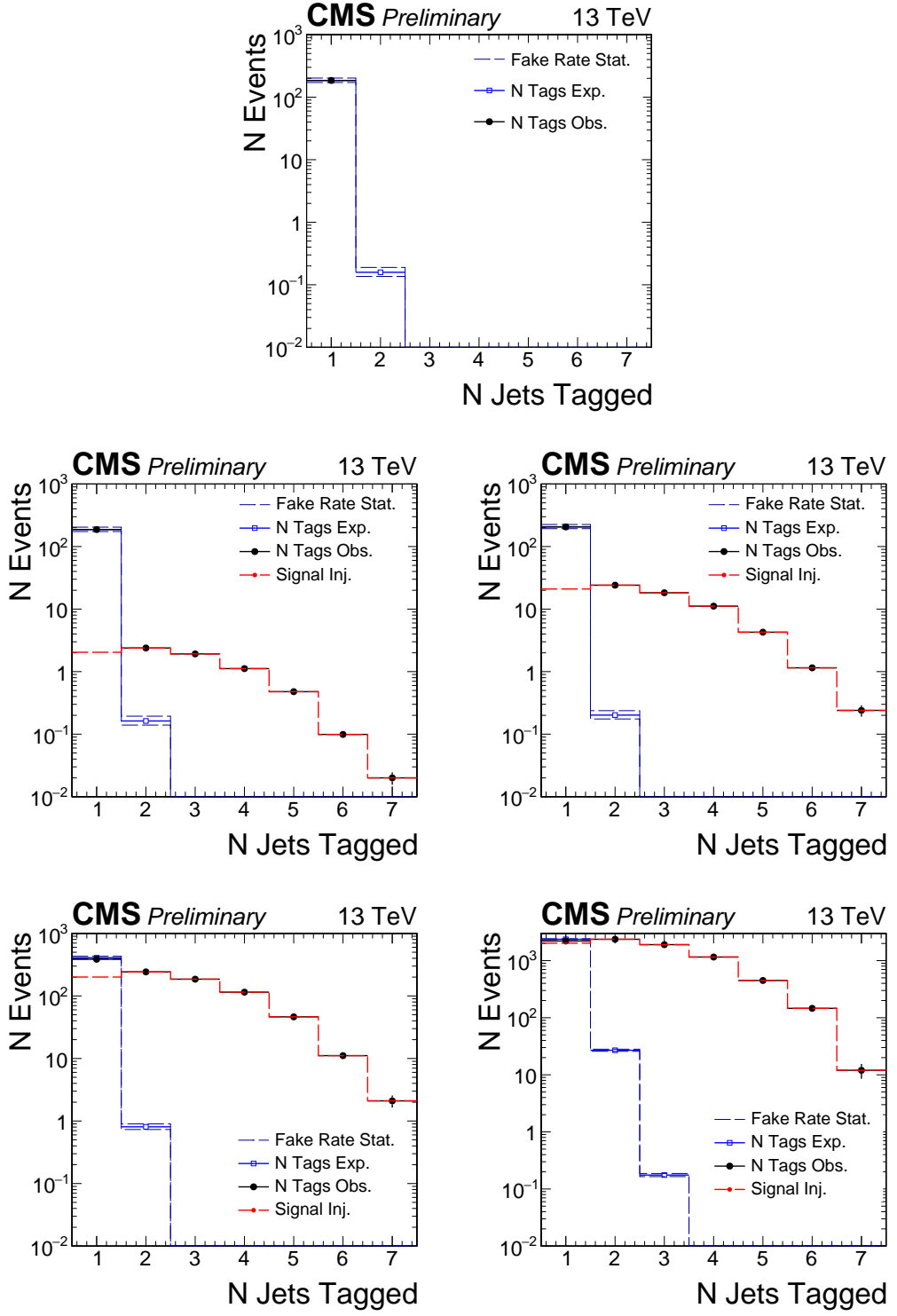


Figure 6.5: Signal Injection tests. The Jet-Jet signal sample used has fixed  $m_X = 700\text{GeV}$  and  $c\tau_0 = 10 \text{ mm}$ . The level of signal contamination is progressively varied between 10, 100, 1000, and 10000 events injected before any selection. The full event selection is applied and the baseline jet tag definition.

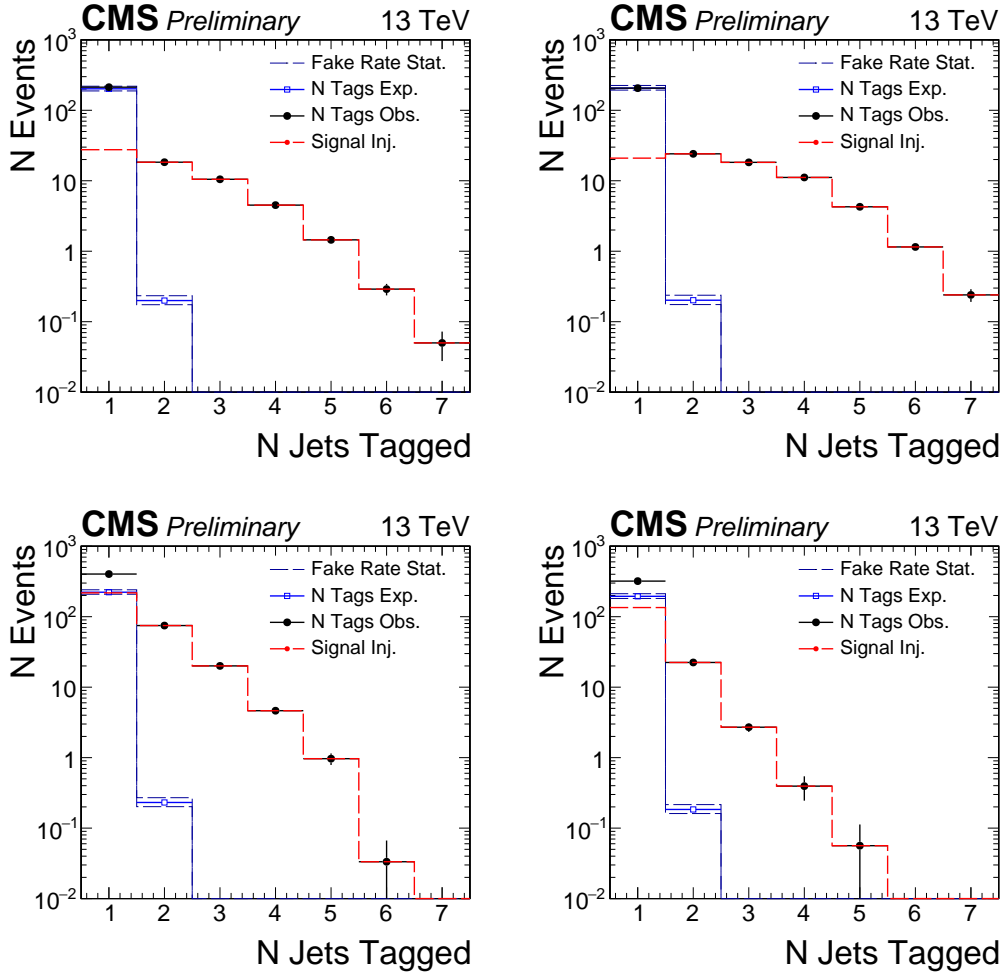


Figure 6.6: Signal Injection. The Jet-Jet signal sample is varied  $m_X = 700 \text{ GeV}$  and  $c\tau_0 = 1000 \text{ mm}$  (top left)  $m_X = 700 \text{ GeV}$  and  $c\tau_0 = 10 \text{ mm}$  (top right)  $m_X = 100 \text{ GeV}$  and  $c\tau_0 = 1000 \text{ mm}$  (bottom left)  $m_X = 100 \text{ GeV}$  and  $c\tau_0 = 10 \text{ mm}$  (bottom right). The level of signal contamination is fixed at 100 events for the  $m_X = 700 \text{ GeV}$  and 1000 events for  $m_X = 100 \text{ GeV}$ . The full event selection is applied and the baseline jet tag definition.

Table 6.9 and Table 6.10. The goal of this exercise is to understand the quantity of signal contamination, as well as lifetime and mass, required to significantly alter the background prediction.

The resulting predictions are also reported normalized such that the total signal + qcd events passing the event selection are equal to the number of events passing the event selection in the analysis in Table 6.11.

The change in the  $N_{tags}^{obs}$  distribution to the presence of signal is on the order of the number of events with  $N_{tags} > 2$  whereas the integrated shift in  $P(N_{tags} \geq 2)$  is on the order of the shift induced in the  $p(j)$  distribution. This shift is of the order the signal contamination. We can conclude the analysis will retain relative sensitivity as long as the signal contamination is relatively smaller than the QCD contribution in the fake rate calculation.

In summary, the background prediction is robust to a variety signal masses, lifetimes and sizes of contamination. Robust in the sense that the background is correctly determined within error in the 0 injection case and the bias to the background prediction due to the contamination is small relative to the number of signal events injected.

The following section explores the sensitivity to signal explicitly in a simplified scenario given the assumption that the jet probabilities accurately predict the background in the scenario where there are no signal events present. This assumption is based on the closure studies in the previous section and be considered true within some closure systematic.

### Explicit Sensitivity in A Simplified Injection Scenario

Consider a sample of  $N_{QCD}$  QCD events with a known fraction of jets that are tagged  $f(j_i)$  as a function of some jet parameters  $j_i$ . For simplicity, assume events have exactly 2 jets. Also assume we have shown that the observation approximately deter-

mined  $N_{obs}^{2tag} = N_{pred}^{2tag}$  when we interpret  $f(j_i)$  as a conditional probability  $p(j_i)$  such that:

$$N_{obs}^{2tag} = N_{pred}^{2tag} = \sum_i [p(j_1)p(j_2)]_i = N_{QCD}p^2$$

where we are using a flat probability  $p$  such that  $p(j_1) = p(j_2) = p = n_{tag}/n_{jets} = n_{fake}/2N_{events}$ . Where  $n_{tag}$  is the number of jets tagged, which in a QCD sample is exactly  $n_{fake}$ . Now, say we perform the signal injection test by injecting  $N_{sig}$  events with correspondingly  $2N_{sig}$  signal jets. Let  $\epsilon$  be the efficiency for a signal event to have 1 tag. Accordingly the probability will shift  $p(j_i) \rightarrow \tilde{p}(j_i)$ :

$$\tilde{p} = \frac{n_{fake} + n_{true-tags}}{2N_{QCD} + 2N_{sig}} = \frac{n_{fake} + \epsilon 2N_{sig}}{2N_{QCD} + 2N_{sig}}$$

Taylor expanding in  $N_{sig}$  about 0 we obtain:

$$\begin{aligned} \tilde{p} &= \frac{n_{fake}}{2N_{QCD}} - \frac{N_{sig}n_{fake}}{2(N_{QCD})^2} + \epsilon \frac{2N_{sig}N_{QCD}}{2(N_{QCD})^2} \\ &= p - p \frac{N_{sig}}{N_{QCD}} + \frac{N_{sig}\epsilon}{N_{QCD}} \end{aligned}$$

Let  $\Delta = N_{sig}/N_{QCD}$

$$\tilde{p} = p(1 - \Delta) + \Delta\epsilon$$

Note that as the signal contamination  $\Delta \rightarrow 0$ , we obtain the correct probability  $\tilde{p} = p$ . Now we attempt to predict the number of events with 2 tags using  $\tilde{p}$  and splitting

the sum over signal and QCD events.

$$\begin{aligned}
N_{pred}^{2tag} &= \sum_i \tilde{p}\tilde{p} \\
&= \sum_i (p(1 - \Delta) + \Delta\epsilon)^2 \\
&= \sum_i p^2 - p^2(2\Delta) + p^2\Delta^2 + 2p\Delta\epsilon - 2p\Delta^2\epsilon + \Delta^2\epsilon^2
\end{aligned}$$

We now split the events in the sum between QCD and Signal.

$$\begin{aligned}
N_{pred}^{2tag} &= \sum_i (QCD) + \sum_i (Signal) \\
\sum_i (QCD) &= N_{QCD}(p^2 - p^2(2\Delta) + p^2\Delta^2 + 2p\Delta\epsilon - 2p\Delta^2\epsilon + \Delta^2\epsilon^2) \\
&= N_{obs}^{QCD} - N_{sig}(p^2\Delta + \Delta\epsilon^2 - 2p^2 + 2p\epsilon - 2p\Delta\epsilon)
\end{aligned}$$

where we have used the fact that  $\Delta N_{QCD} = N_{sig}$  and  $\sum_i p^2 = N_{obs}^{QCD}$ :

$$\sum_i (Signal) = N_{sig}(p^2 - p^2(2\Delta) + p^2\Delta^2 + 2p\Delta\epsilon - 2p\Delta^2\epsilon + \Delta^2\epsilon^2)$$

We now evaluate our sensitivity to signal or equivalently the disagreement between observed and prediction by the variable  $S$ . Let  $N_{obs}^{2tag} = N_{obs}^{sig} + N_{obs}^{QCD}$ . The sensitivity  $S$ , is a measure of how well we have predicted the background in the presence of signal. When  $S = 1$  the prediction is exactly the background and the excess is exactly the number of signal events. When  $S = 0$  the probabilities prediction has over estimated the background entirely resulting in no disagreement between observed and predicted

2 tag events.

$$\begin{aligned}
S = \frac{N_{obs}^{2tag} - N_{pred}^{2tag}}{N_{sig}} &= 1 - (2p\epsilon + \Delta\epsilon^2) \\
&\quad - (p^2 + \Delta^2\epsilon^2 + 2p\Delta\epsilon - 2p^2 - 2p\Delta\epsilon) \\
&\quad - (p^2\Delta - 2p^2\Delta - 2p\Delta^2\epsilon) \\
&\quad - (p^2\Delta^2)
\end{aligned}$$

where we have grouped terms by their order in  $O(\Delta) + O(p)$ . Consider the case when  $\epsilon \approx 1$  (this is an approximation for readability as  $\epsilon = 1$  would imply no 2 tag events) and for simplicity say  $\Delta = p = x$ .

$$S = 1 - 3x + 3x^3 - x^4$$

If we plug in the baseline fake rate for  $x$  then  $S(x = 5 \times 10^{-4}) = 0.999$ .

### 6.6.2 Tag Probability Cross Validation

To test the bias of the background estimation a method of cross validation is utilized. For a given sample,  $N_{div}$  non-overlapping sub-samples are partitioned. For each sub-sample, a corresponding set of jet probabilities are computed as described in the previous section. For each set of jet probabilities, an  $N_{tag}^{pred}$  prediction is made for the  $N_{div} - 1$  remaining samples (which have no overlapping events). We will refer to the sample used for the prediction as the measurement sample. The result is  $N_{div}(N_{div} - 1)$  pairs of probabilities and measurement samples. From each pair, in each bin of  $N_{tags}$ , we generate a distribution of pulls  $(N_{obs} - N_{pred})/\sqrt{N_{pred}}$  for each  $N_{tag}$  bin. All events must pass the event selection.

Due to limited statistics in the 2 tag bin for the baseline tag, the loose tag definition (Table 6.2) is used to generate pull distributions in the 2 tag bin.

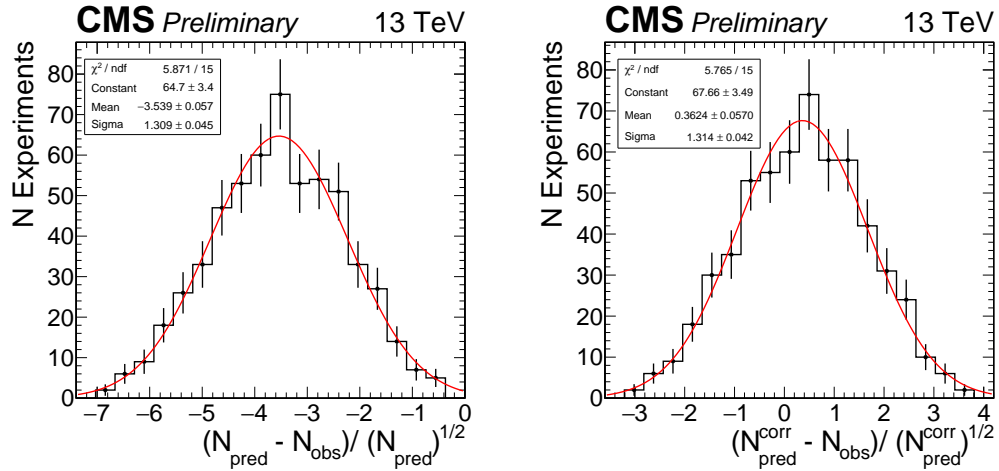


Figure 6.7: Cross validation of the predicted of the number of loose tags in data collected by the displaced jet triggers. Pulls for the 1 tag bin with the loose tag (left). Pulls for the 1 tag bin with the loose tag with the SR correction (Right).

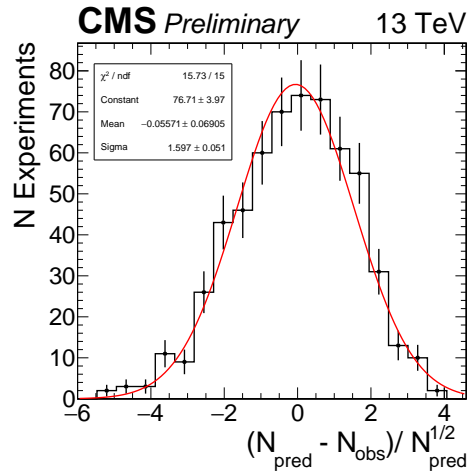


Figure 6.8: Cross validation of the predicted of the number of tags in data passing the displaced jet triggers. Pulls for the 1 tag bin with the baseline tag after the application of the signal removal correction  $2r_{12} = .2\%$

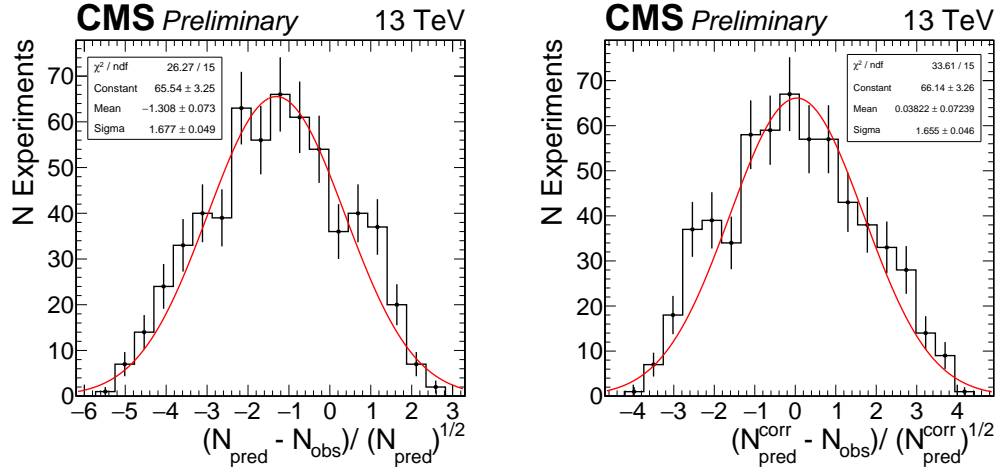


Figure 6.9: Cross validation of the predicted of the number of loose tags in QCD events passing the displaced jet triggers. Pulls for the 1 tag bin with the loose tag (left). The signal region removal corrected pulls (Right).

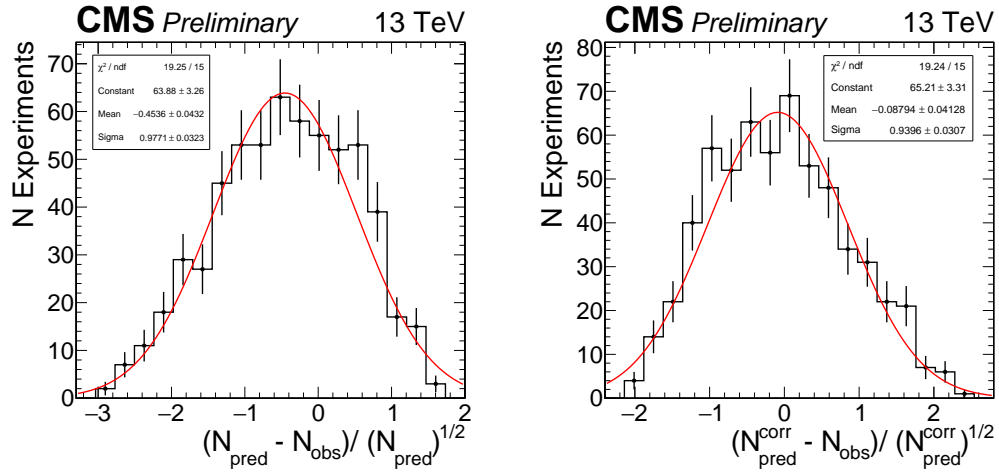


Figure 6.10: Cross validation of the predicted of the number of loose tag in QCD events passing the displaced jet triggers. Pulls for the 2 tag bin with the loose tag uncorrected (left). The same prediction corrected for the SR removal (right)

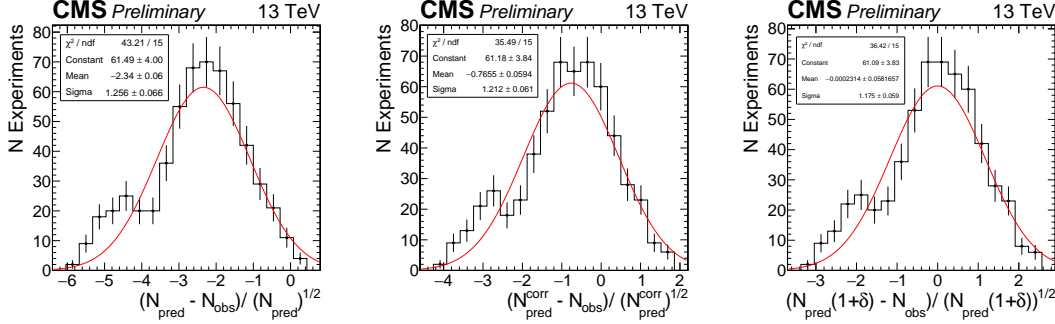


Figure 6.11: Cross validation of the predicted of the number of baseline tags in data collected by the displaced jet triggers. Pulls for the 2 tag bin with the loose tag (left). Pulls with the signal region removal correction applied (middle). The same signal region removal correction shifted by  $\delta = 7.5\%$  (Right).

We summarize the cross validation studies in the following figures:

- Fig 6.7: SR corrected and uncorrected 1 tag bin pulls for the Loose tag definition in Data collected by Displaced Jet Triggers.  $N_{div} = 25$
- Fig 6.8: SR corrected 1 tag bin pulls for the Baseline tag definition in Data collected by Displaced Jet Triggers.  $N_{div} = 25$
- Fig 6.9: 1 tag bin pulls for the Loose tag definition in QCD events passing the Displaced Jet Triggers.  $N_{div} = 25$
- Fig 6.10: 2 tag bin pulls for the Loose tag definition in QCD events passing by Displaced Jet Triggers.  $N_{div} = 25$
- Fig 6.11: SR corrected, uncorrected, and SR corrected+ $\delta$  2 tag bin pulls for the Loose tag definition in Data collected by Displaced Jet Triggers.  $N_{div} = 25$

In data and QCD, the SR correction provides a significant improvement on the pull distributions with respect to the ideal parameters  $\mu = 0$  and  $\sigma = 1.0$ . For the 1 tag prediction in data with the loose tag the central value changes from  $\mu = 3.5$  (uncorrected) to  $\mu = 0.36$  (corrected). For the signal region (2+ tags), the loose tag

in data is within 7.5% of ideal  $\mu$  and the QCD estimate is within error of  $\mu = 0$  but has  $\sigma = 1.6 > 1.0$ .

## 6.7 Systematic uncertainties

### 6.7.1 Background systematic uncertainties

A background systematic uncertainty is quoted for the data-driven background prediction method. This uncertainty is estimated by repeating the background-prediction procedure on data with a looser version of the displaced-jet tagging algorithm as outlined in section 6.6. The background estimation uncertainty of 7.5% is the required adjustment to the prediction to remove the bias observed in the Gaussian fit. For three or more tags, the systematic uncertainty for the method is kept fixed.

The statistical uncertainty on the measured misidentification rate as a function of  $N_{\text{tracks}}$  is propagated to the predicted  $N_{\text{tags}}$  distribution as a systematic uncertainty. This systematic uncertainty is calculated for each tag multiplicity bin individually. The uncertainty for the 2 tag bin is  $-12/+13\%$ .

In summary, for the background prediction in the two tag bin, a 7.5% uncertainty is assigned to the background prediction method and  $-12/+13\%$  uncertainty is assigned to the statistics of the misidentification rate.

### 6.7.2 Signal systematic uncertainties

A summary of the systematic uncertainties associated with the signal yields is given in Table 6.12. The uncertainty on the trigger emulation is measured by comparing the predicted efficiency for simulated multijet events and data collected by a loose  $H_T$  trigger. The observed difference at threshold (5%) is taken as an estimate of the uncertainty in the emulation of the online  $H_T$  requirement. Similarly, the uncertainty induced by the online versus offline jet acceptance is obtained from the shift in the

trigger efficiency when the offline jet  $p_t$  requirement is increased from  $p_t > 60$  GeV to  $p_t > 80$  GeV (5%).

The systematic uncertainty on the luminosity is 2.7% [10].

The uncertainty arising from the PDFs for pair-produced masses in the range of 50–1500GeV is found to be 1–6% Figure 6.12. An ensemble of alternative PDF is sampled from the output of the NNPDF fit. Events are reweighted according to the ratio between these alternative PDF sets and the nominal ones. The distribution of the signal prediction for these PDF ensemble is used to quantify the uncertainty.

The systematic uncertainty on the modeling of the jet tagging variables in signal MC samples is estimated from the displaced track modeling in multi-jet events in data and MC. The mismodeling of the measured value of  $\Theta_{2D}$  and  $IP_{sig}^{2D}$  for single tracks is propagated to the final tag distribution by varying the individual measured values in MC by the difference in the measured value relative to data (3–10%). The tagging variables are then re-calculated. The  $N_{tags}$  distribution is recalculated with the new values. The systematic uncertainty is assigned as the relative change in events, bin by bin in  $N_{tags}$ . For the two tag bin, this varies from 1 to 30% depending on the mass and lifetime Figure 6.16. The mismodeling of  $\alpha_{max}$  is found to have a negligible effect on the signal efficiency as the requirement is relatively loose.

The systematic uncertainty on the modeling of the online tracking efficiency is obtained by studying the online regional track reconstruction in data and MC. The online values of  $IP^{2D}$  and  $IP_{sig}^{2D}$  are varied by the magnitude of the mismodeling found in events collected in control triggers. The new values are used to determine if the event would still pass at least one of the trigger paths and its associated offline  $H_T$  requirement. The  $N_{tags}$  distribution is recalculated with the values varied up and down. The relative change in the number of events per bin is taken as the systematic uncertainty. For the two tag bin, this uncertainty varies from 1 to 35%.

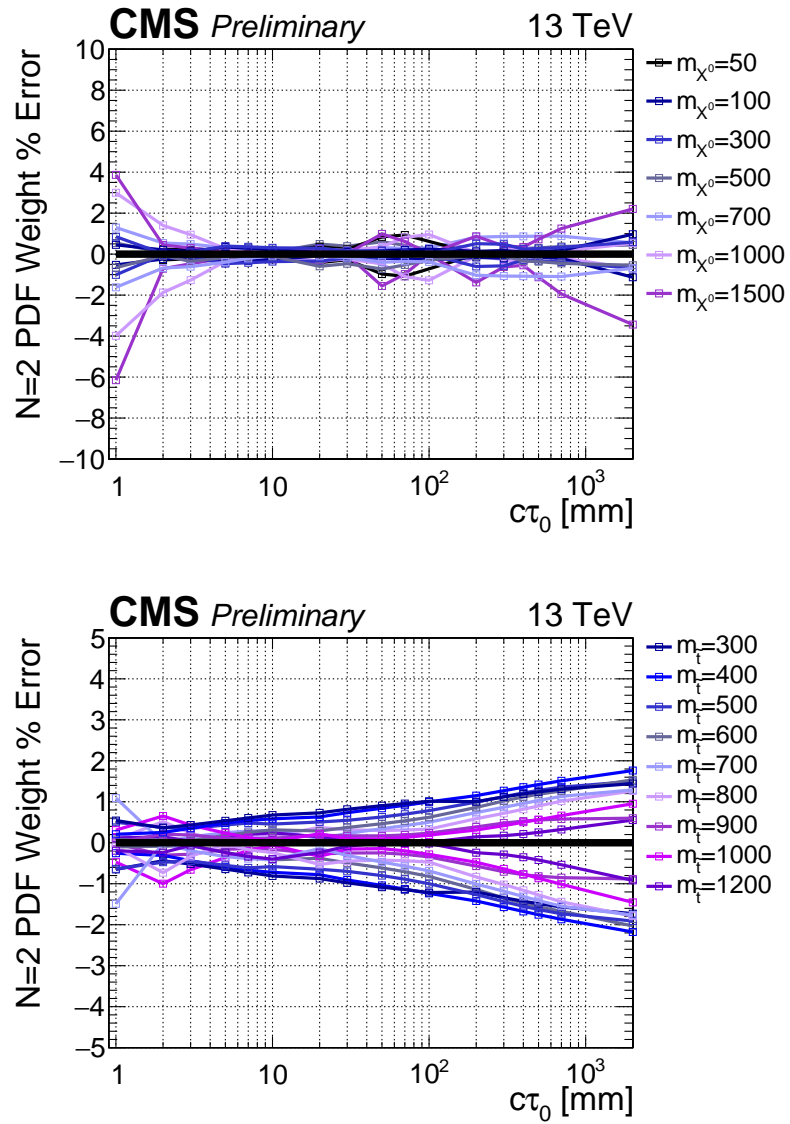


Figure 6.12: The PDF acceptance systematics in the Jet-Jet (left) and B-Lepton (right) signal model as a function of the mass  $m_X$  or  $c\tau_0$  for the 2 tag bin. The systematic is reported two sided for the two tag bin in the analysis. The error to fluctuate up is in the upper half plane and the error to fluctuate down on the lower half plane.

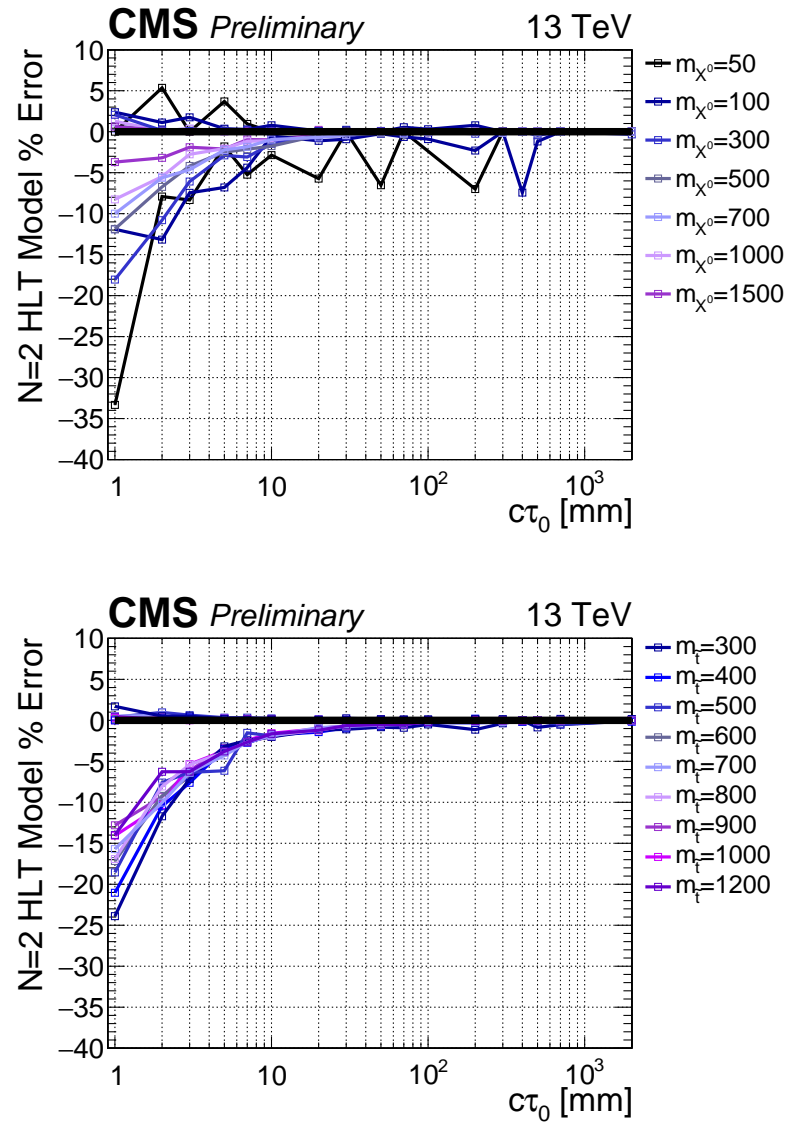


Figure 6.13: The onling tracking related systematics in the Jet-jet (top) and B-Lepton (bottom) model as a function of  $c\tau_0$ . (Top) The online track 2DIP and  $2DIP_{sig}$  modeling in the 2 tag bin

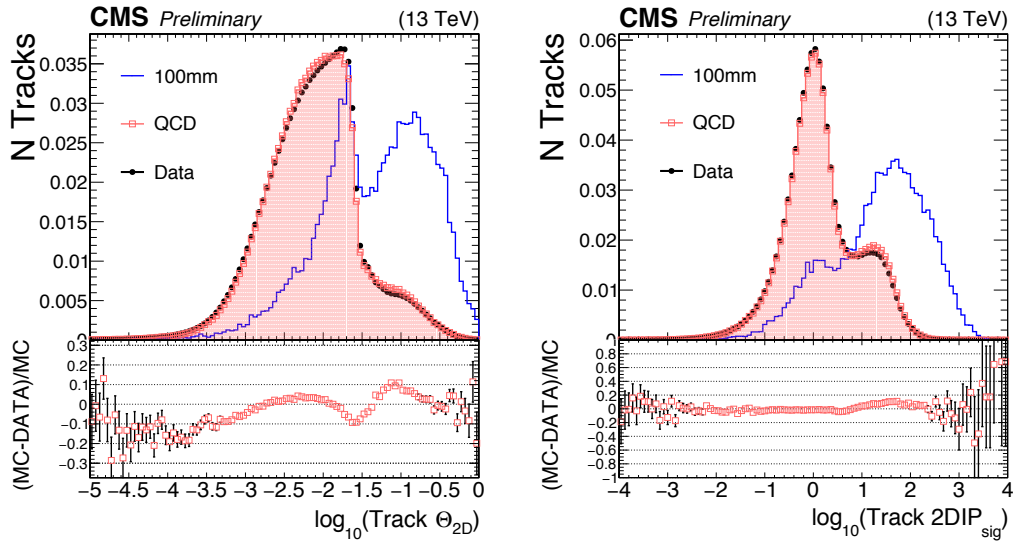


Figure 6.14: Comparison of the offline  $\theta$  and 2DIP<sub>sig</sub> for individual tracks associated to jets passing  $p_T > 60$  GeV and  $|\eta| < 2.0$  as collected by HLT-HT425.

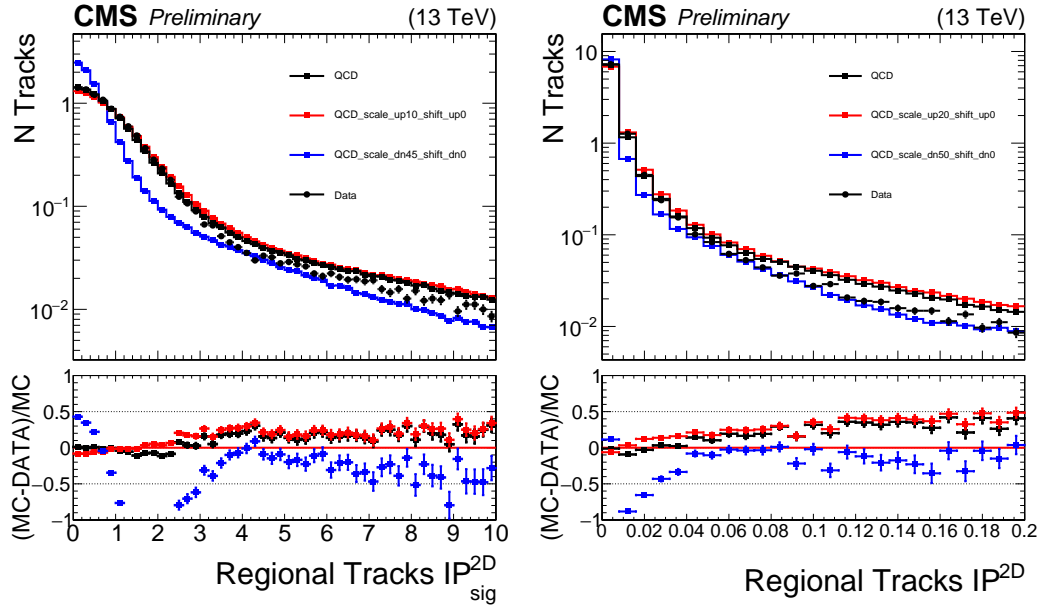


Figure 6.15: Comparison of the online 2DIP and 2DIP<sub>sig</sub> for individual tracks associated to jets passing  $p_T > 60$  GeV and  $|\eta| < 2.0$  as collected by HLT-HT425. For each variable  $x$  the value is scaled as  $x(1 \pm \Delta)$  with positive in red and the negative in blue. A re-scaling of  $+10/-45$  and  $+20/-50$  for 2DIP<sub>sig</sub> and 2DIP respectively provide an envelope for the DATA/MC differences

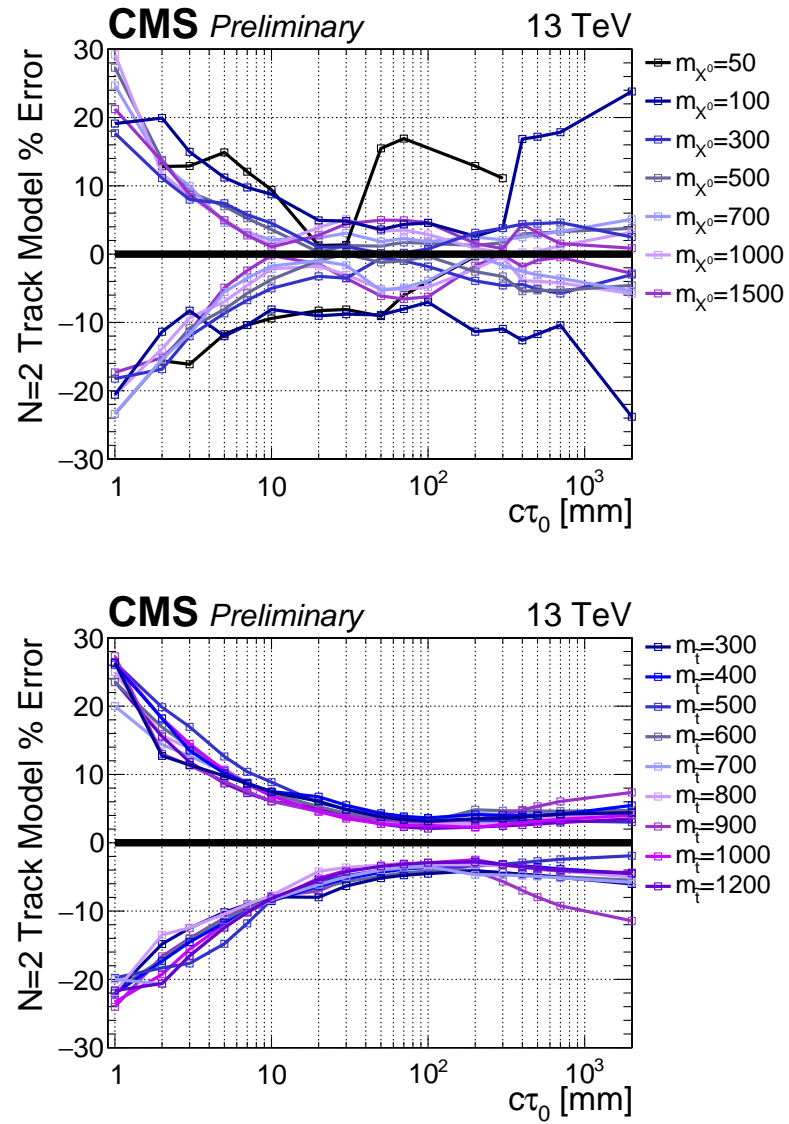


Figure 6.16: The two tracking related systematics in the Jet-Jet (top) and B-Lepton (bottom) model as a function of  $c\tau_0$ . The displaced jet tagging variable systematic in the 2 tag bin. The systematic is reported two sided for the two tag bin in the analysis. The error to fluctuate up is in the upper half plane and the error to fluctuate down on the lower half plane.

All signal systematic uncertainties are calculated individually for each model for all individual mass and lifetime points, and for each value of  $N_{\text{tags}}$  in the signal region.

## 6.8 Results and interpretation

The numerical values for the expected and observed yields are summarized in Table 6.13. The observed yields are found to be consistent with the predicted background, within the statistical and systematic uncertainties. No evidence for a signal at large values of  $N_{\text{tags}}$  is observed.

Exclusions for each model are obtained from the predicted and observed event yields in Table 6.13 and the signal efficiencies in Tables 6.7–6.8. All bounds are derived at 95% confidence-level (CL) according to the  $\text{CL}_s$  prescription [11, 12, 13] in the asymptotic approximation. For each limit derivation, we consider events with  $N_{\text{tags}} \geq 2$  using independent bins for  $N_{\text{tags}} = 2$  and  $N_{\text{tags}} \geq 3$ . Finer binning of the tag multiplicity for  $N_{\text{tags}} > 3$  is found to have a negligible affect on the expected limits. Cross section upper limits are presented as a function of the mass and lifetime of the parent particle. The analysis sensitivity is maximal for  $(10 < c\tau_0 < 1000)\text{mm}$ . Mass exclusion bounds at fixed lifetime are also derived, comparing the excluded cross section with the values predicted for the benchmark models described in section 6.5. In the case of SUSY models, the next-to-leading order (NLO) and next-to-leading-logs (NLL)  $t\bar{t}$  production cross section is used as reference, computed in the large-mass limit for all the other SUSY particles [14, 15, 16, 17, 18, 19].

Figures 6.17 and 6.18 show the excluded pair-production cross section for the Jet-Jet and Light-Light models, respectively. Cross sections as small as 1.2 fb are excluded for  $c\tau_0 = 50\text{mm}$  for both models. Exclusion limits are also derived for resonances decaying to  $b\ell$  final states, as shown in Fig. 6.19. The sensitivity is similar to what is observed for the Jet-Jet model, although less stringent as additional jets

give higher efficiency than additional leptons from both the tagging and triggering perspectives. Cross sections larger than 2.47 fb are excluded at 95% CL, for  $c\tau_0$  in the range 70–100 mm excluding a parent mass value of 1135 GeV.

Figures 6.20 and 6.21 show the exclusions on the B-Tau and B-Ele models, respectively. The two models have similar performance at high mass with slightly stronger limits for the B-Ele model at lower mass  $m_{\tilde{t}} = 300$  GeV and lifetimes  $c\tau_0 > 10$ mm. The highest mass excluded in the B-Ele (B-Tau) model occurs at  $m_{\tilde{t}} = 1150$  (1155)GeV and  $c\tau_0 = 70$  (70)mm at an observed cross section upper limit of 2.25 (2.17) fb at 95% CL.

In contrast, Fig. 6.22 shows the exclusion for the B-Mu model. Since the analysis uses jets reconstructed from calorimetric deposits while the two muons have small or no associated calorimeter deposit, the signal reconstruction efficiency and displaced-jet multiplicity are smaller in this case. This results in a weaker exclusion bound. The highest mass excluded in the B-Mu model occurs at  $m_{\tilde{t}} = 1090$  GeV and  $c\tau_0 = 70$ mm at an observed cross section upper limit of 3.36 fb at 95% CL.

Table 6.6: Signal efficiency for fixed  $m_X = m_{\tilde{t}} = 300$  GeV and varied  $c\tau_0$  with modified branching ratios relative to the Jet-Jet and B-Lepton models. Selection requirements are cumulative from the first to the last row.

<b>Light-Light</b>				
$m_X$ [GeV]	300	300	300	300
$c\tau_0$ [mm]	1	10	100	1000
$\geq 2$ tags	$2.20 \pm 0.19\%$	$40.49 \pm 0.80\%$	$54.92 \pm 0.93\%$	$14.55 \pm 0.47\%$
Trigger	$2.04 \pm 0.18\%$	$39.16 \pm 0.78\%$	$39.63 \pm 0.79\%$	$8.20 \pm 0.36\%$
Event sel.	$2.03 \pm 0.18\%$	$38.41 \pm 0.77\%$	$36.99 \pm 0.76\%$	$6.89 \pm 0.33\%$
$\geq 3$ tags	$0.187 \pm 0.054\%$	$14.77 \pm 0.48\%$	$16.70 \pm 0.51\%$	$1.48 \pm 0.15\%$
$\geq 4$ tags	–	$5.11 \pm 0.28\%$	$4.73 \pm 0.27\%$	$0.216 \pm 0.058\%$
<b>B-Ele</b>				
$m_{\tilde{t}}$ [GeV]	300	300	300	300
$c\tau_0$ [mm]	1	10	100	1000
$\geq 2$ tags	$0.807 \pm 0.093\%$	$20.51 \pm 0.47\%$	$39.01 \pm 0.65\%$	$11.46 \pm 0.35\%$
Trigger	$0.398 \pm 0.065\%$	$14.68 \pm 0.40\%$	$22.95 \pm 0.50\%$	$5.15 \pm 0.23\%$
Event sel.	$0.398 \pm 0.065\%$	$13.92 \pm 0.39\%$	$20.34 \pm 0.47\%$	$3.58 \pm 0.19\%$
$\geq 3$ tags	$0.043 \pm 0.022\%$	$4.22 \pm 0.21\%$	$7.21 \pm 0.28\%$	$0.822 \pm 0.093\%$
$\geq 4$ tags	–	$0.727 \pm 0.088\%$	$1.19 \pm 0.11\%$	$0.053 \pm 0.024\%$
<b>B-Tau</b>				
$m_{\tilde{t}}$ [GeV]	300	300	300	300
$c\tau_0$ [mm]	1	10	100	1000
$\geq 2$ tags	$0.483 \pm 0.073\%$	$18.40 \pm 0.45\%$	$34.98 \pm 0.61\%$	$9.31 \pm 0.32\%$
Trigger	$0.439 \pm 0.069\%$	$14.63 \pm 0.40\%$	$20.20 \pm 0.46\%$	$3.81 \pm 0.20\%$
Event sel.	$0.406 \pm 0.067\%$	$12.45 \pm 0.37\%$	$15.50 \pm 0.41\%$	$2.37 \pm 0.16\%$
$\geq 3$ tags	$0.022 \pm 0.016\%$	$3.23 \pm 0.19\%$	$4.62 \pm 0.22\%$	$0.441 \pm 0.069\%$
$\geq 4$ tags	–	$0.525 \pm 0.076\%$	$0.660 \pm 0.084\%$	$0.022 \pm 0.015\%$
<b>B-Mu</b>				
$m_{\tilde{t}}$ [GeV]	300	300	300	300
$c\tau_0$ [mm]	1	10	100	1000
$\geq 2$ tags	$0.130 \pm 0.037\%$	$8.02 \pm 0.29\%$	$20.09 \pm 0.46\%$	$4.03 \pm 0.21\%$
Trigger	$0.054 \pm 0.024\%$	$3.97 \pm 0.21\%$	$6.63 \pm 0.26\%$	$0.881 \pm 0.098\%$
Event sel.	$0.043 \pm 0.022\%$	$2.92 \pm 0.18\%$	$4.21 \pm 0.21\%$	$0.489 \pm 0.073\%$
$\geq 3$ tags	–	$0.227 \pm 0.049\%$	$0.307 \pm 0.057\%$	$0.033 \pm 0.019\%$
$\geq 4$ tags	–	$0.011 \pm 0.011\%$	–	–

Table 6.7: Signal efficiencies for the Jet-Jet and B-Lepton models with  $c\tau_0 = 30\text{mm}$  and varied mass. Selection requirements are cumulative from the first to the last row.

<b>Jet-Jet</b>				
$m_X$ [GeV]	50	100	300	1000
$c\tau_0$ [mm]	30	30	30	30
$\geq 2$ tags	$2.710 \pm 0.095\%$	$14.80 \pm 0.22\%$	$54.24 \pm 0.74\%$	$79.93 \pm 0.89\%$
Trigger	$0.503 \pm 0.041\%$	$5.39 \pm 0.13\%$	$46.41 \pm 0.68\%$	$74.05 \pm 0.86\%$
Event sel.	$0.297 \pm 0.031\%$	$3.70 \pm 0.11\%$	$44.75 \pm 0.67\%$	$73.99 \pm 0.86\%$
$\geq 3$ tags	$0.050 \pm 0.013\%$	$1.087 \pm 0.060\%$	$20.87 \pm 0.46\%$	$49.42 \pm 0.70\%$
$\geq 4$ tags	–	$0.217 \pm 0.027\%$	$6.81 \pm 0.26\%$	$25.45 \pm 0.50\%$

<b>B-Lepton</b>				
$m_{\tilde{t}}$ [GeV]	300	600	800	1000
$c\tau_0$ [mm]	30	30	30	30
$\geq 2$ tags	$31.52 \pm 0.19\%$	$47.32 \pm 0.23\%$	$52.53 \pm 0.24\%$	$55.88 \pm 0.35\%$
Trigger	$17.08 \pm 0.14\%$	$35.03 \pm 0.20\%$	$40.40 \pm 0.21\%$	$43.14 \pm 0.30\%$
Event sel.	$14.70 \pm 0.13\%$	$32.34 \pm 0.19\%$	$36.94 \pm 0.20\%$	$39.26 \pm 0.29\%$
$\geq 3$ tags	$4.106 \pm 0.068\%$	$10.76 \pm 0.11\%$	$13.29 \pm 0.12\%$	$15.00 \pm 0.18\%$
$\geq 4$ tags	$0.552 \pm 0.025\%$	$1.828 \pm 0.045\%$	$2.687 \pm 0.055\%$	$3.092 \pm 0.082\%$

Table 6.8: Signal efficiency for fixed  $c\tau_0 = 30$ mm and varied mass with modified branching ratios relative to the Jet-Jet and B-Lepton models. Selection requirements are cumulative from the first to the last row.

<b>Light-Light</b>					
$m_X$ [GeV]	50	100	300	1000	
$c\tau_0$ [mm]	30	30	30	30	
$\geq 2$ tags	$2.84 \pm 0.12\%$	$15.56 \pm 0.29\%$	$54.87 \pm 0.92\%$	$80.52 \pm 1.11\%$	
Trigger	$0.530 \pm 0.052\%$	$5.70 \pm 0.17\%$	$47.14 \pm 0.85\%$	$74.85 \pm 1.07\%$	
Event sel.	$0.327 \pm 0.041\%$	$3.90 \pm 0.14\%$	$45.68 \pm 0.84\%$	$74.80 \pm 1.07\%$	
$\geq 3$ tags	$0.052 \pm 0.016\%$	$1.113 \pm 0.076\%$	$21.77 \pm 0.58\%$	$50.04 \pm 0.88\%$	
$\geq 4$ tags	–	$0.230 \pm 0.035\%$	$7.38 \pm 0.34\%$	$25.80 \pm 0.63\%$	
<b>B-Ele</b>					
$m_{\tilde{t}}$ [GeV]	300	600	800	1000	
$c\tau_0$ [mm]	30	30	30	30	
$\geq 2$ tags	$39.01 \pm 0.65\%$	$53.70 \pm 0.75\%$	$59.62 \pm 0.78\%$	$62.42 \pm 1.11\%$	
Trigger	$22.95 \pm 0.50\%$	$38.07 \pm 0.63\%$	$43.06 \pm 0.66\%$	$45.21 \pm 0.95\%$	
Event sel.	$21.59 \pm 0.48\%$	$37.02 \pm 0.62\%$	$39.47 \pm 0.64\%$	$42.20 \pm 0.92\%$	
$\geq 3$ tags	$7.86 \pm 0.29\%$	$14.28 \pm 0.38\%$	$17.37 \pm 0.42\%$	$20.39 \pm 0.64\%$	
$\geq 4$ tags	$1.37 \pm 0.12\%$	$3.32 \pm 0.19\%$	$4.34 \pm 0.21\%$	$4.69 \pm 0.31\%$	
<b>B-Tau</b>					
$m_{\tilde{t}}$ [GeV]	300	600	800	1000	
$c\tau_0$ [mm]	30	30	30	30	
$\geq 2$ tags	$34.98 \pm 0.61\%$	$51.42 \pm 0.73\%$	$57.20 \pm 0.76\%$	$59.43 \pm 1.07\%$	
Trigger	$20.20 \pm 0.46\%$	$39.78 \pm 0.64\%$	$45.46 \pm 0.68\%$	$47.62 \pm 0.96\%$	
Event sel.	$17.17 \pm 0.43\%$	$37.47 \pm 0.62\%$	$43.64 \pm 0.67\%$	$44.26 \pm 0.92\%$	
$\geq 3$ tags	$5.21 \pm 0.24\%$	$13.29 \pm 0.37\%$	$16.15 \pm 0.40\%$	$19.13 \pm 0.61\%$	
$\geq 4$ tags	$0.86 \pm 0.10\%$	$3.09 \pm 0.18\%$	$3.68 \pm 0.19\%$	$4.48 \pm 0.29\%$	
<b>B-Mu</b>					
$m_{\tilde{t}}$ [GeV]	300	600	800	1000	
$c\tau_0$ [mm]	30	30	30	30	
$\geq 2$ tags	$20.09 \pm 0.46\%$	$35.46 \pm 0.60\%$	$41.18 \pm 0.64\%$	$43.13 \pm 0.93\%$	
Trigger	$6.63 \pm 0.26\%$	$24.73 \pm 0.50\%$	$31.85 \pm 0.56\%$	$34.10 \pm 0.82\%$	
Event sel.	$5.25 \pm 0.24\%$	$21.40 \pm 0.47\%$	$27.42 \pm 0.52\%$	$31.18 \pm 0.79\%$	
$\geq 3$ tags	$0.344 \pm 0.060\%$	$3.03 \pm 0.18\%$	$5.28 \pm 0.23\%$	$6.08 \pm 0.35\%$	
$\geq 4$ tags	–	$0.122 \pm 0.035\%$	$0.677 \pm 0.082\%$	$0.68 \pm 0.12\%$	

Table 6.9: The signal injection test using a fixed signal point  $m_X = 700$  GeV and  $c\tau_0 = 10\text{mm}$  with varied amount of injection. A summary of the 1,2,3, and 4 tag predictions as a function of the number of events injected (top). The two background systematic errors are listed separately as  $\sigma_{method}, \sigma_{fake-rate}$ . A summary of the observed number of tags (bottom).

<b>Injection <math>\sigma \times \mathcal{L}</math></b>	<b>1 Tag Pred</b>	<b>2 Tag Pred</b>	<b>3 Tag Pred</b>	<b>4 Tag Pred</b>
0	$185^{+14,+17}_{-14,-13}$	$0.16^{+0.01,+0.03}_{-0.01,-0.02}$	—	—
10	$187^{+14,+17}_{-14,-13}$	$0.16^{+0.01,+0.03}_{-0.01,-0.02}$	—	—
100	$207^{+16,+18}_{-16,-14}$	$0.20^{+0.02,+0.04}_{-0.02,-0.03}$	—	—
1000	$408^{+31,+23}_{-31,-19}$	$0.81^{+0.06,+0.09}_{-0.06,-0.08}$	—	—
10000	$2366^{+177,+53}_{-177,-49}$	$26.95^{+2.02,+1.19}_{-2.02,-1.10}$	$0.18^{+0.01,+0.01}_{-0.01,-0.01}$	—
<b>Injection <math>\sigma \times \mathcal{L}</math></b>	<b>1 Tag Obs</b>	<b>2 Tag Obs</b>	<b>3 Tag Obs</b>	<b>4 Tag Obs</b>
0	185.00	0.00	0.00	0.00
10	186.94	2.40	1.99	1.20
100	205.14	23.05	20.45	11.89
1000	386.10	237.20	188.40	116.80
10000	2260.00	2341.00	1976.00	1165.00

Table 6.10: Signal injection test with fixed number of injected events and varied  $c\tau_0$  and  $m_X$ . A summary of the 1,2,3, and 4 tag predictions as a function of the number of events injected (top). The two background systematic errors are listed separately as  $\sigma_{method}, \sigma_{fake-rate}$ . A summary of the observed number of tags (bottom).

<b><math>\sigma \times \mathcal{L}</math></b>	<b>Mass [GeV]</b>	<b><math>c\tau_0</math> [mm]</b>	<b>1 Tag Pred</b>	<b>2 Tag Pred</b>	<b>3 Tag Pred</b>	<b>4 Tag Pred</b>
100	700	10	$207^{+16,+18}_{-16,-14}$	$0.20^{+0.02,+0.04}_{-0.02,-0.03}$	—	—
100	700	1000	$202^{+15,+18}_{-15,-14}$	$0.20^{+0.02,+0.03}_{-0.02,-0.03}$	—	—
1000	100	10	$222^{+17,+18}_{-17,-14}$	$0.23^{+0.02,+0.04}_{-0.02,-0.03}$	—	—
1000	100	1000	$195^{+15,+17}_{-15,-13}$	$0.18^{+0.01,+0.03}_{-0.01,-0.02}$	—	—
<b><math>\sigma \times \mathcal{L}</math></b>	<b>Mass [GeV]</b>	<b><math>c\tau_0</math> [mm]</b>	<b>1 Tag Obs</b>	<b>2 Tag Obs</b>	<b>3 Tag Obs</b>	<b>4 Tag Obs</b>
100	700	10	205.14	23.05	20.45	11.89
100	700	1000	211.56	17.98	9.04	3.62
1000	100	10	403.57	74.33	20.97	5.13
1000	100	1000	320.64	22.92	3.60	0.39

Table 6.11: A summary of the size of the signal injected in the signal injection test (top). A summary of signal region yields in the 2,3, and 4 nominal displaced jet tag bins (middle) and the observed number of tags (bottom), as a function of the size of the signal contamination, for a signal injection test using a fixed signal point  $m_X = 700$  GeV and  $c\tau_0 = 10$  mm with varied signal yields. The no signal case is included as a reference to the predicted values without contamination. The test is normalized such that the sum of signal and background events stays fixed at the observed number of events passing the analysis event selection. The contamination fraction corresponds to the hypothetical fraction of signal events contained within the events passing the event selection.

Contam. Fraction	Signal $\sigma$ [fb]		
0	0		
0.01%	30		
0.10%	290		
1.04%	3000		
9.47%	28000		
Contamination %	2 tag pred	3 tag pred	4 tag pred
0	$1.34^{+0.25}_{-0.17}$	-	-
0.01%	$1.34^{+0.25}_{-0.17}$	-	-
0.10%	$1.67 \pm 0.33$	-	-
1.04%	$6.71^{+0.91}_{-0.82}$	-	-
9.47%	$205.38 \pm 15.21$	$1.37 \pm 0.08$	-
Contamination %	2 tag obs	3 tag obs	4 tag obs
0.00%	0	0	0
0.01%	19	16	10
0.10%	179	159	93
1.04%	1914	1520	943
9.47%	17632	14883	8775

Table 6.12: Summary of the systematic uncertainties. When the uncertainty depends on the specific features of the models (mass, lifetime and decay mode of the long-lived particle) a range is quoted, which refers to the computed uncertainty for  $N_{\text{tags}} = 2$  events.

<b>Signal systematic uncertainty</b>	<b>Effect on yield</b>
$H_T$ trigger inefficiency	5.0%
Jet $p_t$ trigger inefficiency	5.0%
Trigger online tracking modeling	1.0–35.0%
Luminosity	2.7%
Acceptance due to PDF	1.0–6.0%
Displaced-jet tag variable modeling	1.0–30.0%

Table 6.13: The predicted and observed number of events as a function of  $N_{\text{tags}}$ . The prediction is based on the mistagging probability derived from events with fewer than two tags. The full event selection is applied. The quoted uncertainty corresponds to the total background systematic uncertainty.

$N_{\text{tags}}$	<b>Expected</b>	<b>Observed</b>
2	$1.09^{+0.16}_{-0.15}$	1
$\geq 3$	$(4.9 \pm 1.0) \times 10^{-4}$	0

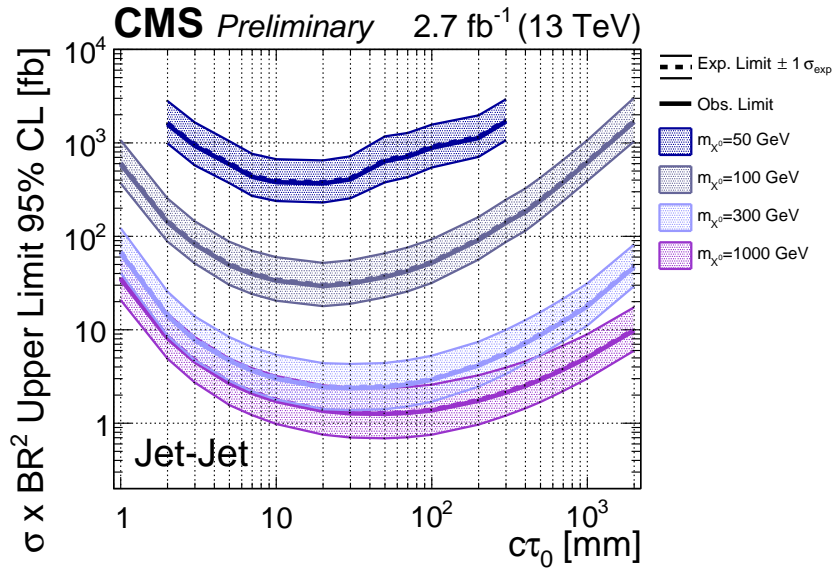
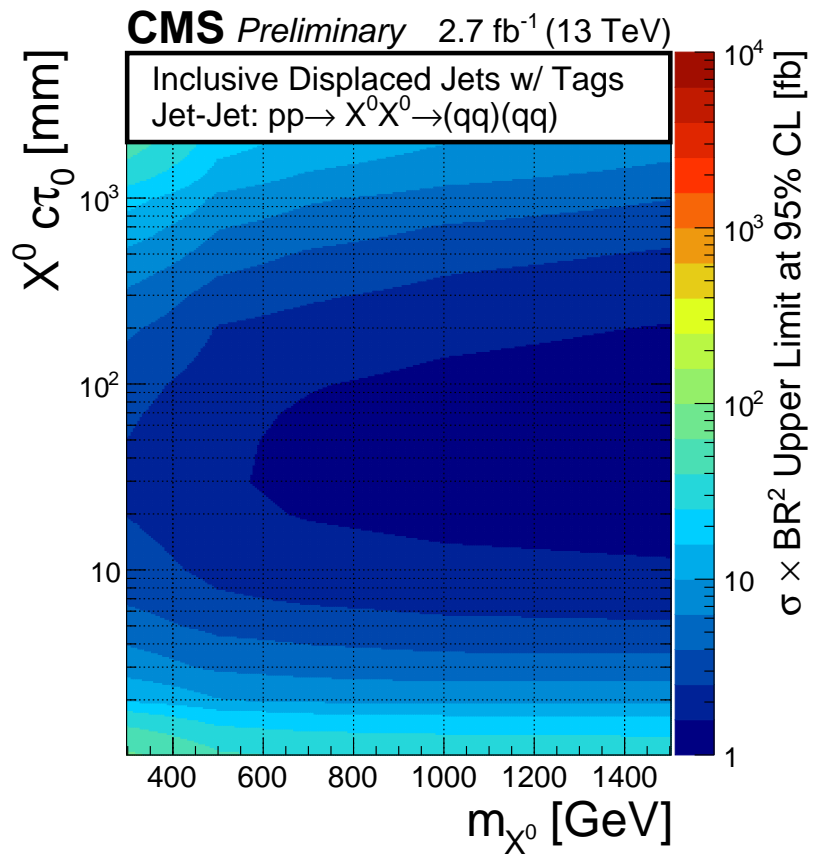


Figure 6.17: The excluded cross section at 95% CL for the Jet-Jet model as a function of the mass and lifetime of the parent particle  $X^0$  (top) and as a function of the lifetime for four values of the mass (bottom).

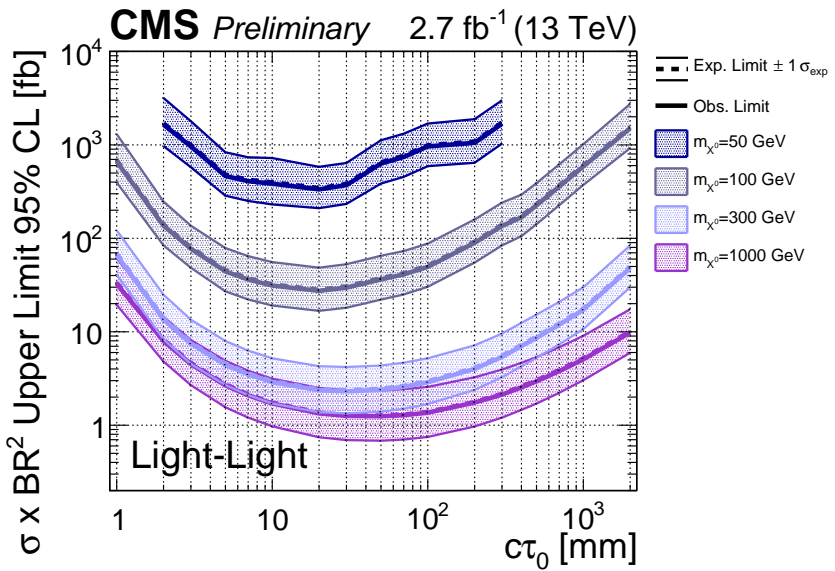
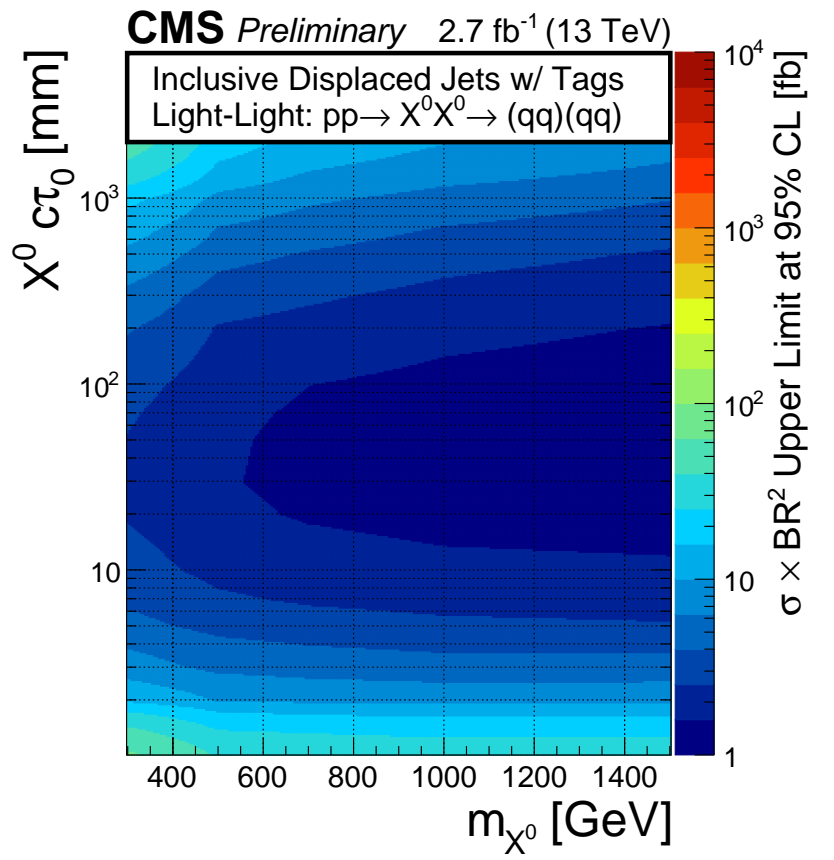


Figure 6.18: The excluded cross section at 95% CL for the Light-Light model as a function of the mass and lifetime of the parent particle  $X^0$  (top) and as a function of the lifetime for four values of the mass (bottom).

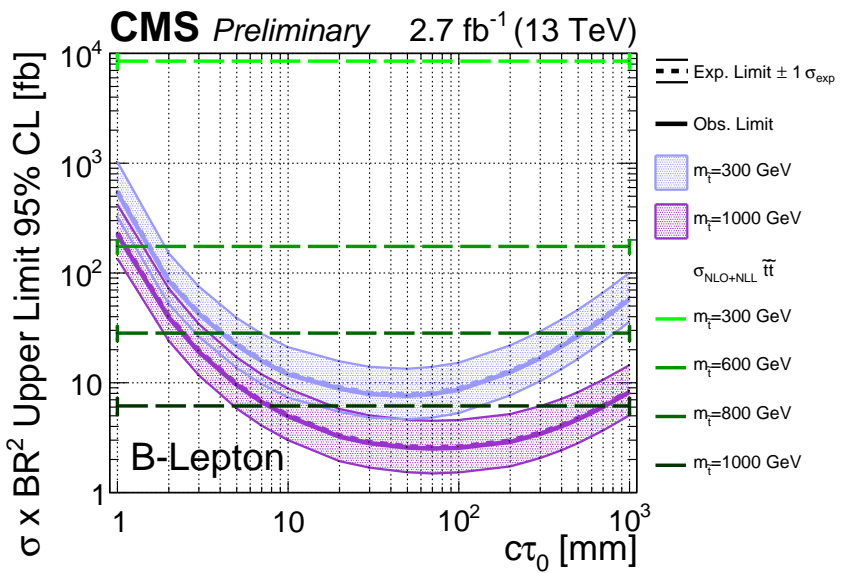
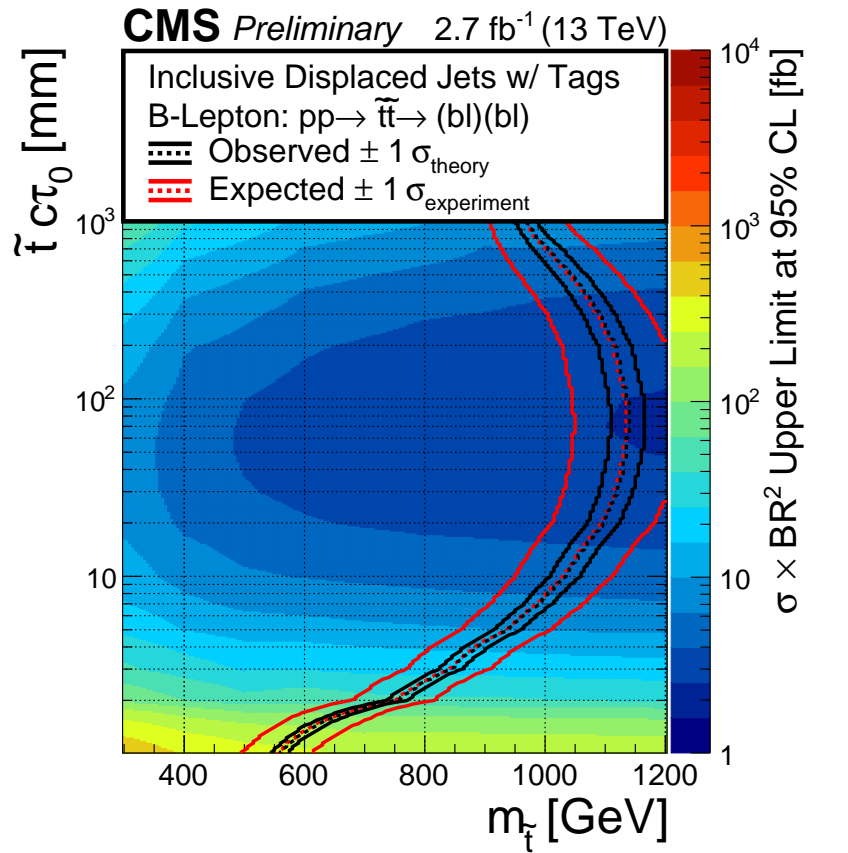


Figure 6.19: The excluded cross section at 95% CL for the B-Lepton model as a function of the mass and lifetime of the parent particle  $\tilde{t}$  (top) and as a function of the lifetime for two values of the mass (bottom). The bottom plot also shows the expected upper limits with one standard deviation uncertainties.

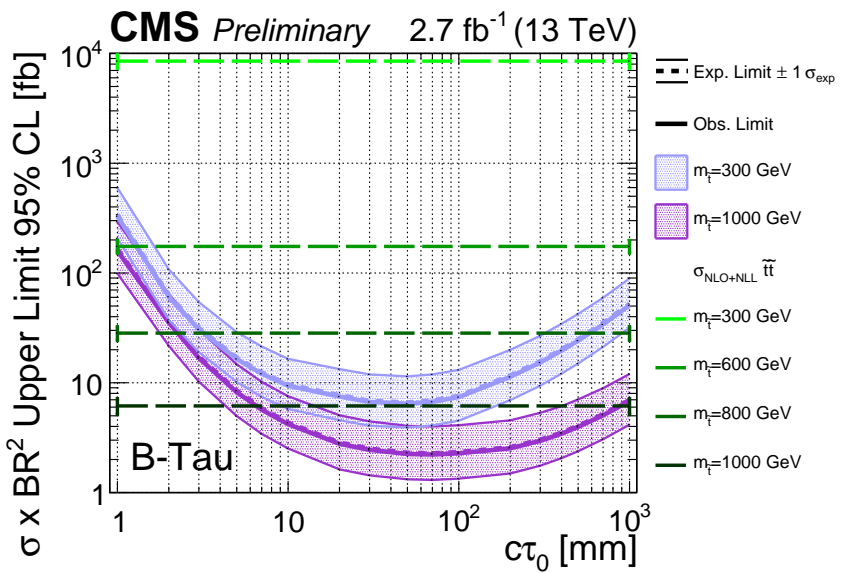
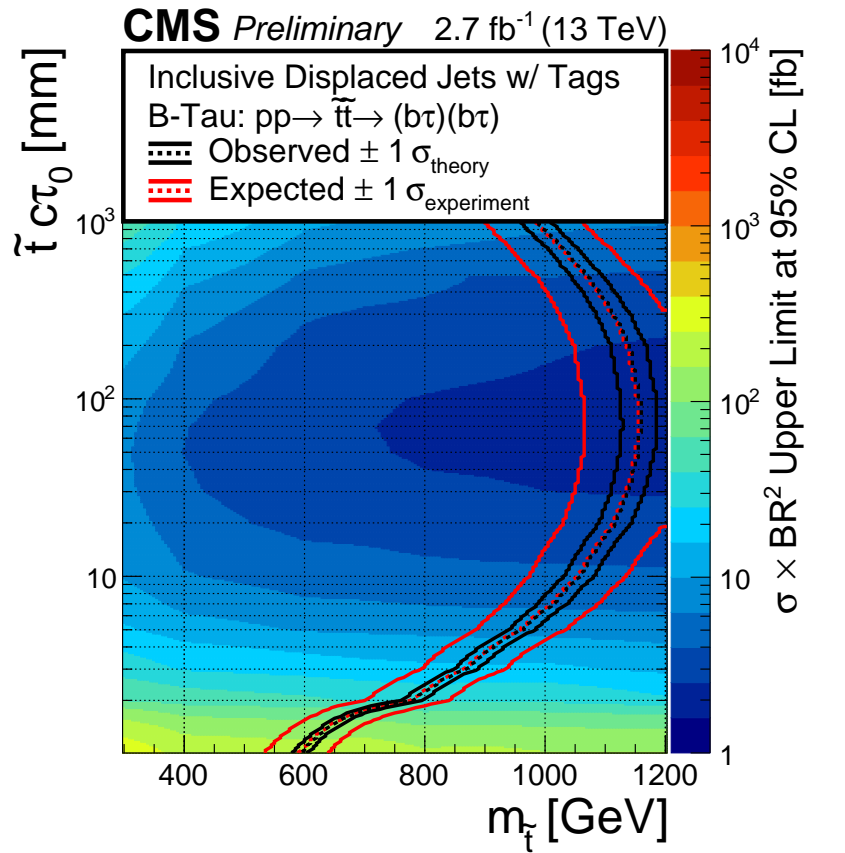


Figure 6.20: The excluded cross section at 95% CL for the B-Tau model as a function of the mass and lifetime of the parent particle  $\tilde{t}$  (top) and as a function of the lifetime for two values of the mass (bottom). The bottom plot also shows the expected upper limits with one standard deviation uncertainties.

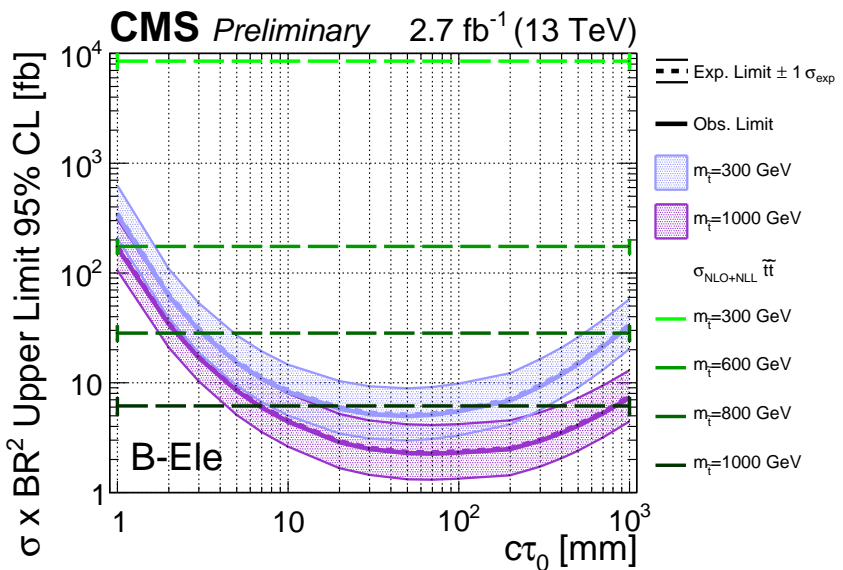
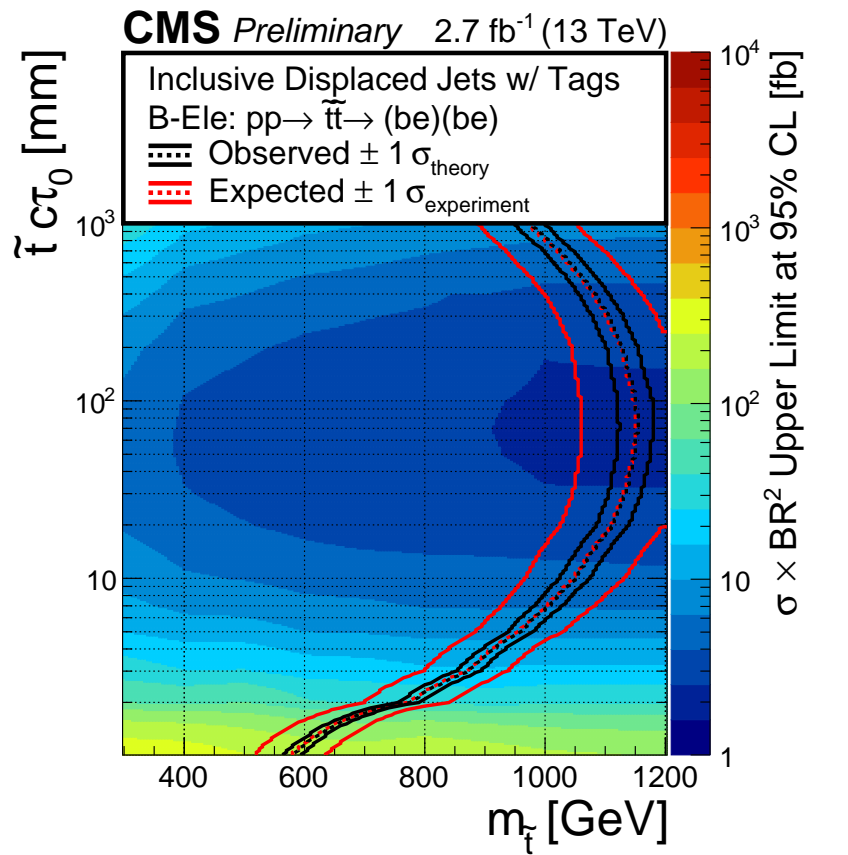


Figure 6.21: The excluded cross section at 95% CL for the B-Ele model as a function of the mass and lifetime of the parent particle  $\tilde{t}$  (top) and as a function of the lifetime for four values of the mass (bottom). The bottom plot also shows the expected upper limits with one standard deviation uncertainties.

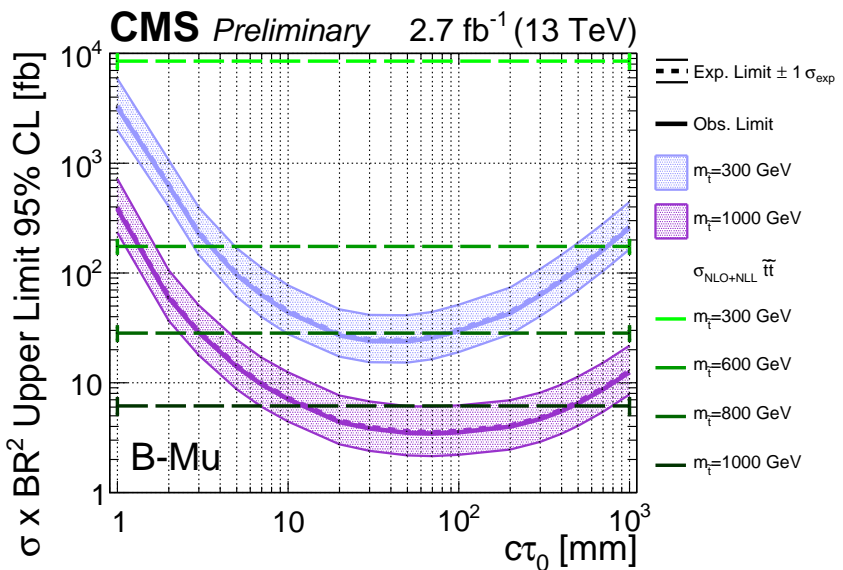
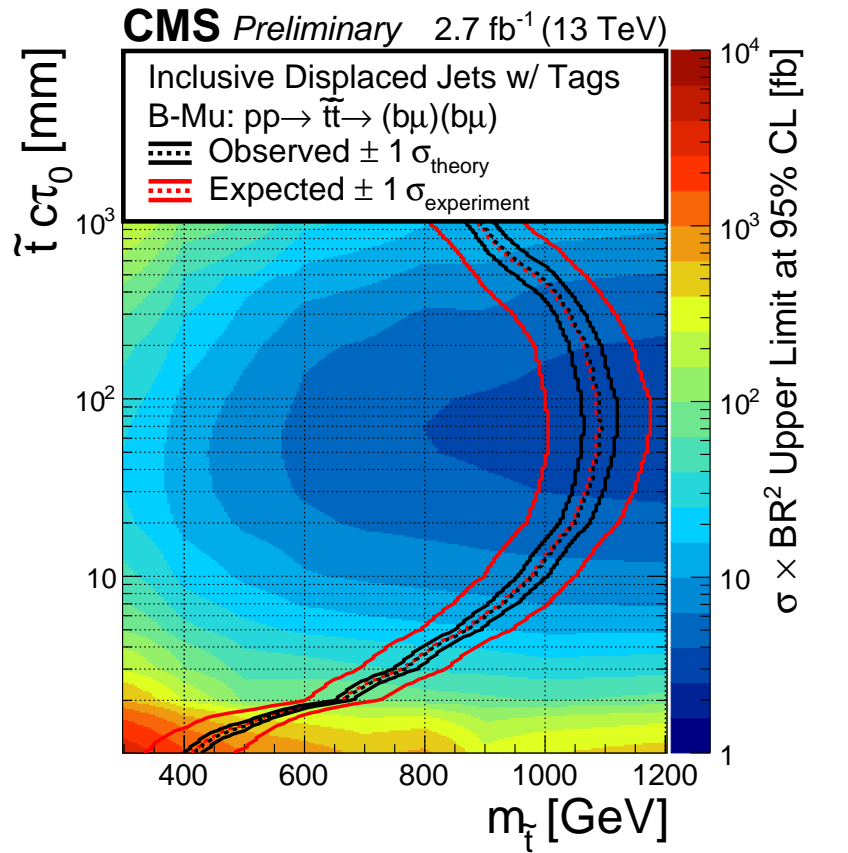


Figure 6.22: The excluded cross section at 95% CL for the B-Mu model as a function of the mass and lifetime of the parent particle  $\tilde{t}$  (top) and as a function of the lifetime for four values of the mass (bottom). The bottom plot also shows the expected upper limits with one standard deviation uncertainties.

# Bibliography

- [1] Georges Aad et al. Search for long-lived, weakly interacting particles that decay to displaced hadronic jets in proton-proton collisions at  $\sqrt{s} = 8$  TeV with the atlas detector. *Phys. Rev. D*, 92:012010, 2015.
- [2] Georges Aad et al. Search for massive, long-lived particles using multitrack displaced vertices or displaced lepton pairs in pp collisions at  $\sqrt{s} = 8$  TeV with the ATLAS detector. *Phys. Rev. D*, 92:072004, 2015.
- [3] Vardan Khachatryan et al. Search for Long-Lived Neutral Particles Decaying to Quark-Antiquark Pairs in Proton-Proton Collisions at  $\sqrt{s} = 8$  TeV. *Phys. Rev. D*, 91:012007, 2015.
- [4] Matteo Cacciari, Gavin P. Salam, and Gregory Soyez. Fastjet user manual. *Eur. Phys. J. C*, 72, 2012.
- [5] Matteo Cacciari, Gavin P. Salam, and Gregory Soyez. The anti- $k_t$  jet clustering algorithm. *JHEP*, 04:063, 2008.
- [6] T. Sjöstrand, Stephen Mrenna, and Peter Z. Skands. A brief introduction to PYTHIA 8.1. *Comput. Phys. Commun.*, 178:852, 2008.
- [7] R. et al Ball. Parton distributions with LHC data. *Nucl. Phys. B*, 867:244, 2013.
- [8] M. Strassler and Zurek K. Discovering the higgs through highly displaced vertices. *Phys. Lett. B*, 263, 2008.
- [9] P. Graham, D. Kaplan, S. Rajendran, and P. Sarawat. Displaced supersymmetry. *Journal of High Energy Physics*, 149, 2012.
- [10] CMS Luminosity Measurement for the 2015 Data Taking Period. Technical Report CMS-PAS-LUM-15-001, CERN, Geneva, 2016.
- [11] A. L. Read. Presentation of search results: the  $CL_s$  technique. *J. Phys. G*, 28:2693, 2002.
- [12] Thomas Junk. Confidence level computation for combining searches with small statistics. *Nucl. Instrum. Meth. A*, 434:435, 1999.
- [13] CMS and ATLAS Collaborations. Procedure for the lhc higgs boson search combination in summer 2011. CMS-NOTE-2011-005, 2011.

- [14] W. Beenakker, R. Höpker, M. Spira, and P. M. Zerwas. Squark and gluino production at hadron colliders. *Nucl. Phys. B*, 492:51, 1997.
- [15] A. Kulesza and L. Motyka. Threshold resummation for squark-antisquark and gluino-pair production at the LHC. *Phys. Rev. Lett.*, 102:111802, 2009.
- [16] A. Kulesza and L. Motyka. Soft gluon resummation for the production of gluino-gluino and squark-antisquark pairs at the LHC. *Phys. Rev. D*, 80:095004, 2009.
- [17] W. Beenakker, S. Brensing, M. Krämer, A. Kulesza, E. Laenen, and I. Niessen. Soft-gluon resummation for squark and gluino hadroproduction. *JHEP*, 12:041, 2009.
- [18] W. Beenakker, S. Brensing, M. Krämer, A. Kulesza, E. Laenen, L. Motyka, and I. Niessen. Squark and gluino hadroproduction. *Int. J. Mod. Phys. A*, 26:2637, 2011.
- [19] M. Krämer, A. Kulesza, R. van der Leeuw, M. Mangano, S. Padhi, T. Plehn, and X. Portell. Supersymmetry production cross sections in pp collisions at  $\sqrt{s} = 7$  TeV. 2012.